Delft University of Technology

On self magnetic flux leakage in support of fatigue crack monitoring in ship and offshore structures
A numerical, experimental, and full-scale application study

van der Horst, Menno

Important note
To cite this publication, please use the final published version (if applicable).
Please check the document version above.

On Self Magnetic Flux Leakage in Support of Fatigue Crack Monitoring in Ship and Offshore Structures

Dissertation

for the purpose of obtaining the degree of doctor
at Delft University of Technology
by the authority of the Rector Magnificus prof.dr.ir. T.H.J.J. van der Hagen
chair of the Board for Doctorates
to be defended publicly on
Tuesday 23 October 2018 at 15:00 o'clock

by

Menno Patrick VAN DER HORST

Master of Science in Structural Engineering,
Delft University of Technology, The Netherlands
born in Santa Clara (CA), United States of America

This dissertation has been approved by the promotor.

Composition of the doctoral committee:
Rector Magnificus,   chairperson
Prof.dr.ir. M.L. Kaminski   Delft University of Technology, promotor

Independent members:
Prof.dr. I.M. Richardson   Delft University of Technology
Prof.dr.ir. P.H.A.J.M. van Gelder   Delft University of Technology
Prof.dr.ir. T. Tinga   University of Twente
Prof.dr.ir. W. de Waele   Ghent University, Belgium

Other members:
Dr.ing. E. Puik   HU University of Applied Sciences Utrecht
Dr. E.S.A.M. Lepelaars   TNO

Keywords: fatigue, crack monitoring, ship and offshore structures, self magnetic flux leakage, metal magnetic memory method

Printed by: Print Service Ede
Cover by: Sinds 1961 Grafisch Ontwerp

An electronic version of this dissertation is available at *http://repository.tudelft.nl/*.

To my wife, Mallery

Who left her home across the sea

Just to be with me

To give me her love and support

So that I can finish this work

Contents

Summary

Ship and offshore structures are prone to fatigue damage as they are cyclically loaded by waves. Therefore, regular inspection is needed in order to confirm adequate structural integrity throughout the entire service life of the structure. Detected fatigue cracks that are too long for safe operation need to be repaired. Detected cracks of acceptable length need to be at least inspected more frequently. These inspections are costly, time consuming, and hazardous, so additional inspections on top of the periodical class approval surveys are to be avoided if possible.

The research presented in this thesis proposes using a monitoring system for detected cracks, which minimizes additional inspections resulting in reduced operational costs, less downtime, and increased safety. Such a crack monitoring system is not yet available and should be affordable, robust, wireless, and easy to install. The objective of this research is to select the most promising non-destructive evaluation method for a real-time crack monitoring system and to investigate its applicability for monitoring fatigue cracks in ship and offshore structures.

A literature review study of available and state-of-the-art non-destructive evaluation methods was conducted, which were then ranked based on seven criteria to determine their applicability for crack monitoring in ship and offshore structures. The Metal Magnetic Memory (MMM) method shows the greatest potential because it is intrinsically safe, no cleaning or polishing of the metal surface is required, and it is a passive method making it energy efficient and easy to install. The theoretical basis of the MMM method was then validated through an experiment and numerical simulation for a square steel plate with a slit that represents a through thickness fatigue crack. Magnetic Flux Leakage (MFL) was observed as a local positive and negative peak in the out-of-plane magnetic flux density on either side of the slit. As the specimen was not actively magnetized, this phenomenon is referred to as Self Magnetic Flux Leakage (SMFL).

Even though the theory behind the MMM method is well established and validated by means of an experiment, there are still many knowledge gaps that prevent a successful application to a crack monitoring system for ship and offshore structures because the SMFL is dependent on many unknown factors. First of all, the SMFL is induced by different sources of magnetization, such as the Earth magnetic

field, permanent magnetization, and stress-induced magnetization. On top of that, the Earth-induced SMFL varies in time due to changing geometry (crack opening and crack propagation) and changing background field (Earth field orientation), the stress-induced SMFL responds to changing stresses due to wave loading, and the permanent magnetization may slowly change due to ferromagnetic hysteresis effects. However, when only short-term effects are considered, the magnetization curve of ferromagnetic materials may be assumed linear for weak magnetic fields. Finally, most fatigue cracks in ship and offshore structures occur in welded joints due to stress concentration and initial material defects due to welding imperfection. It means that the geometry effects of welded joints and different magnetic material parameters of the welds need to be accounted for as well.

For unloaded plate specimens, the stress-induced magnetization equals zero and the induced and permanent magnetization can be separated from each other using two different experimental methods. The first method is to take magnetic measurements near the plate surface and repeating the same measurements with the plate rotated. If the plate is fully symmetric, the measured values can be separated into an induced part and a permanent part. It is demonstrated that this works well as error margins are within 20% when comparing the induced part with results from a Finite Element (FE) model for a square steel plate. The second method involves placing the specimen in a magnetic field simulator and taking magnetic measurements near the plate surface for a certain given background field and repeating the same measurements at zero magnetic field. This way, the permanent part of the magnetic measurements can be directly measured and subtracted from the initially measured values to obtain the induced part. This procedure was done for the square steel plate with a straight slit from the earlier experiment and error margins are within 5% when compared to results from an FE model when choosing an isotropic and homogeneous relative magnetic permeability of 225 for the plate material. Therefore, this method is more accurate than the first method and it can also be applied on specimens with any geometry, such as plates with cracks. From the results, it is also observed that the permanent magnetization can be of a larger magnitude than the induced magnetization and is typically non-uniformly distributed in steel plate specimens.

After it was demonstrated that the Earth-induced SMFL for a steel specimen can be accurately simulated by an FE model using a uniform relative magnetic permeability of 225, a numerical parametric study was performed to investigate the effects of altitude (distance between a sensor and the specimen's surface), Earth field orientation, crack opening, crack length, and geometries of welded joints on the Earth-induced SMFL. It was found that for increasing altitude, the SMFL signal strength decreases as a power function and the signal width increases linearly. The results also show that the signal strength is proportional to the effective background field that is

in-plane and perpendicular to the crack orientation and that larger crack sizes lead to larger SMFL signal strengths. Furthermore, it was demonstrated that for a double-sided and unpenetrated fillet welded steel T-joint with a through thickness crack at one weld toe in combination with realistic parameter values for crack size, Earth field orientation and altitude, the Earth-induced SMFL is strong enough to be measured with a small-size and inexpensive Hall effect sensor. One remark is that these sensors would need to be placed in close proximity to the crack, so also on top of the weld surface.

When a steel specimen is loaded, it experiences stresses, which induce a magnetization due to the magnetomechanical effect. To investigate the effect of this stress-induced magnetization on crack monitoring by the SMFL method, an experiment was conducted. A slender steel plate with an elliptical hole to create a stress concentration without experiencing crack opening effects was cyclically loaded in tension while measuring the out-of-plane magnetic flux density near the plate surface in a grid around the hole. The results show that the stress-induced magnetization varies cyclically with the loading frequency and forms a closed loop, so the effect was fully reversible. The spatial distribution of the measured stress-induced magnetic flux density was not symmetric around the elliptical hole, probably due to its dependency on the inhomogeneous permanent magnetization in the steel plate. The maximum change in measured SMFL due to applied tension up to the design yield stress was approximately 25 µT.

Finally, an experimental validation was conducted for the applicability of the SMFL method for monitoring real through thickness fatigue cracks in full-scale steel structures. Measurements of the out-of-plane magnetic flux density were performed on cracks in a suction hopper dredger and in a reconstructed steel bridge deck using a Hall effect sensor. The results from measurements in a grid with a spacing of 5 mm and altitude of 1 mm indicate clearly the location and size of the cracks. Compared to prior experimental results from small-scale specimens with artificial cracks, the observed signal strengths are much larger for the full-scale steel structures with real fatigue cracks. It means that the magnetization is much larger, and it is hypothesized that the permanent magnetization is dominant over the Earth-induced magnetization, which would make the crack monitoring system based on the SMFL method less susceptible to changing background fields.

It is concluded that a real-time crack monitoring system for ship and offshore structures based on the MMM method is feasible and can be affordable, robust, wireless, and easy to install. Some challenges have been investigated and can be mitigated by smart design of the sensor and intelligent data processing of the SMFL measurements. For example, the monitoring system should have sensors at an optimal

altitude by balancing sensor sensitivity and the amount of sensors needed, their sampling frequency should be dictated by the loading frequency to cope with crack opening, and a correction on the measured data may be needed to cope with changing orientation of the structure in the Earth's magnetic field. Additionally, the stress-induced magnetization may need to be taken into account for correct interpretation of the measured signals, depending on the application. For large steel structures such as a bridge or dredging ship with through thickness cracks, the measured signals are so strong that the stress-induced magnetization may be neglected. However, for other applications, such as semi-elliptical surface cracks, it may have a significant effect on the measured SMFL.

Samenvatting

Schepen en offshore constructies hebben last van vermoeiing vanwege cyclische belasting door golven. Om de integriteit van deze constructies te bewaken, worden daarom periodieke inspecties uitgevoerd gedurende de gehele levensduur van de constructie. Gedetecteerde vermoeiingsscheuren die te groot zijn om de veiligheid te kunnen garanderen moeten worden gerepareerd. Gedetecteerde scheuren met nog acceptabele afmetingen moeten tenminste meer frequent worden geïnspecteerd. Deze inspecties brengen veel kosten met zich mee, nemen veel tijd in beslag en kunnen gevaarlijke situaties opleveren. Om deze redenen moeten extra inspecties bovenop de periodieke classificatie inspecties zoveel mogelijk worden beperkt waar mogelijk.

Het onderzoek gepresenteerd in dit proefschrift stelt voor om een monitoring systeem te gebruiken voor reeds gedetecteerde scheuren. Dit minimaliseert het aantal benodigde inspecties, wat resulteert in lagere operationele kosten, minder uitvaltijd en hogere veiligheid. Een dergelijk monitoring systeem voor scheuren is nog niet beschikbaar en moet betaalbaar, robuust, draadloos en makkelijk te installeren zijn. Het doel van dit onderzoek is om de meest veelbelovende niet-destructieve onderzoeksmethode te selecteren voor een continu monitoring systeem en zijn toepasbaarheid voor het monitoring van vermoeiingsscheuren in schepen en offshore constructies te onderzoeken.

Een literatuurstudie is gedaan naar beschikbare en innovatieve niet-destructieve onderzoeksmethoden, welke vervolgens zijn gerangschikt op basis van zeven criteria om hun toepasbaarheid te toetsen voor het monitoren van scheuren in schepen en offshore constructies. De Metal Magnetic Memory (MMM) methode kwam daarin naar boven als meest veelbelovend vanwege de intrinsieke veiligheid, het niet hoeven behandelen van het metalen oppervlak en omdat het een passieve methode is waardoor het zeer energiezuinig en makkelijk te installeren is. De theorie achter de MMM methode is vervolgens gevalideerd door middel van een experiment en numerieke simulatie voor een vierkante stalen plaat met een sleuf door de gehele dikte, die een vermoeiingsscheur voorstelt. Magnetic Flux Leakage (MFL) was geconstateerd in de vorm van een positieve en negatieve piek in de magnetische fluxdichtheid loodrecht op het vlak nabij en aan weerszijden van de sleuf. Aangezien

het proefstuk niet actief was gemagnetiseerd spreekt men van Self Magnetic Flux Leakage (SMFL).

Ook al is de theorie achter de MMM methode bekend en gevalideerd door middel van een experiment, toch zijn er nog vele uitdagingen die een succesvolle implementatie naar een monitoring systeem voor scheuren in schepen en offshore constructies verhinderen, want de SMFL hangt af van verscheidene factoren. Ten eerste is de SMFL geïnduceerd door verschillende bronnen van magnetisatie, zoals het aardmagnetisch veld, de permanente magnetisatie en magnetisatie door mechanische spanning. Daarnaast varieert de aarde-geïnduceerde SMFL door veranderende geometrie (scheuropening en –propagatie) en veranderend achtergrondveld (oriëntatie in het aardmagnetisch veld), reageert de spanning-geïnduceerde SMFL op variërende spanningen door de golfbelasting en kan de permanente magnetisatie langzaam veranderen door ferromagnetische hysterese. Echter, wanneer alleen korte termijn effecten worden beschouwd, mag de magnetisatiecurve als lineair worden verondersteld voor zwakke veldsterktes. Tot slot, de meeste vermoeiingsscheuren in schepen en offshore constructies ontstaan in gelaste verbindingen vanwege hoge spanningsconcentraties en initiële defecten door lasimperfecties. Dit betekent dat de geometrische effecten van gelaste verbindingen en de andere magnetische parameters van het lasmateriaal ook moeten worden meegenomen.

Voor onbelaste proefstukken is de spanning-geïnduceerde magnetisatie nihil en kunnen de aarde-geïnduceerde en permanente magnetisatie van elkaar worden gescheiden door middel van twee verschillende experimentele methoden. De eerste methode is om magnetische metingen te doen nabij het plaatoppervlak en dezelfde metingen te herhalen terwijl de plaat geroteerd is. Indien het proefstuk volledig symmetrisch is, kunnen de metingen worden gescheiden in een geïnduceerd en permanent deel. Het is aangetoond dat dit werkt, aangezien de afwijking binnen 20% blijft in vergelijking tot resultaten uit een Finite Element (FE) model voor een vierkante stalen plaat en aangezien die afwijkingen voornamelijk nabij de randen van de plaat voorkomen. De tweede methode vereist plaatsing van het proefstuk in een magnetisch veld simulator. Magnetische metingen worden gedaan nabij het plaatoppervlak voor een gegeven achtergrondveld welke vervolgens worden herhaald in een magnetisch nulveld. Hierdoor kan het permanente deel van de metingen direct worden vastgesteld en worden afgetrokken van de initieel gemeten waarden om het geïnduceerde deel vast te stellen. Deze procedure is uitgevoerd voor de vierkante stalen plaat met een sleuf uit het eerdere experiment en de afwijking blijft nu binnen 5% in vergelijking tot FE resultaten bij een gekozen isotrope en homogene relatieve magnetische permeabiliteit van 225 voor het plaatmateriaal. Deze methode is dus nauwkeuriger dan de eerste methode en kan ook worden toegepast op proefstukken met elk gegeven geometrie, zoals bijvoorbeeld platen met scheuren. Kijkende naar de

resultaten kan ook geconstateerd worden dat de permanente magnetisatie groter kan zijn dan de geïnduceerde en dat deze gewoonlijk niet-uniform verdeeld is in stalen platen.

Nadat aangetoond is dat de aarde geïnduceerde SMFL voor een stalen proefstuk nauwkeurig gesimuleerd kan worden met een FE model met een uniforme relatieve magnetische permeabiliteit van 225, is een numerieke parametrische studie gedaan naar de effecten van sensorafstand (tot het plaatoppervlak), oriëntatie van het aardmagnetisch veld, scheuropening, scheurlengte en geometrieën van gelaste verbindingen op de aarde geïnduceerde SMFL. Resultaten laten zien dat voor toenemende sensorafstand, de SMFL signaalsterkte afneemt als een machtsfunctie en de signaalbreedte lineair toeneemt. Ook is aangetoond dat de signaalsterkte proportioneel is met het effectieve achtergrondveld wat in het vlak en loodrecht op de scheuroriëntatie staat, en hoe grotere scheurafmetingen tot hogere SMFL signaalsterktes leiden. Bovendien is aangetoond dat voor een T-verbinding met een dubbele niet volledig gepenetreerde hoeklas en een door de dikte lengtescheur in combinatie met realistische parameters voor de scheurafmetingen, oriëntatie van het aardmagnetisch veld en de sensorafstand, de aarde-geïnduceerde SMFL voldoende sterk is om gemeten te worden met een kleine en goedkope Hall effect sensor. Hiervoor is het wel noodzakelijk dat de sensoren dicht nabij de scheur geplaatst dienen te worden, dus ook op de hoeklas.

Als een stalen proefstuk wordt belast, dan ontstaan spanningen welke magnetisatie induceren door het magnetomechanische effect. Om het effect van spanning-geïnduceerde magnetisatie op scheur monitoring met de SMFL methode te onderzoeken, is een experiment uitgevoerd. Een slanke stalen plaat met een elliptisch gat, om een spanningsconcentratie te veroorzaken zonder dat scheuropening effecten een rol spelen, is cyclisch belast in trek terwijl de magnetische fluxdichtheid loodrecht op het plaatoppervlak is gemeten in een raster van punten rondom het gat. De resultaten laten zien dat de spanning-geïnduceerde magnetisatie cyclisch varieert met dezelfde frequentie als de belasting en een gesloten kring vormt, dus het effect was volledig omkeerbaar. De ruimtelijke verdeling van de gemeten spanning-geïnduceerde magnetische fluxdichtheid was niet symmetrisch rondom het gat, hetgeen waarschijnlijk te verklaren is door de afhankelijkheid van de niet uniform verdeelde permanente magnetisatie in de stalen plaat. De maximale verandering van de gemeten SMFL veroorzaakt door een trekspanning tot de ontwerp vloeigrens was ongeveer 25 µT.

Tot slot is er experimenteel onderzoek gedaan ter validatie van de toepasbaarheid van de SMFL methode voor het monitoren van echte vermoeiingsscheuren in stalen constructies op ware grootte. Metingen van de

magnetische fluxdichtheid loodrecht op het plaatoppervlak zijn verricht nabij scheuren in een sleephopperzuiger schip en in een reconstructie van een stalen brugdek met een Hall effect sensor. De resultaten van de metingen in een grid met tussenafstand van 5 mm en op een sensorhoogte van 1 mm van het oppervlak laten duidelijk de locatie en de lengte van de scheuren zien. Vergeleken met eerdere experimentele resultaten van proefstukken op kleinere schaal en met een gemaakte scheur, zijn de geobserveerde signaalsterktes veel hoger voor stalen constructies op ware grootte met echte vermoeiingsscheuren. Het blijkt dus dat de magnetisatie veel groter is en de hypothese is dat de permanente magnetisatie dominant is over de aarde-geïnduceerde magnetisatie. Dit zou betekenen dat het monitoring systeem voor gedetecteerde scheuren gebaseerd op de SMFL methode niet heel gevoelig zal zijn voor variërende achtergrondvelden.

De conclusie luidt dat een monitoring systeem voor gedetecteerde scheuren in schepen en offshore constructies gebaseerd op de MMM methode haalbaar is en dat het betaalbaar, robuust, draadloos en makkelijk te installeren kan zijn. Een aantal uitdagingen zijn onderzocht en kunnen worden verholpen door het optimaal ontwerpen van de sensor en intelligente dataverwerking van de SMFL metingen. Bijvoorbeeld, het monitoring systeem moet sensoren hebben op een optimale afstand van het plaatoppervlak om de juiste balans te vinden tussen sensorgevoeligheid en het aantal benodigde sensoren, de meetfrequentie moet bepaald worden aan de hand van de belastingfrequentie om rekening te houden met scheuropening effecten en een correctie op de gemeten data is wellicht noodzakelijk om rekening te houden met de oriëntatie van de constructie in het aardmagnetisch veld. Daarnaast kan het belangrijk zijn om de spanning-geïnduceerde magnetisatie in acht te nemen voor correcte interpretatie van de gemeten signalen, afhankelijk van de toepassing. Voor grote stalen constructies zoals een brug of een baggerschip zijn de gemeten signalen zo hoog dat de spanning-geïnduceerde magnetisatie een verwaarloosbaar effect heeft, maar voor andere toepassingen, zoals bijvoorbeeld semi-elliptische oppervlaktescheuren, kan het zeker een significant effect hebben op de gemeten SMFL.
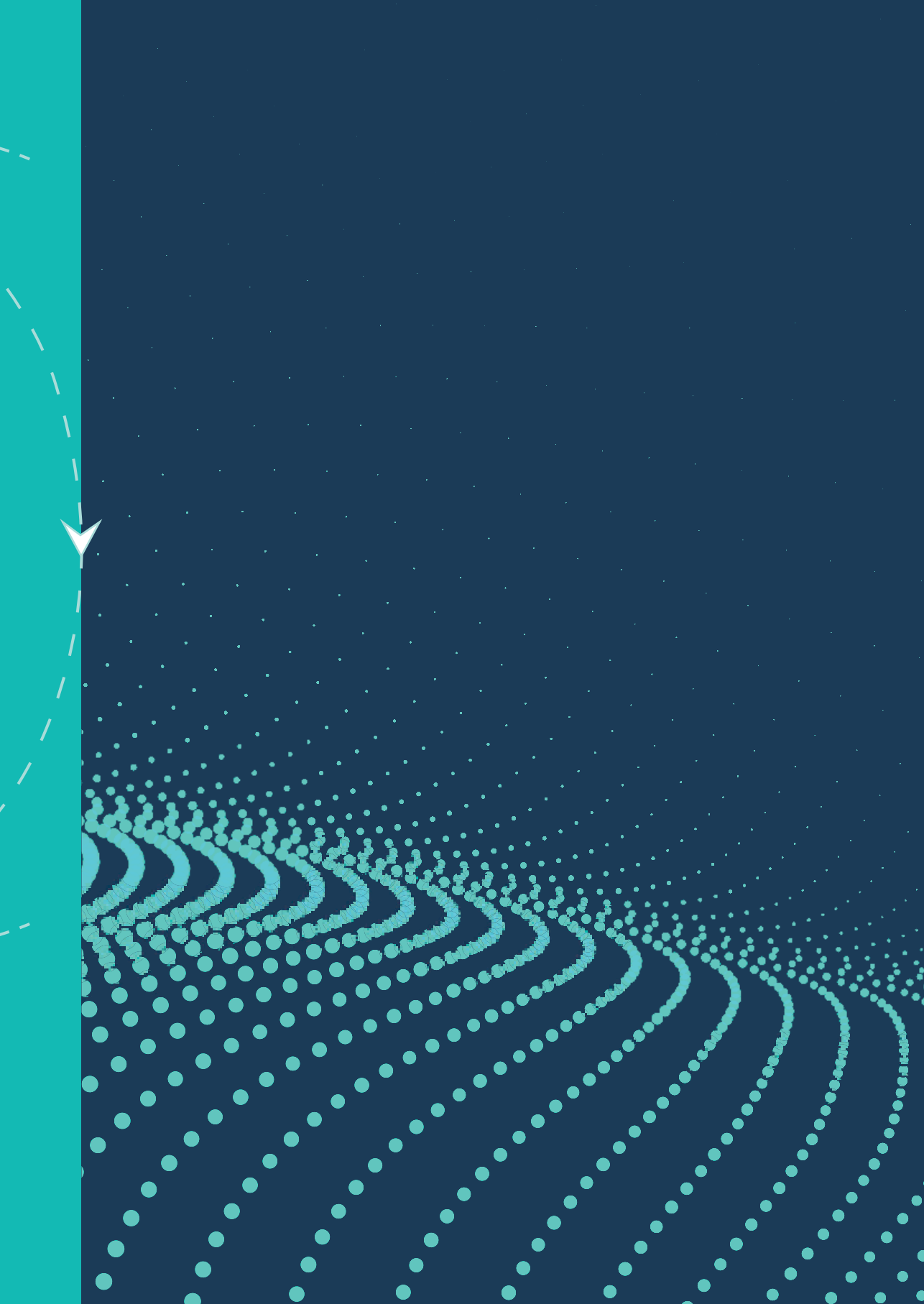
1

Introduction

1.1. Motivation

Marine structures, such as ships and offshore platforms (see Figure 1.1 for examples), are complex engineering systems of great economic importance. These structures need to be designed, operated, and maintained in such a way that they are safe to the public and to the environment. Therefore, rules and guidelines have been developed over the past decades to ensure their structural integrity [1–4]. The rules, in general, allow for defects which do not jeopardize safe operation [5].
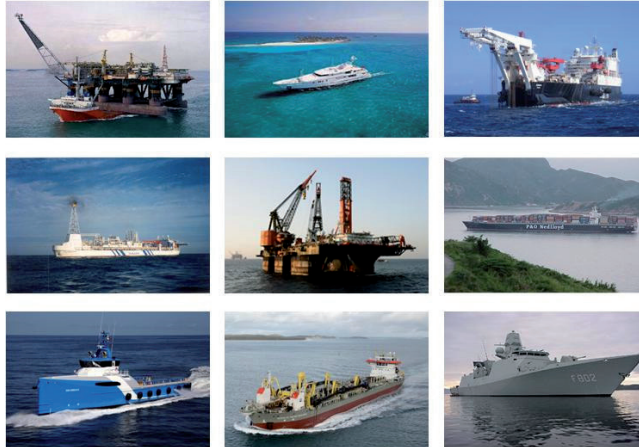
Figure 1.1: Examples of ship and offshore structures.

Fatigue cracks are common defects found in ship and offshore structures due to the cyclic nature of wave loading. The growing application of high strength steels makes fatigue an even more critical failure mode. As fatigue cracks initiate and grow, operators of ship and offshore structures are obliged to perform inspection periodically [6]. Cracks that are too long for safe operation must be repaired. Cracks of an acceptable length must be inspected more frequently [7]. However, crack growth rates are often uncertain [8], despite many efforts in developing predictive models for crack growth and crack propagation using fracture mechanics theory. This means that it is not known when the cracks reach their critical lengths. Crack prediction models can possibly be improved by taking multiaxial stress states into account, which is currently being worked on by Van Lieshout *et al.* [9,10]. For now, most operators adopt a conservative approach by either increasing the inspection frequency or reducing the allowable crack length.

The cost of a typical single tank inspection on an FPSO (Floating Production Storage and Offloading) is approximately 100,000 USD, so increasing the inspection frequency would lead to significantly higher operational costs. Additionally, ships and

offshore platforms are mostly at sea, so an inspection would need to happen in dry dock or during operation, causing significant downtime. These inspections can also be hazardous as they typically involve sending people into dark and confined spaces and often require rope access and scaffolding.

Interviews with asset owners and operators of ship and offshore structures revealed that they seek an affordable, simple, and robust system for monitoring detected cracks in ship and offshore structures. Such a system should detect when a crack has reached its predefined unacceptable length and communicate this wirelessly to the operator. The overall cost of the system should be competitive with the cost of additional visual inspection by a surveyor. Therefore, the goal of the CrackGuard Joint Industry Project (JIP), supported by various industry partners, is to conduct precompetitive research and to develop an affordable system for monitoring cracks. The research described in this thesis is part of the CrackGuard JIP.

A real-time crack monitoring system could provide more frequent and more reliable information on a detected crack's criticality without any additional inspections by surveyors. Therefore, such a system could guarantee the structural integrity of ship and offshore structures in a more effective way, leading to reduced operational costs and increased safety. A schematic overview of the envisaged crack management with intervention by CrackGuard for cracks with medium or high risk levels is shown in Figure 1.2.
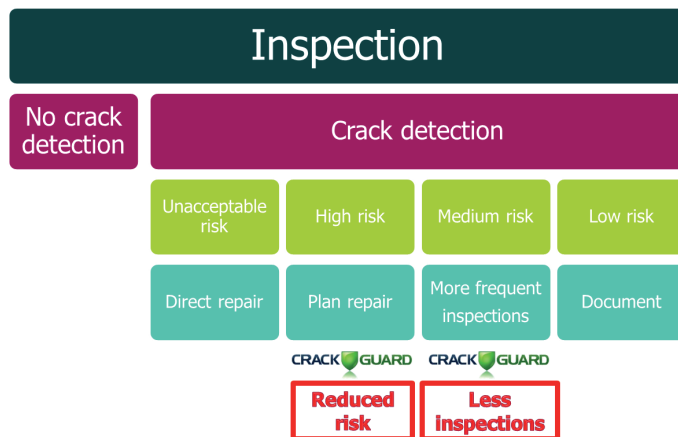

Figure 1.2: Envisaged crack management scheme.

1.2. Research Objective

The objective of the research presented in this thesis is to select the most promising non-destructive evaluation method for a real-time crack monitoring system and to investigate its applicability for monitoring fatigue cracks in ship and offshore structures.

1.3. Thesis Outline

Chapter 2 gives a review of available and state-of-the-art non-destructive evaluation methods and selects the most promising method for monitoring cracks in marine structures. The theoretical basis of the selected method, the Metal Magnetic Memory method, is then validated through an experiment and numerical simulation in Chapter 3. Chapter 4 focuses on which magnetic material parameters to choose for structural steels in order to numerically simulate the Self Magnetic Flux Leakage accurately. These material parameters are then used in Chapter 5 to analyze the Earth-induced Magnetic Flux Leakage by finite element simulation. Chapter 6 investigates the effect of stress-induced magnetization on crack monitoring using Self Magnetic Flux Leakage measurements. A full-scale experimental study on Self Magnetic Flux Leakage near real fatigue cracks in steel structures is presented in Chapter 7. Finally, the conclusions are summarized in Chapter 8, which also discusses the implications of this research and gives some recommendations for future work.

1.4. References

[1]   IACS. Common Structural Rules for Bulk Carriers. 2006.

[2]   IACS. Common Structural Rules for Double Hull Oil Tankers. 2006.

[3]   Fricke W, Bronsart R. Proceedings of the 18th International Ship and Offshore Structures Congress. Proc. 18th Int. Sh. offshore Struct. Congr., vol. 1, Schiffbautechnische Gesellschaft e.V.; 2012.

[4]   Fricke W, Bronsart R. Proceedings of the 18th International Ship and Offshore Structures Congress. Proc. 18th Int. Sh. Offshore Struct. Congr., vol. 2, Schiffbautechnische Gesellschaft e.V.; 2012.

[5]   ABS. Guide for Nondestructive Inspection of Hull Welds. Houston, TX: 2011.

[6]   ABS. Guide for Hull Inspection and Maintenance Program. Houston, TX: 2013.

1

[7]   DNV-GL. Probabilistic methods for planning of inspection for fatigue cracks in offshore structures. 2015. doi:10.1016/j.marstruc.2016.02.002.

[8]   Matthies HG, Brenner CE, Bucher CG, Guedes Soares C. Uncertainties in probabilistic numerical analysis of structures and solids-Stochastic finite elements. Struct Saf 1997;19:283–336. doi:10.1016/S0167-4730(97)00013-1.

[9]   Van Lieshout PS, Den Besten JH, Kaminski ML. Comparative study of multiaxial fatigue methods applied to welded joints in marine structures. Frat Ed Integrita Strutt 2016;10:173–92. doi:10.3221/IGF-ESIS.37.24.

[10]   van Lieshout PS, den Besten JH, Kaminski ML. Multiaxial fatigue assessment of welded joints in marine structures. Int Shipbuild Prog 2017;0:1–43. doi:10.3233/ISP-170141.
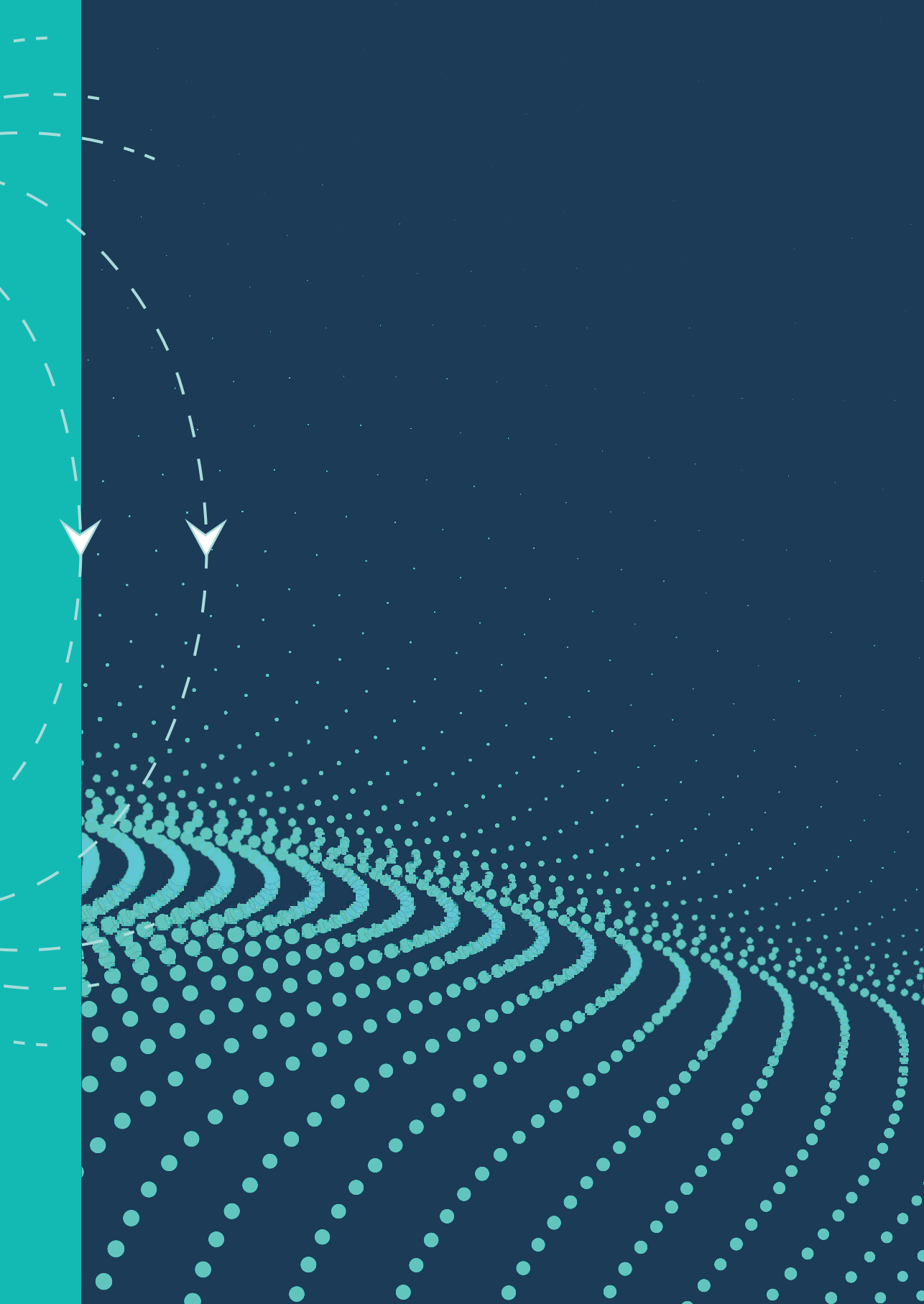
2

Selection of Metal Magnetic Memory Method for Fatigue Crack Monitoring in Marine Structures

Abstract

Monitoring of detected cracks can ensure the structural integrity of marine structures in a more effective way. The envisaged crack monitoring system needs to be affordable, robust, wireless, and easy to install. Such systems are not yet available. This chapter gives a review of non-destructive evaluation (NDE) technologies that can potentially be used for monitoring cracks. The NDE technologies are ranked based on seven criteria, which results in the magnetic methods showing the greatest potential because of their intrinsic safety and no cleaning or polishing of the metal surface is required. In particular, the Metal Magnetic Memory method is a suitable method for the application considered here, as it is a passive method. Therefore, a crack monitoring system based on this method can be easier to install and can be wireless due to higher energy efficiency.

Keywords

Marine structures; fatigue crack monitoring; non-destructive evaluation; structural integrity; magnetic flux leakage; metal magnetic memory.

2.1. Introduction

To assess the condition of marine structures [1], non-destructive evaluation (NDE) methods have been developed for characterizing materials and detecting the presence of defects, such as cracks. NDE was once an empirical technology that required subjective judgment of surveyors. Examples of such methods are dye penetrant inspection, magnetic particle inspection, and imaging techniques like microscopy. For simple applications, these methods give acceptable results. For more complex applications, however, there is a growing need for *"quantitative measurement techniques, physical models for computational analysis, statistical considerations, quantitative designs of measurement systems, specifications for flaw detection and characterization, system validation and performance reliability"* [10, p. 13-14]. Other studies also explicitly mentioned the need for on-line monitoring techniques, especially for monitoring fatigue cracks [3,4].

This chapter reviews conventional and recent NDE methods and evaluates their applicability for a novel crack monitoring system that is affordable, robust, wireless, and easy to install. The aim of the chapter is to select the best measurement method for crack monitoring in marine structures.

Section 2.2 gives a review on the state-of-the-art in non-destructive evaluation. Four different methods are discussed in the subsections. In section 2.3, these methods are ranked on their applicability for a crack monitoring system on board of a marine structure. Finally, there is a conclusion, which will also elaborate on the implications of the availability of the intended crack monitoring system on risk based inspections and existing structural health monitoring systems.

2.2. Potential NDE Methods

2.2.1. Ultrasonic Testing

The basic idea of ultrasonic testing is that an ultrasonic sound wave is introduced in a concerned material and when a discontinuity is present in the wave path, part of the wave reflects back from the flaw surface. The location of the flaw can be determined because the direction of the wave and the signal travel time are known. Sometimes, other flaw properties, such as its size and orientation, can be retrieved from the reflected signal. Some of the advantages of ultrasonic inspection are its sensitivity to both surface and subsurface discontinuities, its depth of penetration, its

high accuracy in determining the location and size of flaws, and it gives instantaneous results.

However, there are also some drawbacks of ultrasonic testing. The most important drawback is that it normally requires a coupling medium to promote the transfer of sound energy into the test specimen. Usually, piezoelectric transducers are used with water coupling in an immersion tank. Another option is to have direct contact by using contact transducers. A recurring problem with contact transducers is the quality of the thin coupling layer between the transducer and the structure. The thickness and homogeneity of coupling layers is difficult, if not impossible, to control. Achenbach states that it is particularly difficult if the transducers have to be moved during the testing procedure to optimize the position for signal reception [2]. On the other hand, using an immersion tank would be even less suitable for in-service testing. Hence, methods of generating ultrasound in a non-contact manner are of increasing interest.

The following ultrasonic methods are discussed below: laser-based ultrasonics and air-coupled ultrasonics.

❖   **Laser-Based Ultrasonics**

The advantage of using an ultrasonic generator is that it can be remote from the test sample under investigation. Most detectors of acoustic pulses are of a contacting nature; thereby, they are perturbing the original characteristics of the acoustic pulse. If a laser interferometer is used instead, the detection system can also be made remote, and some of the output optics can be made integral with the laser generator. Aindow *et al.* did experimental research on subsurface flaw characterization with laser-based ultrasonics [5]. It was shown that a two-laser system can be used for remote characterization of flat-bottomed holes, which act as subsurface flaws within an aluminum test sample.

There are also some disadvantages of using laser detection. It requires polishing of the metal surface to reflect sufficient light, which is highly impractical when used for in-service testing of marine structures. The laser detector is also known to be not as sensitive as other ultrasonic detectors.

❖   **Air-Coupled Ultrasonics**

Over the past decades, there have been significant advances in the state-of-the-art of air-coupled ultrasonic inspection systems, resulting in practical industrial applications of the technology. Air-coupled ultrasonic inspection can be regarded as a non-contact or minimally-invasive method because the coupling medium (air or

another gas) is part of the natural environment and, therefore, no additional physical contact is required. The use of air-coupling is particularly attractive because it results in ultrasonic probing signals whose temporal and spatial characteristics are similar to those generated using water-coupling [6]. It is imperative that gases and liquids exhibit substantially different specific densities and sound speeds, which can result in practical advantages as well as limitations. The biggest obstacle of air-coupled ultrasonic testing is that the received signal amplitude is affected by transmission losses at the air/solid interfaces. The sensitivity of this system is therefore negatively affected. Air-coupled ultrasonic NDE has been enabled by the availability of transducers of the generation and reception of ultrasound, which are the most critical components of the air-coupled ultrasonic NDE system. Grandia & Fortunko discussed six types of electro-acoustic transducers that are potentially of interest: electrostatic, variable reluctance, moving coil, piezoelectric, electrostrictive, and magnetostrictive [6]. For NDE systems, the piezoelectric transducer appears to be of most interest.

2.2.2. Radiographic Testing

X-rays and gamma-rays are of the same nature as light since they are electromagnetic waves but with much shorter wave-lengths. This allows X-rays and gamma-rays to penetrate in a lot of materials, which makes them suitable for non-destructive testing. This is called radiographic testing. The electromagnetic radiation, which consists of high energy photons, can be generated by an X-ray machine or a radioactive source. With a detecting device, the amount of radiation that travelled through the test specimen can be measured and projected onto a film. This results in a latent image of varying densities according to the amount of radiation reaching each area. This image is called a radiograph. Such a radiograph contains enough information about the test specimen that flaws can be detected.

❖ **X-Ray Backscatter Tomography**

Computed tomography uses multiple X-ray transmission projections and mathematical reconstruction methods to create a tomograph representing a slice through the object [7]. These two-dimensional radiographic projections of a sample are used to reconstruct a three-dimensional map of the X-ray attenuation coefficient of the material. Due to the availability of new synchrotron X-ray sources and new detectors, reconstructed 3D images with a spatial resolution close to 1 μm can be obtained. Because of its great sensitivity and high resolution, this technique is used for the observation of the early stages of nucleation and growth of short fatigue cracks [8].

A less known property of X-rays is that they can carry information regarding material composition and structure when scattered. This property can be exploited since X-rays are scattered in all directions, which is very useful in case transmission methods are not feasible. However, the backscatter inspection method suffers from inherent limitations, notably with respect to depth penetration and various image artifacts.

An alternative approach uses highly collimated source and detector beams, as shown in Figure 2.1. It is then possible to measure a scatter signal from the volume element defined by the intersection of both beams. When these measurements are done for each volume element in a plane within the object, the data can be displayed as a tomograph [7]. Such a process is referred to as X-ray backscatter tomography (XBT), which combines the best of the two methods described earlier.
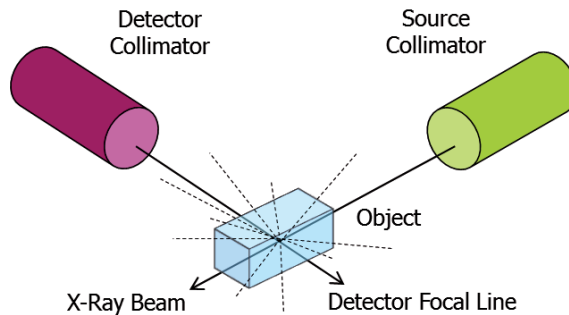

Figure 2.1: Principle of collimated scatter detection, based on [7].

XBT can be an ideal NDE method but it is limited to applications that require only an image representing a density distribution. Furthermore, XBT is limited to the range of materials and depths of inspection from which a measurable signal can be obtained. According to Poranski, Greenawald & Ham, these limitations are due to effects of attenuation. They also state that the inspection of dense materials, such as steel, is limited to a depth of 5 mm from the surface [7].

2.2.3. Eddy Current Testing

Eddy current methods for non-destructive evaluation are often seen as magnetic methods. Strictly speaking, these methods do not depend on any inherent magnetic properties of the material and can be applied to any conducting material [9]. Therefore, eddy current testing is treated here as a separate class of NDE.

In eddy current testing, electrical currents are generated in a conductive material as a result of a time-varying magnetic field. These eddy currents can be

measured by plotting a complex impedance plane map. Material defects, such as cracks, cause interruptions in the flow of the eddy currents. *"This results in a different complex impedance of the eddy current pick-up coil when it is positioned over the flaw compared with when it is positioned over an undamaged region of the material"* [18, p. 89]. For non-magnetic materials, the interpretation of results is quite straightforward; for ferromagnetic materials, the interpretation is more complex as the response depends on the material's magnetic permeability. Jiles states in his review article that eddy currents can also be used for measuring the thickness of coatings, determining permeability and conductivity, evaluating changes in heat treatment and microstructure, and estimating tensile strength, chemical composition and ductility [9]. A more comprehensive review on quantitative eddy current non-destructive evaluation was published by Auld & Moulder, who elaborated on numerical methods as well as analytical expressions for both the forward and inverse problem for eddy current testing [10].

❖ **Pulsed Eddy Current Testing**

Where conventional eddy current testing uses sinusoidal alternating electrical current of a certain frequency, the pulsed eddy current technique applies a step function voltage to excite the probe. The advantage is that the step function has a continuous spectrum of frequency components. Therefore, the electromagnetic response to multiple frequencies can be measured with a single step. Since the penetration depth is dependent on the frequency of excitation, information over a range of depths can instantly be obtained. Furthermore, the starting time and intensity of a pulsed excitation can easily be controlled, and the system is less vulnerable to interference [11].

2.2.4. Magnetic Testing

The last but very promising class of NDE methods discussed here is based on the material's magnetic properties. These methods are limited to materials that are ferromagnetic. A figure in which almost all magnetic properties can be found is the hysteresis curve. Hysteresis in general is the dependence of a system not only on its current environment but also on its past environment, so it reflects the ability of retaining magnetic properties. The main mechanisms that cause the hysteresis property of ferromagnetic materials are domain wall bulging, which is a reversible process, and domain wall displacement, which is an irreversible process [12]. Impedance to these mechanisms is caused by pinning sites that can be small defects or precipitates.

There exists no general form of the hysteresis loop for ferromagnetic materials but frequently it is in the shape of a sigmoid. A typical hysteresis loop can be seen in Figure 2.2.
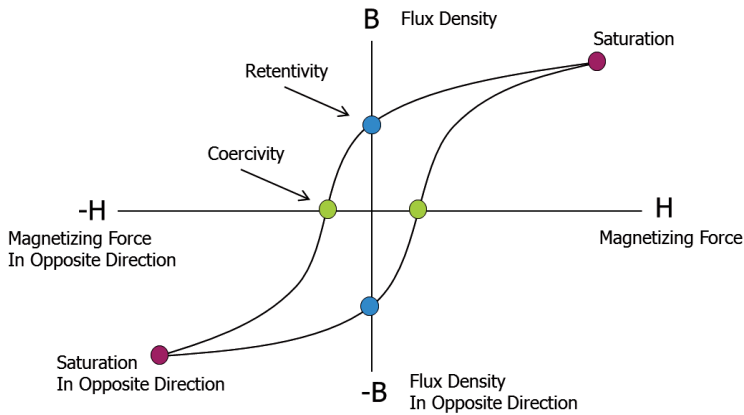

Figure 2.2: Typical hysteresis curve, based on [13].

All the magnetic properties of a material (e.g. retentivity, coercivity, saturation, permeability) that are reflected by the hysteresis curve appear to be related to its mechanical properties. For mechanical properties, one can think of grain size, hardness, precipitates, defects, and residual strains. These properties affect the mechanisms behind the hysteresis property, namely domain wall bulging and domain wall displacement. Because magnetic and mechanical properties are interrelated, it is possible to do non-destructive evaluation based on magnetism.

❖ **Magnetic Particle Inspection**

The magnetic NDE method most widely used in practice is magnetic particle inspection (MPI), mainly because of its apparent simplicity. The method depends on the leakage of magnetic flux at the surface of a magnetized ferromagnetic material in the vicinity of surface-breaking or near-surface flaws [9], see Figure 2.3. The flux leakage occurs due to the abrupt change of magnetic permeability around the flaw. The greatest advantage of MPI is that it gives a direct visual indication of the location and size of a flaw or crack.

However, the process is influenced by a large number of variables, which need careful control to obtain repeatable and reliable results. Skeie & Hagemaier state that the critical parameters for the performance of MPI are the magnetic particles themselves, particle concentration, illumination, current density, field direction, and

human factors [14]. Most importantly, the MPI method does not allow for quantitative measurements; it requires the subjective judgment of surveyors.
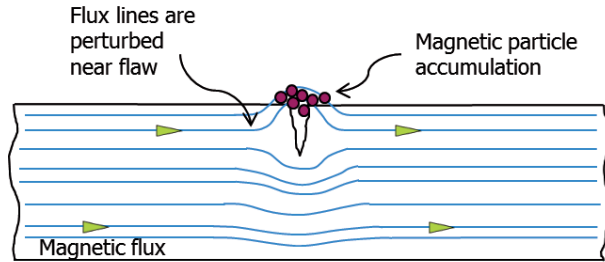

Figure 2.3: Schematic diagram of flux leakage in the vicinity of a surface-breaking flaw with accumulation of magnetic particles, based on [9].

❖ **Magnetic Flux Leakage Technique**

Jiles' review on magnetic methods for non-destructive evaluation [9] describes how MPI can be made quantitative by measuring the magnetic flux leakage with a magnetometer that scans the surface of the specimen, see Figure 2.4. This method is referred to as Magnetic Flux Leakage (MFL) testing. By scanning the surface with a magnetometer, the typical search coil output (out-of-plane) in the vicinity of a crack is shown in Figure 2.5, which also plots the flux leakage. From the figure, it can be observed that where the flux leakage is maximal, the output voltage reaches a peak value and undergoes a sign change. This can be explained by the existence of a local magnetic North and South pole on both sides of the crack.
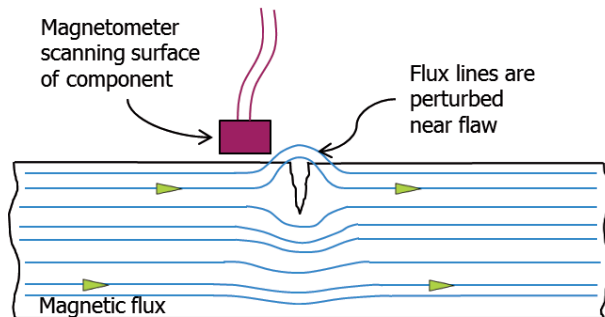

Figure 2.4: Scanning the surface of a specimen with a magnetometer to detect flaws, based on [9].
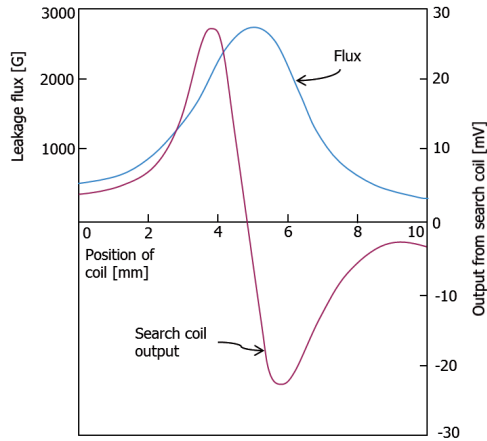
Figure 2.5: Variation of flux leakage as a function of the coil position, based on [15].

The potential of the MFL technique has been recognized by many other researchers who have performed experimental and numerical studies [16–22], with the aim of applying this method in practice. Altschuler & Pignotti researched MFL testing specifically for the application of flaw detection in steel pipes. They calculated a typical MFL output signal, see Figure 2.6, using a finite element model [23]. This finding is comparable to the search coil output from Figure 2.5. Real applications of MFL testing have recently been developed, for example for the in-line inspection industry of steel pipes. ROSEN Technology and Research Center in Germany developed a single in-line inspection tool that combines MFL and ultrasonic testing to improve the probability of detection and the sizing model [24].
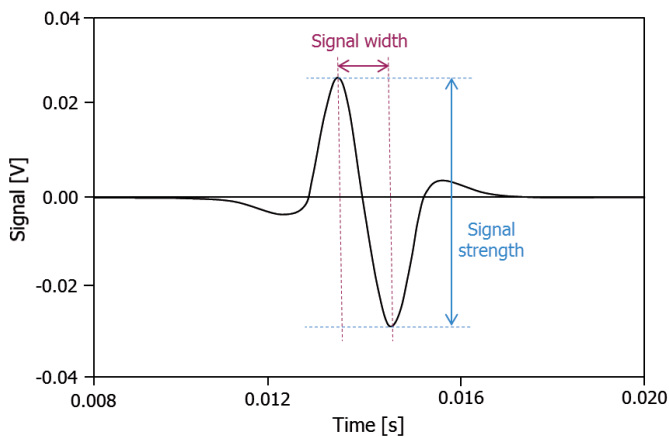

Figure 2.6: Typical MFL signal calculated with a finite element model, based on [23].

❖ **Metal Magnetic Memory Method**

The Metal Magnetic Memory (MMM) technique was first developed by Dubov [25]. This method is based on the Self Magnetic Flux Leakage (SMFL) principle, which is the same principle as MFL but without actively magnetizing the specimen. Instead, it uses the Earth's magnetic field as its only external source, which makes the MMM technique a passive magnetic NDE method. Besides the Earth's magnetic field, there are also internal magnetization sources, such as permanent magnetization due to remanence, and stress magnetization.

Wang *et al.* did theoretical research [26] to come up with a reliable model to study the relationship between SMFL signals and stress concentrations. Nevertheless, most of the work has been experimental research. It has been shown that although the Earth's magnetic field is very weak, the distribution of magnetic flux on the surface of ferromagnetic materials was significantly disturbed near a flaw [27]. In that same paper, fatigue tests were conducted on pre-notched specimens in which the out-of-plane magnetic memory signals were measured. The results for one of the pre-notched specimens can be found in Figure 2.7.

One can see the resemblance with the signals in Figures 2.5 and 2.6. With increasing load cycles, the signal strength increases as well. Lihong *et al.* also plotted the crack length propagation against the signal strength, see Figure 2.8. Based on these results, the authors even stated that the relation between the signal strength and the crack length is a good linear fit. If this relation is truly linear, the crack length can be accurately estimated with just two measurement points along the crack.
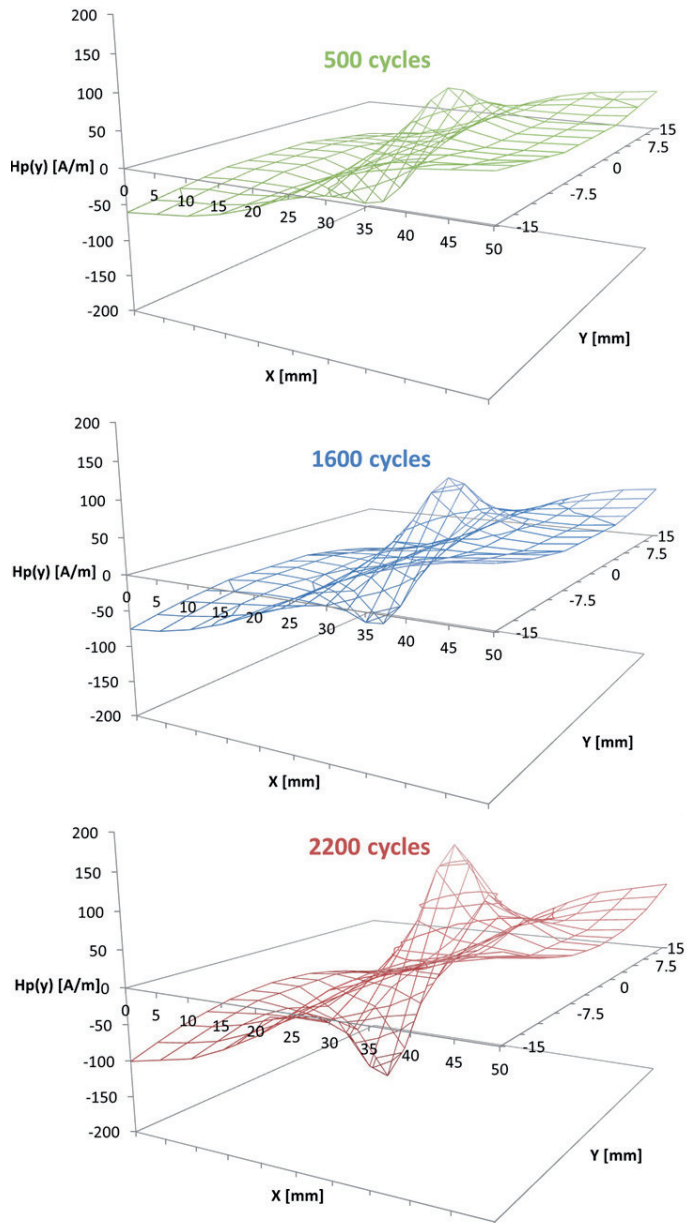
Figure 2.7: Out-of-plane magnetic flux density distribution on the surface of one specimen at different stages of its fatigue life, based on [27].
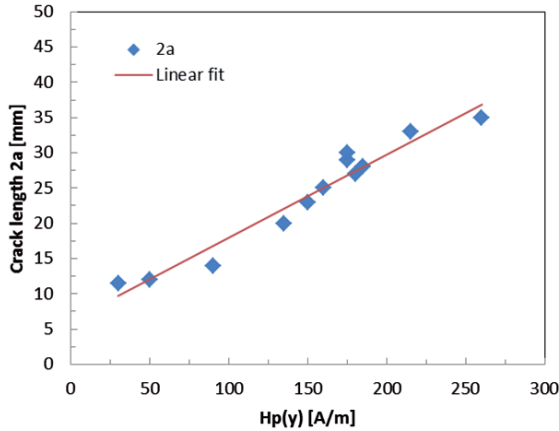
Figure 2.8: The relation between peak-to-peak $H_p(y)$ and crack length 2a of a specimen, based on [27].

2.3. Ranking NDE Technologies

The NDE technologies reviewed in the previous section need to be assessed with regards to the application of a monitoring system of detected cracks in marine structures. The seven criteria that are important in ranking sensor technologies are sensitivity, ruggedness, SHE (Safety, Health and Environment), power, automation, cost, and installation [28]. The results of the assessment are shown in Table 2.1.

	Ultrasonic	X-ray	Eddy Current	Magnetic
Sensitivity	++	++	+	+
Ruggedness	+/-	+/-	+	+/-
SHE	+	- -	- -	+
Power	+/-	-	-	+
Automation	+	- -	+	+
Cost	+/-	-	+	++
Installation	- -	- -	+	+

Table 2.1: Ranking NDE technologies for application of crack monitoring system for marine structures.

Sensitivity, ruggedness, and SHE are the most important criteria. The sensitivity determines how small of a crack can be monitored. All of the technologies are sensitive enough to monitor cracks that surveyors were already able to detect. In terms of ruggedness, the technologies do not differ much. For SHE, however,

radiographic testing and eddy current testing have clear shortcomings when they are applied on board of tankers or offshore structures that are in operation and have to be intrinsically safe in accordance with explosion protection guidelines, such as the ATEX guidelines for devices of the European Union [29]. X-ray testing has the major hazard of human exposure to radiation and eddy current testing can cause sparks, which is extremely dangerous when applied in an explosive environment such as a tank that contains flammable liquids or gases. Because increasing safety is one of the main reasons for developing a crack monitoring system, these two technologies are not suitable.

This leaves the ultrasonic and magnetic methods. The difference between these methods is most clear when considering the installation criterion. For ultrasonic testing, rather large equipment is needed to introduce the ultrasonic waves into the object and also to detect the reflected waves. Magnetic fields, on the other hand, are always present due to the Earth's magnetic field. Therefore, a crack monitoring system based on a magnetic NDE method can be passive and, for that reason, will be easier to install. The possibility of passive measuring also results in less power consumption when compared to ultrasonic testing, which creates the opportunity to implement it in a monitoring system that is wireless.

Lastly, magnetic methods do not require any surface preparation such as cleaning or polishing, unlike ultrasonic testing. Ship and offshore structures are always coated for protection against corrosion, and cracks are often found in tanks which carry oil, gas or dry cargo. Not having to clean or polish the surface is another advantage of magnetic testing.

One obvious limitation of the magnetic methods is that they can only be applied to ferromagnetic materials. Fortunately, most marine structures like ships and offshore platforms are made of steel, which is a ferromagnetic material as long as it is not stainless steel.

2.4. Conclusions

A literature review study has shown that magnetic non-destructive evaluation methods are most suitable for monitoring detected cracks in marine structures. Main arguments for choosing magnetic methods are their intrinsic safety and not having to clean or polish the surface under investigation. In particular, the Metal Magnetic Memory method shows great potential as it is a passive method, which means that no external magnetic source is required. The principle is the same as for Magnetic Flux

Leakage testing but it requires no active magnetization. Therefore, the name Self Magnetic Flux Leakage is introduced. Possible advantages of a passive crack monitoring system include increased battery life, wireless capability, more robust design, easier installation, and cost reduction.

Furthermore, the system could be linked with existing structural health monitoring systems, such as Monitas and Risk Based Inspection (RBI). The Monitas system presents, explains, and advises on the fatigue lifetime consumption of ship hulls based on the comparison between the design and the actual lifetime calculated by a fatigue design tool that uses measured data [30–33]. Within RBI, the probability of fatigue failure of detected and unrepaired cracks is conditioned on inspection results so that inspection intervals can be adjusted according to the inspection outcome [34]. Linking these systems with a crack monitoring system would result in a more rational advice, which would ultimately lead to optimized operational cost, less downtime, and safer operation.

2.5. References

[1]   Rizzo CM, Paik JK, Brennan F, Carlsen C a., Daley C, Garbatov Y, et al. Current practices and recent advances in condition assessment of aged ships. Ships Offshore Struct 2007;2:261–71. doi:10.1080/17445300701423486.

[2]   Achenbach J. Quantitative nondestructive evaluation. Int J Solids Struct 2000;37:13–27. doi:10.1016/S0020-7683(99)00074-8.

[3]   Bea RG. Marine Structural Integrity Programs. Mar Struct 1994;7:77–90. doi:10.1016/0951-8339(94)90011-6.

[4]   Vanlanduit S, Guillaume P, Linden G Van Der. On-line monitoring of fatigue cracks using ultrasonic surface waves. NDT E Int 2003;36:601–7. doi:10.1016/S0963-8695(03)00082-3.

[5]   Aindow AM, Dewhurst RJ, Palmer SB, Scruby CB. Laser-based non-destructive testing techniques for the ultrasonic characterization of subsurface flaws. NDT Int 1984;17:329–35. doi:10.1016/0308-9126(84)90141-X.

[6]   Grandia WA, Fortunko CM. NDE applications of air-coupled ultrasonic transducers. Proc. IEEE Ultrason. Symp., vol. 1, IEEE; 1995, p. 697–709.

[7]   Poranski CF, Greenawald EC, Ham YS. X-Ray Backscatter Tomography: NDT Potential and Limitations. Mater Sci Forum 1996;210–213:211–8. doi:10.4028/www.scientific.net/MSF.210-213.211.

[8]   Marrow TJ, Buffiere JY, Withers PJ, Johnson G, Engelberg D. High resolution X-

ray tomography of short fatigue crack nucleation in austempered ductile cast iron. Int J Fatigue 2004;26:717–25. doi:10.1016/j.ijfatigue.2003.11.001.

[9]   Jiles DC. Review of magnetic methods for nondestructive evaluation. Ndt Int 1990;21:311–9. doi:10.1016/0308-9126(88)90189-7.

[10]   Auld BA, Moulder JC. Review of advances in eddy current nondestructive evaluation. J Nondestruct Eval 1999;18:3–36. doi:10.1023/a:1021898520626.

[11]   Tian GY, Sophian A. Defect classification using a new feature for pulsed eddy current sensors. NDT E Int 2005;38:77–82. doi:10.1016/j.ndteint.2004.06.001.

[12]   Jiles DC, Atherton DL. Theory of ferromagnetic hysteresis (invited). J Appl Phys 1984;55:2115–20. doi:10.1063/1.333582.

[13]   NDT Resource Center n.d. https://www.nde-ed.org/EducationResources/CommunityCollege/MagParticle/Physics/HysteresisLoop.htm (accessed June 23, 2016).

[14]   Skeie K, Hagemaier DJ. QUANTIFYING MAGNETIC PARTICLE INSPECTION. Mater Eval 1988;46:779–85.

[15]   Beissner RE, Matzkanin GA, Teller CM. NDE Applications of Magnetic Leakage Field Methods: A State-of-the-art Survey. 1980.

[16]   Wang ZD, Gu Y, Wang YS. A review of three magnetic NDT technologies. J Magn Magn Mater 2012;324:382–8. doi:10.1016/j.jmmm.2011.08.048.

[17]   Sophian A, Tian GY, Zairi S. Pulsed magnetic flux leakage techniques for crack detection and characterisation. Sensors Actuators, A Phys 2006;125:186–91. doi:10.1016/j.sna.2005.07.013.

[18]   Udpa S, Afzal M. Advanced signal processing of magnetic flux leakage data obtained from seamless gas pipeline. NDT E Int 2002;35:449–57. doi:10.1016/S0963-8695(02)00024-5.

[19]   Van der Horst MP, Kaminski ML, Lepelaars E. Testing and Numerical Simulation of Magnetic Fields Affected by Presence of Fatigue Cracks. Proc. Int. Offshore Polar Eng. Conf., Busan, South-Korea: International Society of Offshore and Polar Engineers; 2014, p. 445–50.

[20]   Li Y, Wilson J, Tian GY. Experiment and simulation study of 3D magnetic field sensing for magnetic flux leakage defect characterisation. NDT E Int 2007;40:179–84. doi:10.1016/j.ndteint.2006.08.002.

[21]   Chen Z, Preda G, Mihalache O, Miya K. Reconstruction of crack shapes from the MFLT signals by using a rapid forward solver and an optimization approach. IEEE Trans Magn 2002;38:1025–8.

[22]   Angani CS, Kim J, Le M, Lee J. Non-destructive testing of inclusions in cold-

rolled strip steels using hall and giant magnetoresistance sensor arrays. Int J Appl Electromagn Mech 2014;45:747–53. doi:10.3233/JAE-141902.

[23]   Altschuler E, Pignotti A. Nonlinear model of flaw detection in steel pipes by magnetic flux leakage. NDT E Int 1995;28:35–40. doi:10.1016/0963-8695(94)00003-3.

[24]   Beuker T, Palmer J, Quack M. In-line inspection using combined technologies–magnetic flux leakage and ultrasonic testing and their advantages. 4th Pipeline Technol. Conf., 2009, p. 1–6.

[25]   Dubov A. A Study of Metal Properties Using the Method of Magnetic Memory. Met Sci Heat Treat 1998;39:401–5.

[26]   Wang ZD, Yao K, Deng B, Ding KQ. Quantitative study of metal magnetic memory signal versus local stress concentration. NDT E Int 2010;43:513–8. doi:10.1016/j.ndteint.2010.05.007.

[27]   Lihong D, Binshi X, Shiyun D, Qunzhi C, Dan W. Variation of stress-induced magnetic signals during tensile testing of ferromagnetic steels. NDT E Int 2008;41:184–9. doi:10.1016/j.ndteint.2007.10.003.

[28]   Paik JK, Thayamballi AK. Ship-Shaped Offshore Installations. Cambridge: Cambridge University Press; 2007. doi:10.1017/CBO9780511546082.

[29]   Directive 2014/34/EU of the European Parliament and of the Council. Off J Eur Union 2014:309–56.

[30]   L'Hostis D, Kaminski ML, Aalberts PJ. Overview of the Monitas JIP. Proc. Offshore Technol. Conf., Houston, TX: 2010.

[31]   Kaminski ML, Aalberts PJ. Implementation of the Monitas system for FPSO units. Proc. Offshore Technol. Conf., Houston, TX: 2010.

[32]   L'Hostis D, Van der Cammen J, Hageman RB, Aalberts PJ. Overview of the Monitas II Project. Proc. Int. Offshore Polar Eng. Conf., Anchorage, Alaska: 2013.

[33]   Van der Meulen FH, Hageman RB. Fatigue Predictions using Statistical Inference within the Monitas II JIP. Proc. Int. Offshore Polar Eng. Conf., Anchorage, Alaska: 2013.

[34]   Tammer MD, Kaminski ML. Fatigue Oriented Risk Based Inspection and Structural Health Monitoring of FPSOs. Proc. Int. Offshore Polar Eng. Conf., Anchorage, Alaska: 2012.
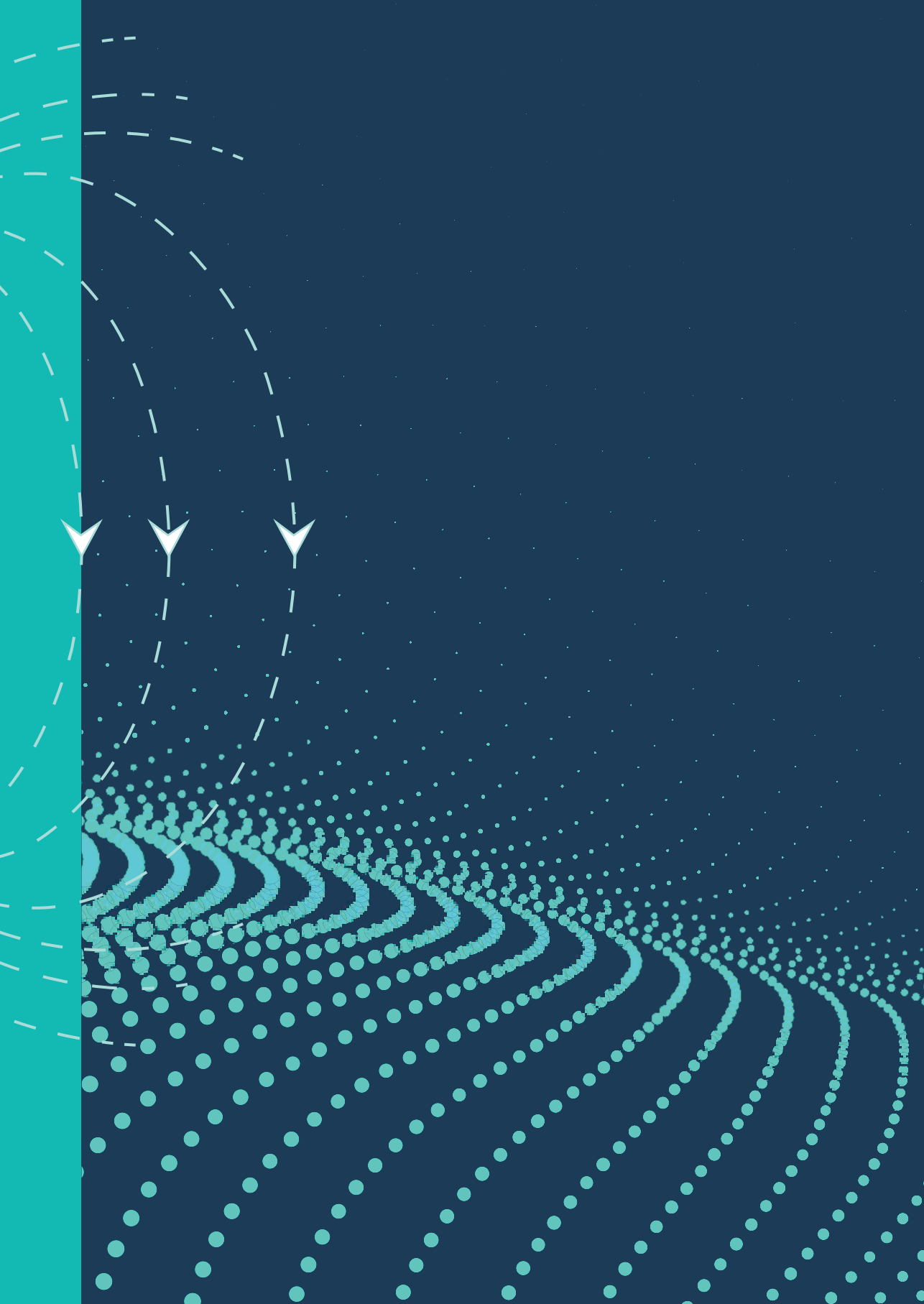
3

Slit Induced Self Magnetic Flux Leakage in a Square Steel Plate

Abstract

Marine structures have to be regularly inspected in order to confirm sufficient level of their structural integrity. A crack monitoring system can help keeping this level with less frequent inspections, because detected fatigue cracks need time to reach unacceptable sizes. The Self Magnetic Flux Leakage (SMFL) method is an attractive concept for a wireless monitoring system for detected cracks. Still, many knowledge gaps exist that prevent a successful application to marine structures. The goal of this chapter is to investigate different sources of magnetization and their effects on slit induced SMFL in a square steel plate. The slit in the steel plate represents a through thickness fatigue crack in a marine structure. The combined effects of Earth-induced and permanent magnetization were measured experimentally, whereas effects only induced by the Earth's magnetic field were determined numerically using the steel's magnetic properties defined in a separate experiment. The difference between the experimental and numerical SMFL was caused by permanent magnetization. The numerical simulation shows that the SMFL induced by the Earth's magnetic field is constant over the slit length. The SMFL induced by the permanent magnetization is one order of magnitude higher and varies linearly over the slit length for the investigated plate. The study concludes that it is feasible to develop a monitoring system for detected cracks in marine structures based on the SMFL.

Keywords

Marine structures; structural integrity; non-destructive evaluation; ferromagnetic steel; fatigue crack monitoring; self magnetic flux leakage; hall effect sensor.

3.1. Introduction

There are many possible ways to monitor a crack in a steel structure, but most of the available non-destructive evaluation (NDE) techniques are designed specifically for crack detection instead of monitoring. Extra requirements to be considered when applying an NDE method for crack monitoring are: wireless connectivity, low power consumption, robustness, safe for health and environment, and easy installation. Potential NDE methods (ultrasonic, radiographic, eddy current, and magnetic testing) have been reviewed in Chapter 2 and based on the aforementioned requirements, amongst other criteria, they have been ranked on their applicability for monitoring fatigue cracks in marine structures. The most promising are the magnetic techniques using the Self Magnetic Flux Leakage (SMFL) phenomenon [1], because the crack monitoring system can be fully passive. Magnetic sensors can be used in the vicinity of a crack to measure the SMFL, which is induced by the Earth's magnetic field and the permanent magnetization in the steel. By correct interpretation of the SMFL signal, the crack can be sized.

Even though the SMFL method shows great potential for wireless fatigue crack monitoring in marine structures, there are many challenges that come with the passive measurement technique. There are many uncertainties that need to be dealt with, e.g. material parameters [2,3], welding [4,5], crack opening and closing [6], effect of plastic deformation [7–9], and magnetization due to applied stress [10–13]. The SMFL method needs to be able to filter out all the magnetic variations due to these uncertainties and be left with the SMFL solely caused by crack growth or crack propagation. In order to filter out these variations, more knowledge needs to be gained about the interaction of different sources of magnetization with different materials, geometries, and defects. The aim of this chapter is to experimentally and numerically investigate the SMFL phenomenon for a steel plate with a slit that represents a through thickness fatigue crack, as a first step towards full understanding of this complex interaction.

3.2. Experimental Investigation

The most basic structural element found in marine structures that could require crack monitoring is a steel plate with a through thickness crack in the base material. For this most basic structural element, the SMFL phenomenon is first investigated by means of an experiment to see whether it can be passively measured, so without active magnetization, with an inexpensive and low-power magnetic sensor, such as a Hall effect sensor. To reduce the complexity, the crack is assumed to be a

straight slit of a constant width, which is a theoretical case. Also, the plate is unloaded so there is no stress magnetization and neither will the slit width vary in time. In reality, a crack will never be straight or have a constant width and will always be opening and closing in phase with the cyclic loading. If the crack does not open and close, it will not be growing or propagating, and monitoring would not be necessary.

3.2.1. Test Plate

In order to experimentally investigate the SMFL phenomenon, a square plate made out of FeE235 steel (typical for marine structures) that is 300 mm wide and 5 mm thick was wire eroded using electrical discharge machining (EDM) to create a slit representing a fatigue crack that is half the length of the plate and 0.3 mm wide, see Figure 3.1. The coordinate system is shown on the plate with its origin at the left bottom corner and the Z-axis pointing upwards (right-handed coordinate system).
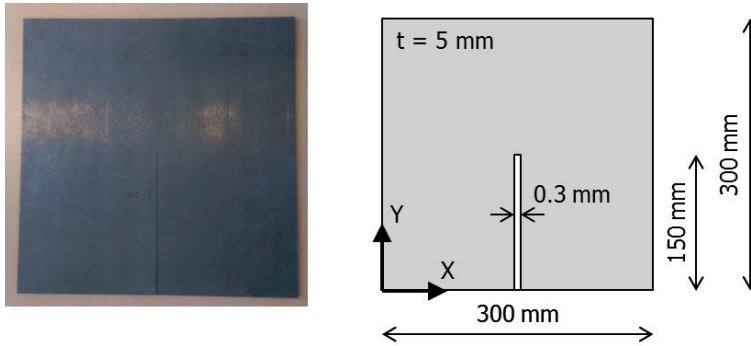

Figure 3.1: Test plate with a slit representing a through thickness fatigue crack.

3.2.2. Measurements

With a Tesla meter [14], a handheld single probe Hall effect sensor, the out-of-plane magnetic flux density was measured along a number of lines perpendicular to the slit and with a constant altitude of 3 mm above the plate surface, which is a realistic altitude to place a sensor at. The plate was positioned horizontally and its X-axis was parallel to the horizontal component of the Earth's magnetic field. Figure 3.2 shows the magnetic flux density measurements along the two lines that were above the slit and the line right above the slit tip. As can be seen, these measurements show a low signal to noise ratio. The observed noise level from these measurements is approximately 10 μT. Still, the red and blue lines show a gradually increasing signal. This is as expected when considering that the background field, the Earth's magnetic field, has a component in the negative Z-direction (downwards) and a component in the positive X-direction (left to right):

$$B_{BG} = \left[B_{BG,X} \; ; \; B_{BG,Y} \; ; \; B_{BG,Z} \right] = [15 \; ; 0 \; ; \; -30] \, \mu T.$$

The Z-component of the background field is visible in the measurements as a vertical offset, so the average magnetic flux density over the length of the plate is -30 µT. The X-component of the background field causes the gradual increase, so a positive slope, in the measurements with on the left side flux entering the steel plate, and on the right side flux exiting the steel plate. The black line right above the slit tip does not show this gradually increasing signal, which is most likely due to the presence of the slit. However, there is no local disturbance visible near the slit tip. This is because the noise in the measurements is larger than the disturbance near the slit tip as will be concluded from the numerical study in the next section.
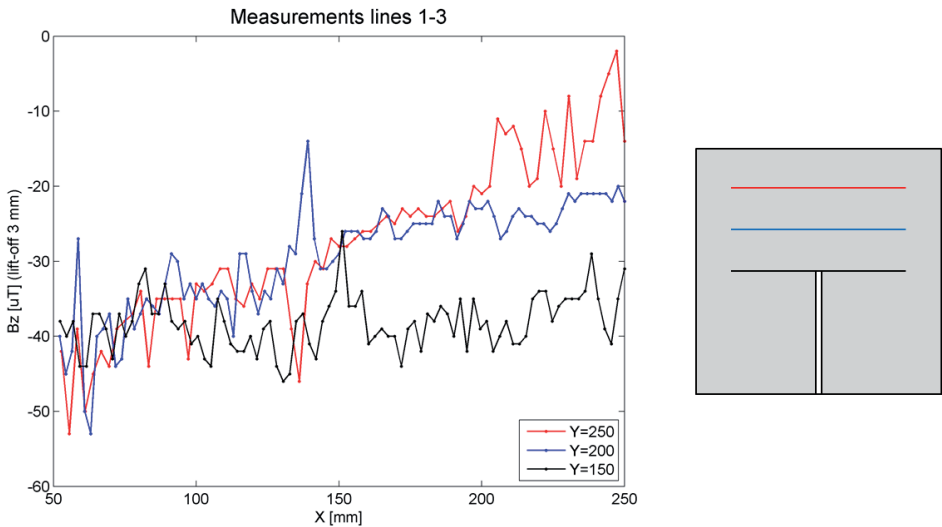

Figure 3.2: Measurement results for B_Z along lines 1-3 (part without slit).

The same measurement procedure was done along the lines that are distributed over the slit, see Figure 3.3. The further away from the slit tip, the larger the disturbance near the slit becomes. Even though the specimen is not actively magnetized, these measurements show very similar results with what is found in literature on MFL testing [15], with a positive peak on one side of the slit and a negative peak on the other side. The only difference is that the measurements in Figure 3.3 show an offset of approximately -30 µT, which is due to the Z-component of the background field. Another observation when looking at the peaks near the slit is that the peak-to-peak value, the signal strength, increases with increasing distance from the slit tip. Lastly, it can be seen that a magnetic sensor with microTesla sensitivity can easily detect the artificial slit at 25 mm or further away from the slit tip

without introducing any external magnetic field other than that of the Earth. In order to detect the location of the slit tip with higher accuracy, the noise would need to be reduced significantly or the distance between the sensor and the plate surface, the altitude, needs to be reduced.
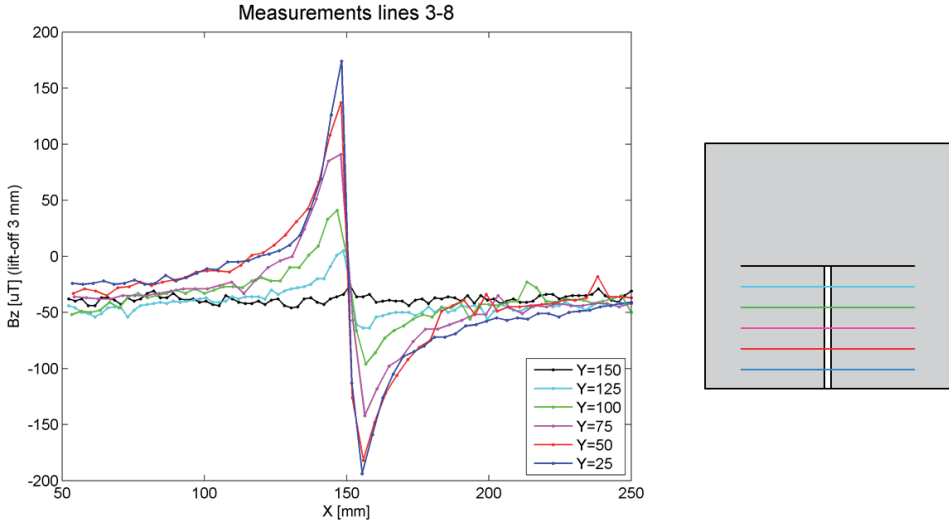

Figure 3.3: Measurement results for B_Z along lines 3-8 (part with slit).

The magnetization due to the background field is not the only source of magnetization. In general, there is also a slowly varying permanent magnetization present in the material, which depends on the history of the specimen and is independent of the current environment. The permanent magnetization is usually unknown, very difficult to measure, and is generally non-uniform, which is a major challenge for interpreting SMFL measurements. It means that the experiment can give a different result for a plate that is identical to the one tested here. In fact, it can even give different results when doing the same measurements for this very same plate at a later moment in time.

So, the combined effect of different sources of magnetization on the slit induced SMFL was measured experimentally. In the following section, the SMFL induced by the Earth's magnetic field is determined numerically using the magnetic properties of steel defined in a separate experiment. As a result, the difference between the experimental and numerical SMFL will be due to the permanent magnetization.

3.3. Numerical Investigation

Electromagnetic fields are governed by Maxwell's equations, which are partial differential equations. In magneto-statics, which disregards time-varying electric fields, these equations reduce to the following equation:

$$\nabla \times \vec{H} = \vec{J}, \tag{3.1}$$

where $\vec{H}$ is the magnetic field strength and $\vec{J}$ the electrical current density.

Gauss' law for magnetism, which states that there are no magnetic charges, yields the following equation:

$$\nabla \cdot \vec{B} = 0, \tag{3.2}$$

where $\vec{B}$ is the magnetic flux density.

The relation between the magnetic flux density and the magnetic field strength is described with the following constitutive equation:

$$\vec{B} = \mu_0(\vec{H} + \vec{M}) = \mu_0 \cdot \mu_r \cdot \vec{H} + \mu_0 \cdot \overrightarrow{M_p}, \tag{3.3}$$

where μ_0 is the magnetic permeability of a vacuum, μ_r the relative magnetic permeability, $\vec{M}$ the total magnetization, and $\overrightarrow{M_p}$ the permanent magnetization.

For a rectangular steel plate in a background field, equations 3.1 to 3.3 can be solved analytically, assuming that the plate is isotropic, uniformly magnetized, and very thin [16]. These assumptions are not valid for a geometry with a slit, so equations 3.1 to 3.3 need to be solved numerically. A suitable numerical method for this problem is the Finite Element Method (FEM), first applied for magnetic flux leakage calculations by Hwang & Lord [17], because it discretizes the solution domain, which allows for local mesh refinement near the defect. In this section, the SMFL phenomenon induced by the Earth magnetic field is investigated by numerical simulation of the steel plate from Figure 3.1 using FEM.

3.3.1. Magnetic Material Parameters

In order to solve equations 3.1 to 3.3, whether analytically or using FEM, the material parameters μ_r and $\overrightarrow{M_p}$ need to be determined. Both parameters are difficult to choose, since steel shows hysteretic behavior. It means that the parameters are dependent on the specimen's history, and they can be both anisotropic and

inhomogeneous, since every infinitesimal part of the steel plate can have a different hysteresis curve in all three directions.

To determine μ_r and $\overrightarrow{M_p}$, the magnetic dipole moments have been measured under a varying background field for two samples taken from the same batch of steel as the plate from Figure 3.1, using a Quantum Design MPMS-5S SQUID magnetometer. The samples were taken from the steel using micro EDM and are in the shape of an ellipsoid of 5 mm long and 1 mm in diameter, see Figure 3.4. One sample has its longitudinal axis in the X-direction of the steel plate from Figure 3.1, and the other sample in the Y-direction, to account for possible anisotropy. The measured magnetic dipole moments for both samples can be seen in Figure 3.5 where the background field was ranging from zero to 100 Gauss ($1\ G = 10^3/4\pi\ A/m$), then to -100 Gauss and back to zero again, with a step size of 5 Gauss. Since all fields are in the longitudinal direction of the sample, the problem at hand is a scalar problem.
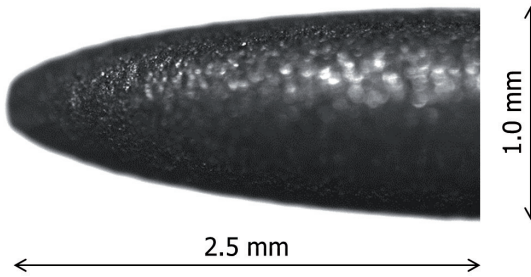

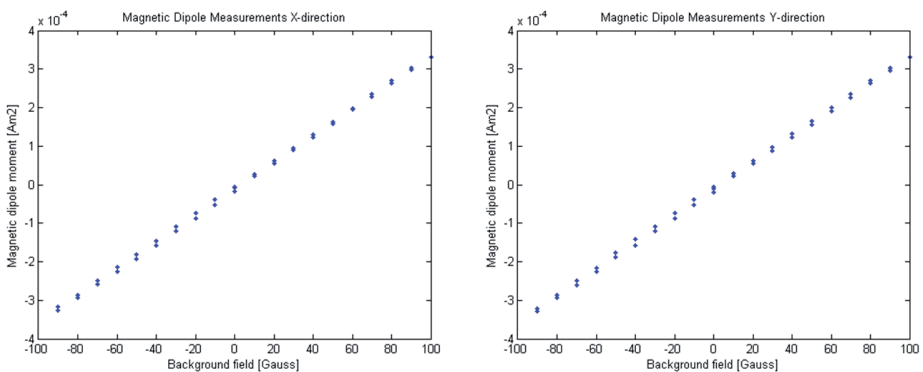Figure 3.4: Symmetric half of ellipsoid steel sample.

Figure 3.5: Results of magnetic dipole moment measurements with Quantum Design MPMS-5S SQUID.

The reason why the samples are chosen to have an ellipsoid (prolate spheroidal) shape is that when brought into a uniform applied field H_0, the magnetic field strength H and magnetization M are uniform throughout [18]. The magnetization inside the steel sample can be found by dividing the magnetic dipole moment by the volume of the sample. With the magnetization and the background field known, the magnetic field strength inside the steel sample can be calculated as

$$H_i = H_0 - N_X \cdot M, \tag{3.4}$$

where H_i is the magnetic field strength inside the ellipsoid, H_0 the background field, M the magnetization inside the ellipsoid, and N_X the demagnetization factor in the longitudinal direction [18].

The demagnetizing factor is determined by the ratio of the axes of the ellipsoid. The general ellipsoid has three semi-axes, where $a \geq b \geq c \geq 0$. For a prolate spheroid ($b = c$), the demagnetizing factor is given [18] by

$$N_X = \frac{1}{m^2-1}\left[\frac{m}{2\sqrt{m^2-1}} \cdot ln\left(\frac{m+\sqrt{m^2-1}}{m-\sqrt{m^2-1}}\right) - 1\right], \tag{3.5}$$

where $m = a/c$.

The steel samples used in this study have a value for $m = 5$, see Figure 3.4, which results in a demagnetizing factor of $N_X = 0.0558$. For each measurement point in Figure 3.5, which shows the measured magnetic dipole moments, the magnetic field strength and the magnetization inside the ellipsoid sample can now be derived. Figure 3.6 shows the resulting magnetization curves for both samples and their linear regressions.
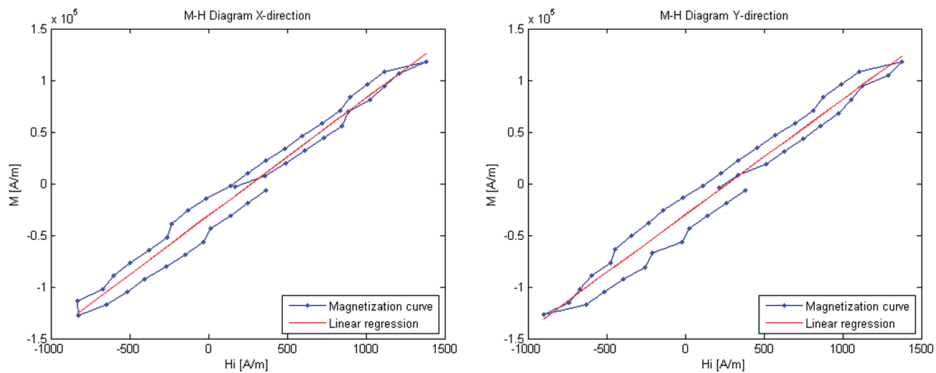

Figure 3.6: Magnetization curves with linear regression.

Even though the maximum magnetization is only approximately 10 percent of the saturation magnetization of low carbon steel, some hysteresis can be observed. It is clear that there is an initial magnetization curve, which is followed by a hysteresis loop. Nevertheless, the hysteretic effect is sufficiently small to be neglected, especially when considering that the Earth's magnetic field, approximately 40 A/m, is much weaker that the fields applied here. This means that the magnetization curve can be assumed to be linear, which is why the linear regression is shown in Figure 3.6 as well. The magnetic susceptibility χ is defined as the slope of the magnetization curve, so

$$\chi = \frac{M}{H_i}. \tag{3.6}$$

The relative permeability μ_r can be simply derived from the magnetic susceptibility by

$$\mu_r = \chi + 1. \tag{3.7}$$

The resulting relative permeabilties are 115 for the sample in X-direction and 113 for the sample in Y-direction. To simplify, the relative permeability of the steel plate is assumed to be 115 in all directions and uniform throughout the plate.

As for the permanent magnetization, both linear regression curves show a magnetization of approximately -30 kA/m for $H_i = 0$. This would mean that the permanent magnetization of the steel plate is 30 kA/m in both negative X and negative Y-direction. However, the permanent magnetization is likely to be very non-uniform throughout the plate. Therefore, the best first approximation is to assume the permanent magnetization to be zero in the entire volume of the steel plate and use FEM to quantify the effect of induced magnetization only.

3.3.2. Finite Element Analysis

The steel plate from Figure 3.1 was modeled. The software package ANSYS Maxwell, which applies an adaptive meshing technique [19], was used to do the FEM simulation. The model was meshed using tetrahedral linear elements and the same background field was applied as was measured in the experiment. Local mesh refinement was applied around the slit, see Figure 3.7, to obtain faster convergence to a solution with a maximum error of 0.1 percent. Since only weak fields are being considered, hysteresis effects were disregarded and the plate material was modeled linearly with a uniform relative permeability of 115 in all three directions and without any permanent magnetization.
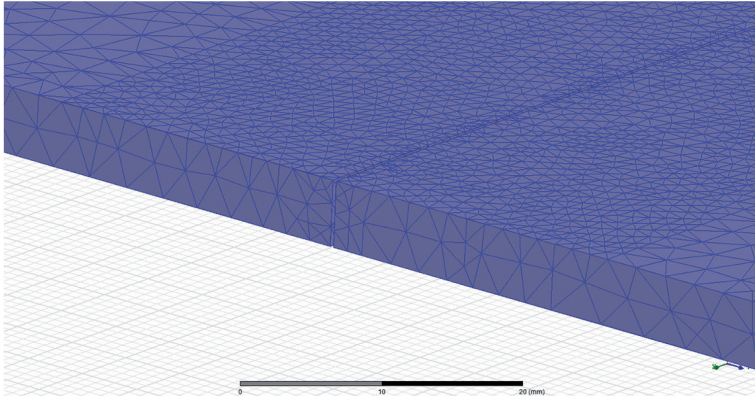
Figure 3.7: Local mesh refinement near the slit.

After solving the model using the magneto-static solver, the overall results are plotted in a surface plot that shows the magnitude of the magnetic flux density at the plate surface (still in the steel), see Figure 3.8. The magnetic flux density reaches a maximum at the slit tip, which can be explained by the fact that the magnetic flux feels the resistance of the slit and, for that reason, bypasses the slit by going around the slit tip. More interesting is to look at the out-of-plane component of the magnetic flux density as it is this component that resembles the magnetic flux leakage. In Figure 3.9, where the Z-component of the magnetic flux density is plotted at the plate surface, it can be seen that there is a disturbance near the entire length of the slit in the form of a positive peak on one side of the slit and a negative peak on the other.
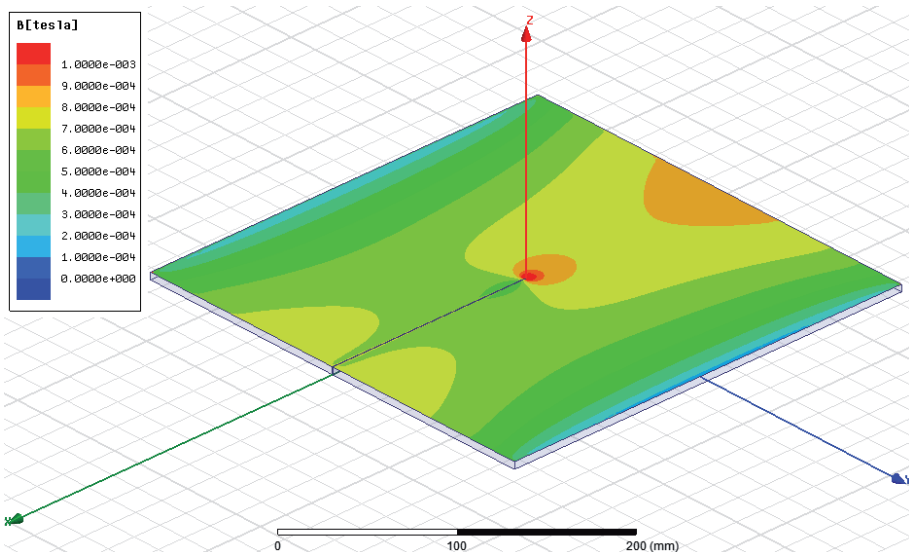

Figure 3.8: Magnitude of magnetic flux density B at the plate surface.
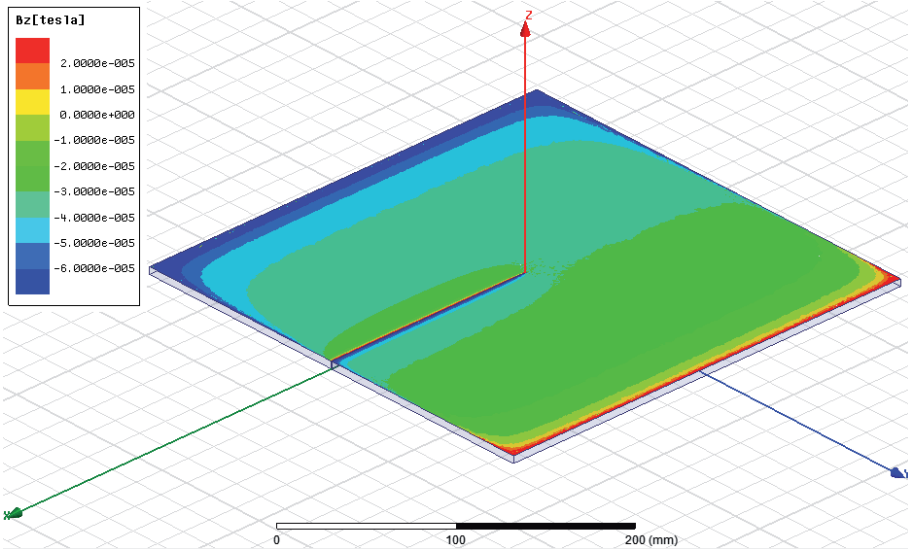
Figure 3.9: Magnetic flux density in Z-direction B_Z at the plate surface.

The magnetic flux leakage around the slit can more clearly be observed when plotting the out-of-plane magnetic flux density B_Z along the same lines as where the measurements from the previous section were taken. Figure 3.10 shows the out-of-plane magnetic flux density along the lines above the part of the plate without slit and Figure 3.11 shows B_Z along the lines above the part of the plate with slit.
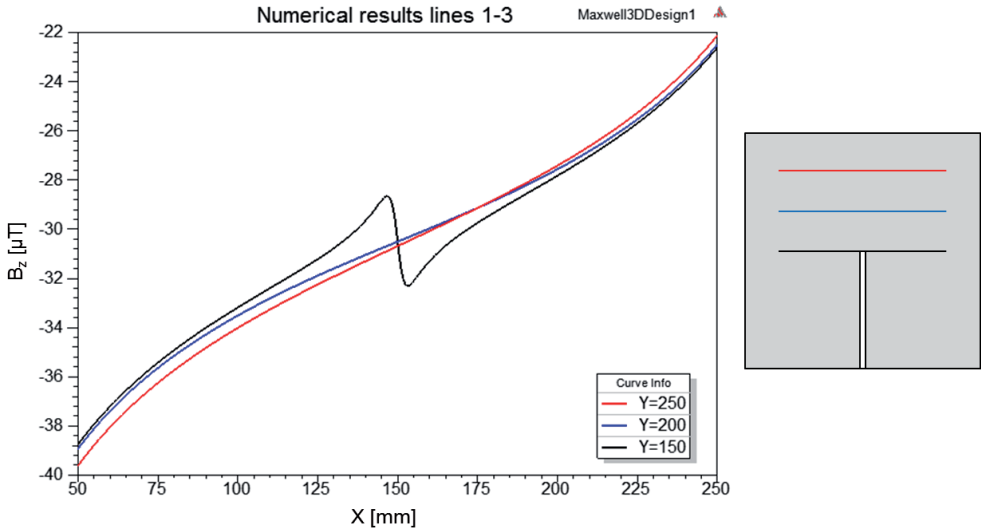

Figure 3.10: FE results for B_Z along lines 1-3 (part without slit).
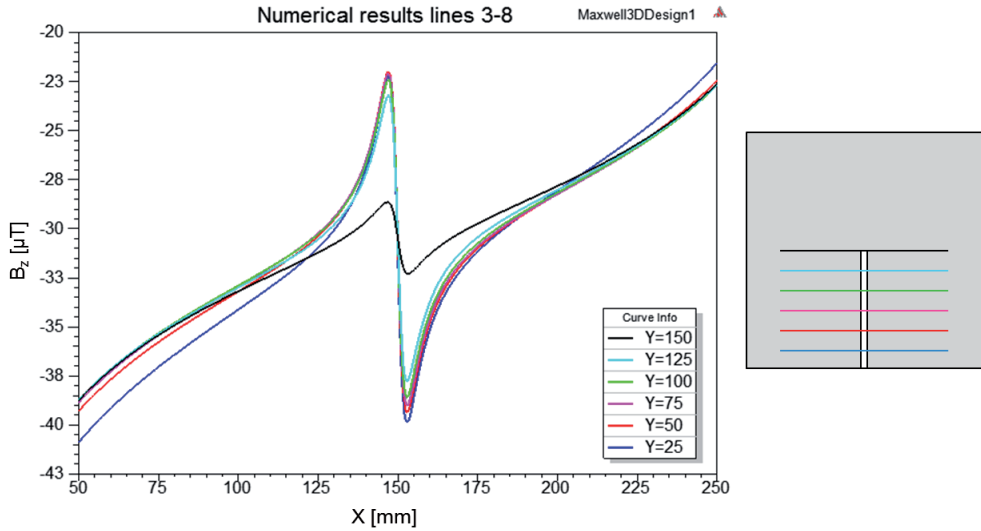
Figure 3.11: FEM results for B_Z along lines 3-8 (part with slit).

At first glance, the numerical results look very similar to the measurements. Interestingly, along the black line, right above the slit tip, a disturbance can now be seen in the B_Z. Its peak-to-peak value is approximately 5 µT, which explains why it could not be seen from the measurements because the noise level is approximately 10 µT. The largest difference with the measurements is the magnitude of the peak-to-peak values, which are much smaller. This can be explained by the fact that in the numerical model only the induced magnetization has been taken into account, where in reality there is also a permanent magnetization present in the material. This permanent magnetization, which may be inhomogeneous over the plate, has not been modeled because it is only known at one location.

3.4. Discussion

When looking at the peak-to-peak values plotted against the distance from the slit tip in Figure 3.12, the difference between the measurements and the numerical results becomes very clear. As previously mentioned, the numerical results only account for the induced magnetization caused by the Earth's magnetic field. The measurements account for both the induced and permanent magnetization, so the difference between the two is caused by the permanent magnetization in the plate only. It is interesting to see that the permanent part is much larger with respect to the induced part, which indicates that crack monitoring based on the SMFL phenomenon should even be working when there is no background field present.
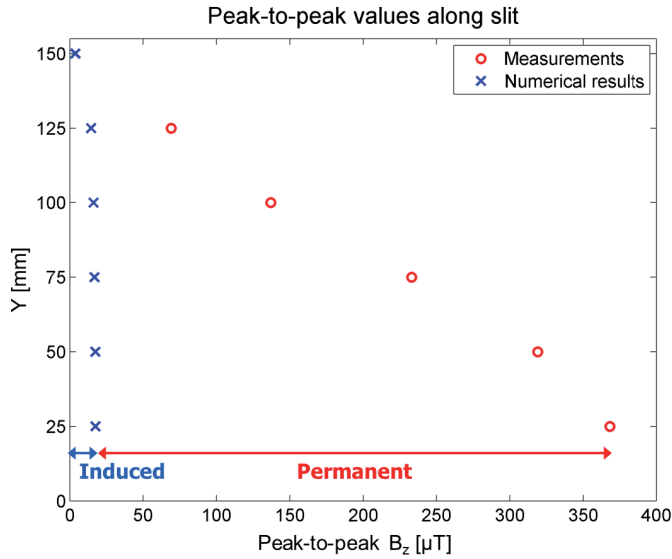
Figure 3.12: Peak-to-peak values of B_Z along the slit (induced and permanent magnetization).

Another observation is that the measured peak-to-peak values show a linear relation with respect to the distance from the slit tip, if one considers that the last point is influenced by the fact that it lies in close proximity to the plate's edge. This result corresponds with earlier findings by Lihong *et al.* [20]. If the signal strength of the SMFL is truly linearly dependent on the crack length, then it means that, theoretically, one could make a prediction of the crack length based on only two measured peak-to-peak values somewhere along the crack.

Lihong *et al.* argue that this linear relation between signal strength and crack length is due to stress magnetization, so magnetization due to mechanical stress in the material [20,21]. The experimental results shown in this chapter show otherwise because there was no mechanical loading involved, yet the same linear relation was found. The results presented in this chapter suggest that the linear relation between signal strength and distance from the slit tip is due to the permanent magnetization.

It should be noted that one set of experimental measurements and numerical simulation of one test specimen gives not enough evidence to state that the SMFL in a steel plate with a slit in a weak magnetic field is linearly dependent on the distance from the slit tip. Therefore, more experiments should be done on the same test specimen to investigate time dependency of the results and more specimens should be tested to reduce the uncertainty in the measurement results.

For this study, the magnetic properties of the steel test plate were determined by measuring the magnetization curves of ellipsoid samples from the base material. Even though the magnetization curves of both samples are almost identical, it does not mean that the magnetic properties are uniform over the plate. Also, it was assumed that fabrication of the ellipsoid samples using micro EDM had no influence on their magnetic properties and that their shapes were perfect prolate spheroids. Both assumptions result in errors that are difficult to quantify. Therefore, alternative methods need to be investigated to obtain a better estimate of the magnetic properties of a test specimen.

3.5. Conclusions

Experimental investigation of the Self Magnetic Flux Leakage (SMFL) of a square steel plate with a slit representing a through thickness fatigue crack has shown that the signal strength is large enough to be measured with a Hall effect sensor, which is currently inexpensive and small in size. In the experiment, two sources were responsible for the SMFL: the induced magnetization by the Earth's magnetic field and the permanent magnetization in the steel. The magnetic flux leakage due to the induced magnetization was modeled with a finite element model. The numerical results showed that the induced part for this particular plate is relatively small compared to the permanent part. This indicates that crack monitoring based on the SMFL phenomenon is not very sensitive to changes in the background field and should even be working when there is no background field present. Also, the induced part of the SMFL showed nearly constant peak-to-peak values along the slit, whereas the measurements showed a linear relation between peak-to-peak values and distance from the slit tip. This suggests that the linear relation is caused by the permanent magnetization. More research is necessary to investigate whether this linear relation is always present for steel plates with a through thickness slit in a weak magnetic field.

3.6. References

[1]   Dubov A. A Study of Metal Properties Using the Method of Magnetic Memory. Met Sci Heat Treat 1998;39:401–5.

[2]   Jiles DC, Atherton DL. Theory of ferromagnetic hysteresis (invited). J Appl Phys 1984;55:2115–20. doi:10.1063/1.333582.

[3]   Pasquale M, Bertotti G, Jiles DC, Bi Y. Application of the Preisach and Jiles–Atherton models to the simulation of hysteresis in soft magnetic alloys. J Appl Phys 1999;85:4373. doi:10.1063/1.369788.

[4]   Luming L, Songling H, Xiaofeng W, Keren S, Su W. Magnetic field abnormality caused by welding residual stress. J Magn Magn Mater 2003;261:385–91. doi:10.1016/S0304-8853(02)01488-9.

[5]   Roskosz M. Metal magnetic memory testing of welded joints of ferritic and austenitic steels. NDT E Int 2011;44:305–10. doi:10.1016/j.ndteint.2011.01.008.

[6]   Clark R, Dover WD, Bond LJ. The effect of crack closure on the reliability of NDT predictions of crack size. NDT Int 1987;20:269–75. doi:10.1016/0308-9126(87)90444-5.

[7]   Makar JM, Tanner BK. Effect of plastic deformation and residual stress on the permeability and magnetostriction of steels. J Magn Magn Mater 2000;222:291–304. doi:10.1016/S0304-8853(00)00558-8.

[8]   Kida K, Ishida M, Furuse M, Mizobe K, Santos EC. Effect of plastic deformation on magnetic fields around fatigue crack tips of carbon tool steel (JIS, SKS93). Int J Fatigue 2016;88:156–65. doi:10.1016/j.ijfatigue.2016.03.022.

[9]   Wang ZD, Deng B, Yao K. Physical model of plastic deformation on magnetization in ferromagnetic materials. J Appl Phys 2011;109. doi:10.1063/1.3574923.

[10]   Bozorth RM, Williams HJ. Effect of Small Stresses on Magnetic Properties. Rev Mod Phys 1945;17:72–80.

[11]   Craik DJ, Wood MJ. Magnetization changes induced by stress in a constant applied field. J Phys D Appl Phys 1970;3:1009–16. doi:10.1088/0022-3727/3/7/303.

[12]   Misra A, Varshney BG. Can a stress alone applied to a demagnetized ferromagnetic specimen produce any magnetization? J Magn Magn Mater 1990;89:159–66.

[13]   Wang ZD, Yao K, Deng B, Ding KQ. Quantitative study of metal magnetic memory signal versus local stress concentration. NDT E Int 2010;43:513–8. doi:10.1016/j.ndteint.2010.05.007.

[14]   Wuntronic. Wuntronic Tesla Meter KOSHAVA-USB n.d. http://www.wuntronic.de/en/USB-Tesla-Meter-Gauss-Meter-with-USB.html (accessed March 27, 2018).

[15]   Van der Horst MP, Kaminski ML, Puik E. Methods for Sensing and Monitoring Fatigue Cracks and Their Applicability for Marine Structures. Proc. Int. Offshore Polar Eng. Conf., Anchorage, Alaska: 2013, p. 455–62.

3

[16]   Van der Horst MP, Kaminski ML, Lepelaars E. Testing and Numerical Simulation of Magnetic Fields Affected by Presence of Fatigue Cracks. Proc. Int. Offshore Polar Eng. Conf., Anchorage, Alaska: International Society of Offshore and Polar Engineers; 2014, p. 445–50.

[17]   H. Hwang J, Lord W. Finite Element Modeling of Magnetic Field/Defect Interactions. ASTM J Test Eval 1975;3:21–5.

[18]   Osborn JA. Demagnetizing Factors of the General Ellipsoid. Phys Rev 1945;67:351–7. doi:10.1103/PhysRev.67.351.

[19]   ANSYS Maxwell V16 Training Manual 2013:Lecture 6: Meshing and Mesh Operations. http://ansoft-maxwell.narod.ru/en/Maxwell_v16_L06_Mesh_Operations.pdf (accessed March 6, 2017).

[20]   Dong L, Xu B, Dong S, Chen Q, Dan W. Monitoring fatigue crack propagation of ferromagnetic materials with spontaneous abnormal magnetic signals. Int J Fatigue 2008;30:1599–605. doi:10.1016/j.ijfatigue.2007.11.009.

[21]   Dong LH, Xu B, Dong S, Song L, Chen Q, Wang D. Stress dependence of the spontaneous stray field signals of ferromagnetic steel. NDT E Int 2009;42:323–7. doi:10.1016/j.ndteint.2008.12.005.

4

Magnetic Properties of Structural Steels for Simulation of Crack Monitoring by Finite Element Method

This chapter is based on:

Abstract

The Metal Magnetic Memory method is a novel technique for monitoring fatigue cracks in steel structures, which can reduce operational expenses and increase safety by minimizing inspections. The crack geometry can be identified by measuring the Self Magnetic Flux Leakage (SMFL), which is induced by the Earth's magnetic field and the permanent magnetization. The Finite Element Method can be used to simulate the induced magnetic field around cracks to help interpret the SMFL measurements but it is unclear what material properties to use. This chapter aims to determine the magnetic permeability of structural steel for accurate simulation of the induced magnetic field around cracks by the Finite Element Method. The induced magnetic field was extracted from measurements above two square steel plates, one without defect and one with a straight slit, and compared with finite element results in function of the relative permeability. For both plates, a uniform relative permeability could be found for which experimental and numerical results were in good agreement. For the plate without defect and a relative permeability of 350, errors were within 20% and were concentrated around the plate's edges. For the plate with the slit and a relative permeability of 225, errors were within 5%.

Keywords

Crack monitoring; metal magnetic memory; self magnetic flux leakage; finite element method; magnetic permeability; permanent magnetization.

4.1. Introduction

The applicability of several non-destructive evaluation (NDE) methods on a crack monitoring system for marine structures was reviewed in Chapter 1. The most promising is the Metal Magnetic Memory (MMM) method, which is an advanced NDE method that can be used to detect or monitor flaws, such as cracks, in ferromagnetic materials [1–4]. This method is very similar to Magnetic Flux Leakage (MFL) testing but does not require active magnetization of the specimen. Instead, the MMM method measures the Self Magnetic Flux Leakage (SMFL), which is induced only by the Earth's magnetic field and a permanent magnetization that is caused by the material's hysteresis property [5]. Developing an understanding of both the induced and permanent magnetic fields around a crack is necessary to interpret the SMFL measurements and determine the crack's geometry reliably. The permanent magnetization of a steel structure varies slowly in time and is affected by remanence [6], stresses [7–10], and temperature fluctuations [11,12]. The induced magnetization can vary instantaneously and is influenced by the structure's geometry, the background field and the steel's magnetic permeability.

The Earth-induced magnetic field distribution around ferromagnetic structures with complex boundary geometries, such as a steel plate with a fatigue crack, can be simulated numerically by the Finite Element Method (FEM). The accuracy of FEM has been demonstrated in [13] by comparing simulation results of a thin ferromagnetic plate in a uniform background field with its analytical approximation. Hwang & Lord were the first to use FEM to model the interaction between the magnetic field and a defect, which they demonstrated for a circular ferromagnetic bar with a rectangular surface defect [14]. Currently, there are several commercial FEM software packages available (e.g. ANSYS Maxwell and COMSOL Multiphysics) to simulate the interaction between magnetic fields and a wide variety of defect shapes, sizes, and locations likely to be seen in practice.

The aim of this chapter is to determine the magnetic permeability of structural steels for accurate simulation of the induced magnetic field distribution around cracks using FEM. Steel's magnetic properties depend greatly on the microstructure (e.g. grain size, pearlite fraction, carbon content, manganese content) [15,16], and are generally described by the hysteresis curve, which is the nonlinear relationship between the magnetic field strength and the magnetic flux density (*B-H* curve). However, for weak fields such as the Earth's magnetic field, the *B-H* curve can be assumed linear, see Figure 4.1. The slope of the curve is the magnetic permeability resulting in the induced magnetization and a vertical offset can be caused by the permanent magnetization. Note that every grain or magnetic domain of the steel's

microstructure can have a different *B-H* curve that may even be different in the X, Y, and Z directions.
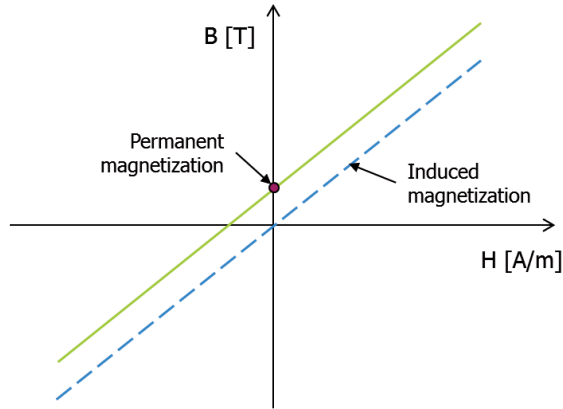

Figure 4.1: Linear approximation of the hysteresis curve, after [13].

To determine the magnetic permeability of a steel plate, induced magnetic field measurements are compared to Finite Element (FE) results for a number of values for the relative permeability. This way, the global permeability of an entire plate can be determined, unlike in Chapter 3 where the permeability was determined of a small ellipsoid sample. The induced magnetic field is separated from the permanent magnetic field using two different methods. For a fully symmetric plate, the permanent magnetic field can be filtered out by repeating the measurements with the plate rotated 180 degrees. This is done in Experiment 1 for a square steel plate without defect. For an object of any other geometry, the permanent magnetic field can be filtered out by repeating the measurements in zero magnetic field by using a magnetic field simulator, which has been done in the past by researchers focusing on reducing the magnetic signature of naval ships [17,18]. This is done in Experiment 2 for a square steel plate with a slit. The methods of both experiments, including their FE models, are explained in section 4.2. The results are presented in section 4.3 and discussed in section 4.4. Finally, some conclusions are drawn.

4.2. Method

Two experiments were conducted. In the first experiment, magnetic measurements were taken above a steel plate without any defect while in the Earth's magnetic field. By extracting the induced magnetic field from the measurements and comparing it with a linear magneto-static FE model of the same plate, the average

magnetic permeability of the plate could be determined. In the second experiment, the steel plate from Chapter 3 with a straight slit was held in a magnetic field simulator while taking magnetic measurements above the slit. Again, the induced magnetic field was extracted from the measurements to be compared with FE results in order to find the magnetic permeability of the plate. Both experiments and their FE models are described in more detail in the subsections below.

4.2.1. Experiment 1

A square FeE235 steel plate of 300 mm wide and 5 mm thick is placed underneath a 3-axis fluxgate magnetometer with nanoTesla sensitivity that can be moved in space in a controlled way, see Figure 4.2. The sensor is programmed to take measurements on a grid of 121 points 75 mm above the plate surface, see Figure 4.3, which is the closest distance this test setup allows. At every grid point, the sensor takes 10 measurements in exactly one second, which are then averaged. The grid columns are numbered from $i = -5$ to $i = 5$ and the rows are numbered from $j = -5$ to $j = 5$. The measurements are repeated with the plate rotated 180 degrees around the Z-axis to be able to filter out the permanent magnetic field. The same setup is also used to measure the background field while the plate is removed.
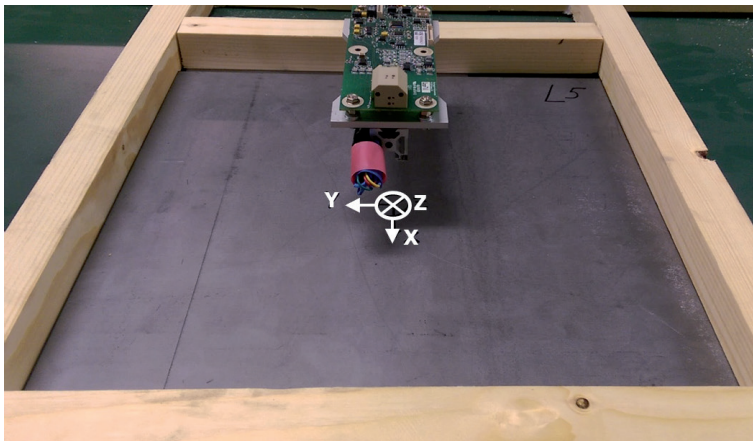

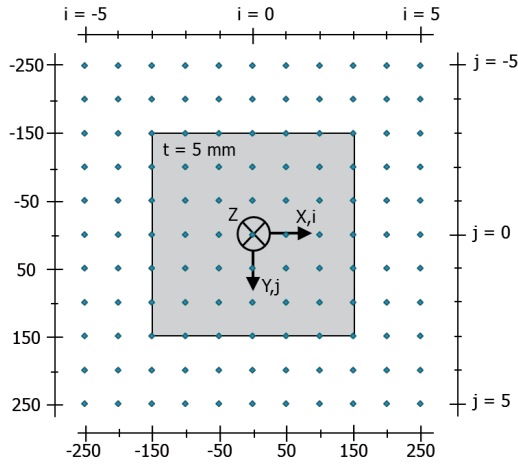Figure 4.2: Experimental setup Experiment 1.

Figure 4.3: Test plate Experiment 1 with measurement grid.

4.2.2. FE Model 1

Experiment 1 is simulated by a linear magneto-static FE model using ANSYS Maxwell. The steel plate is assumed to have no permanent magnetization, so its magnetization is dependant only on the relative permeability μ_r, the background field B_{BG}, and the plate's geometry. The geometry of the plate is known and the background field has been measured using the test setup of Experiment 1 without a steel plate. The measured background field can be seen in Figure 4.4. Note that the dashed square shows the location where the plate will be placed for the actual measurements. The measured background field is fairly uniform, so a uniform background field is assumed in the FE model as the average measured background field:

$$B_{BG} = \left[B_{BG,X} \, ; \, B_{BG,Y} \, ; \, B_{BG,Z}\right] = [-14.3 \, ; -5.6 \, ; \, 36.3] \, \mu T.$$

The model is meshed using linear tetrahedral elements with a minimum of 2 elements over the thickness of the plate. The background field is applied as boundary conditions on the outer surfaces of the model domain, which is a cube ten times the size of the plate. The domain is modeled as a vacuum, so $\mu_r = 1$, which is a good approximation of the permeability of air. The relative permeability of the steel plate is set as a parameter that varies between 50 and 500 with steps of 50. A 3D representation of the FE model with the applied background field as a vector plot can be seen in Figure 4.5.
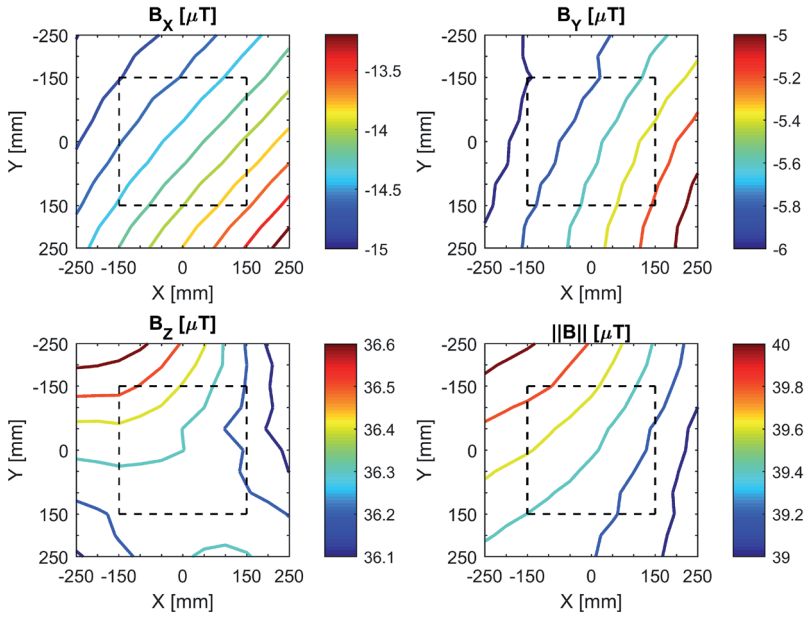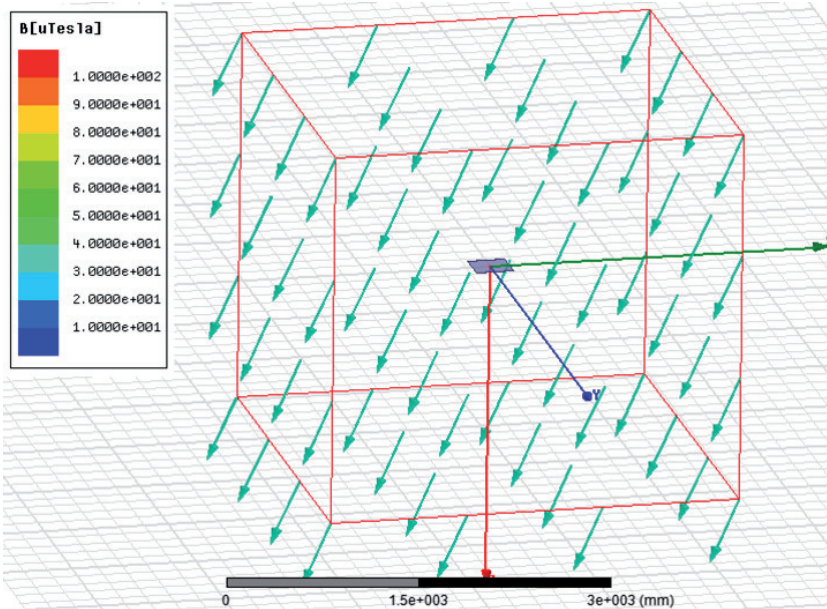
Figure 4.4: Measured background field.

Figure 4.5: FE model 1 with background field.

4.2.3. Experiment 2

A square FeE235 steel plate of 300 mm wide, 5 mm thick, and with a wire cut slit of 150 mm long and 0.3 mm wide, see Figure 4.6, is put in a magnetic field simulator with Helmholtz coils in all three directions. One 3-axis fluxgate magnetometer with nanoTesla sensitivity and a sampling rate of 1000 Hz is used to measure the magnetic field above the plate while a second magnetometer measures the background field, as depicted in Figure 4.7. An acrylic glass (polymethyl methacrylate) plate with a grid of holes is placed over the steel plate in order to fix the location of the sensor above the plate with pins.
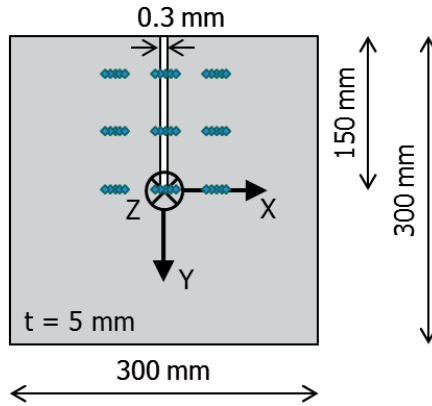
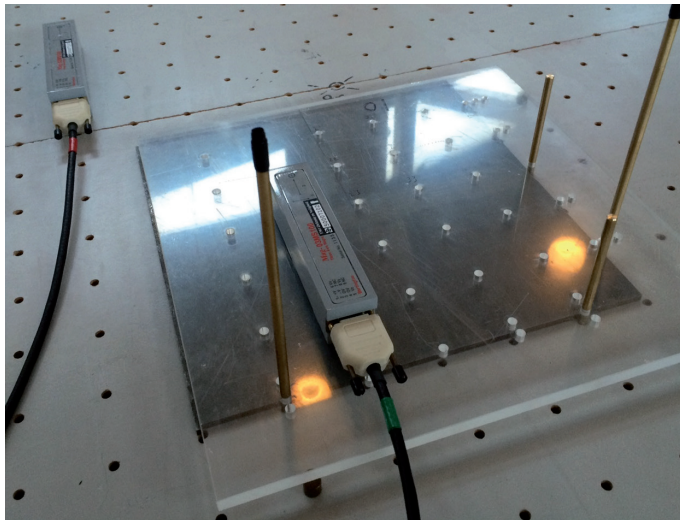Figure 4.6: Test plate Experiment 2 with measurement grid.

Figure 4.7: Test setup Experiment 2.

Magnetic measurements are taken in 9 clusters of 5 points near the slit, each 30 mm above the steel plate, see Figure 4.6. Note that the measurement grid shown in Figure 4.6 depicts the approximate sensor locations and that the pickup coils for X, Y and Z are spaced 15 mm from each other within the fluxgate magnetometer.

The first set of measurements is taken with a background field of 50 μT (average Earth's magnetic field strength) in positive X-direction to maximize the flux leakage around the slit. The second set of measurements is taken with zero background field by active shielding to determine the permanent magnetic field around the plate.

4.2.4. FE Model 2

Experiment 2 is also simulated by a linear magneto-static FE model using ANSYS Maxwell. Again, the steel plate is assumed to have no permanent magnetization, so its magnetization is dependent only on the relative permeability μ_r, the background field B_{BG}, and the plate's geometry. The geometry of the plate is known, see Figure 4.6. The background field is controlled in the experiment using a magnetic field simulator and is set on 50 μT in positive X-direction. The same uniform background field is applied in the FE model:

$$B_{BG} = \left[B_{BG,X} \; ; \; B_{BG,Y} \; ; \; B_{BG,Z}\right] = [50 \; ; 0 \; ; \; 0] \, \mu T.$$

The model is meshed using linear tetrahedral elements with a minimum of 2 elements over the thickness of the plate and with local mesh refinement around the slit, see Figure 4.8, and around the measurement grid, so 30 mm above the plate surface.

The background field is applied as boundary conditions on the outer surfaces of the model domain, which is a vacuum cube ten times the size of the plate. The relative permeability of the steel plate is set as a parameter that varies between 50 and 500 with steps of 50. A 3D representation of the FE model with the background field as a vector plot can be seen in Figure 4.9.
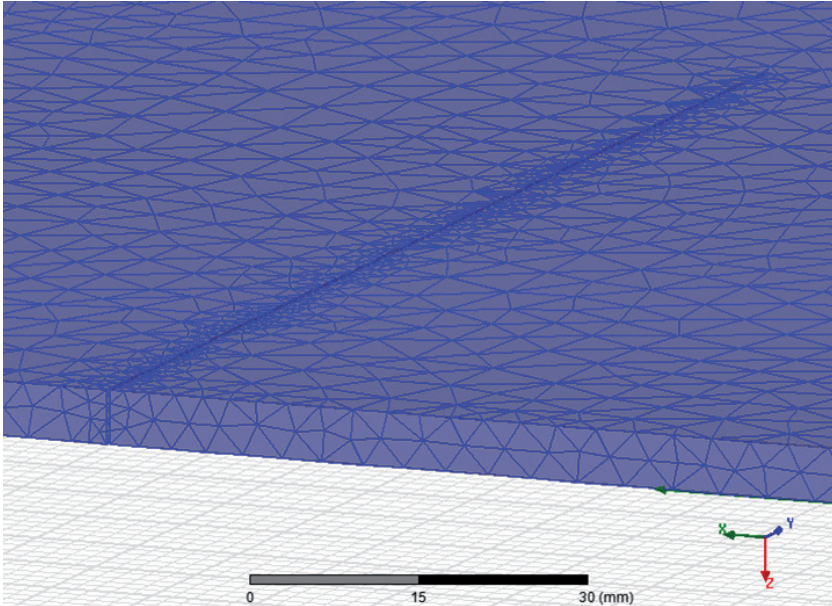
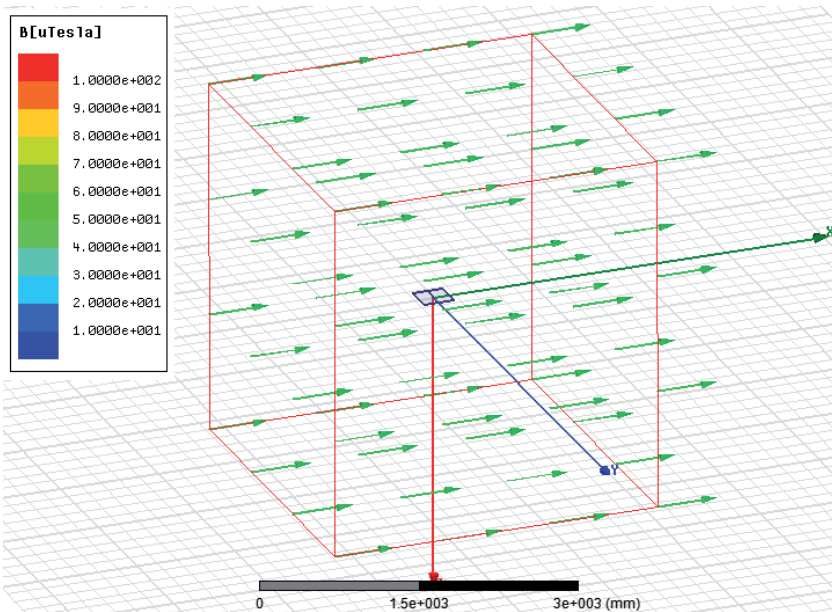Figure 4.8: FE model 2 local mesh refinement around slit.

Figure 4.9: FE model 2 with background field.

4.3. Results

4.3.1. Experiment 1

The first set of measurements with the plate as shown in Figure 4.3 results in a total magnetic field as depicted in Figure 4.10. The second set of measurements with the plate rotated 180 degrees around the Z-axis results in a total magnetic field as depicted in Figure 4.11. In both figures, the grey square shows the location of the steel plate.
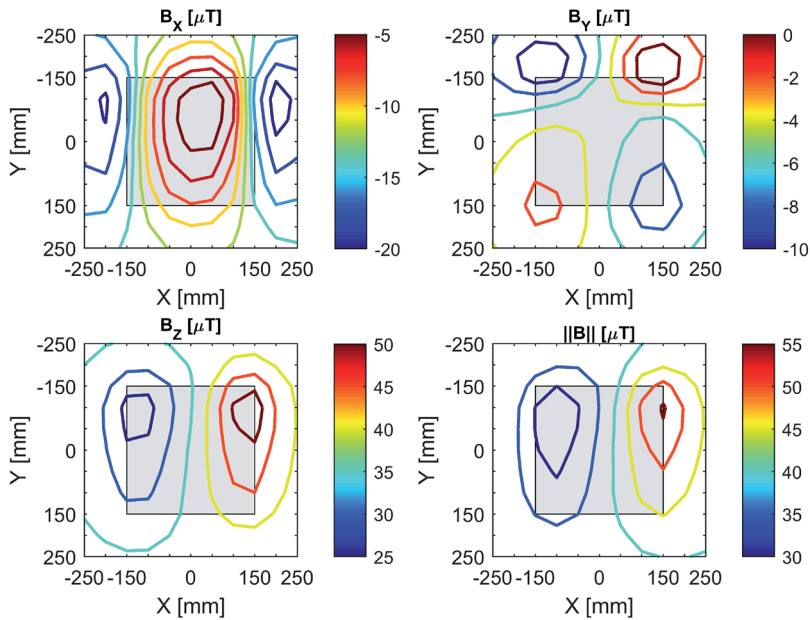

Figure 4.10: Experiment 1 - Total magnetic field $B_{tot,1}$ 75 mm above the plate surface.
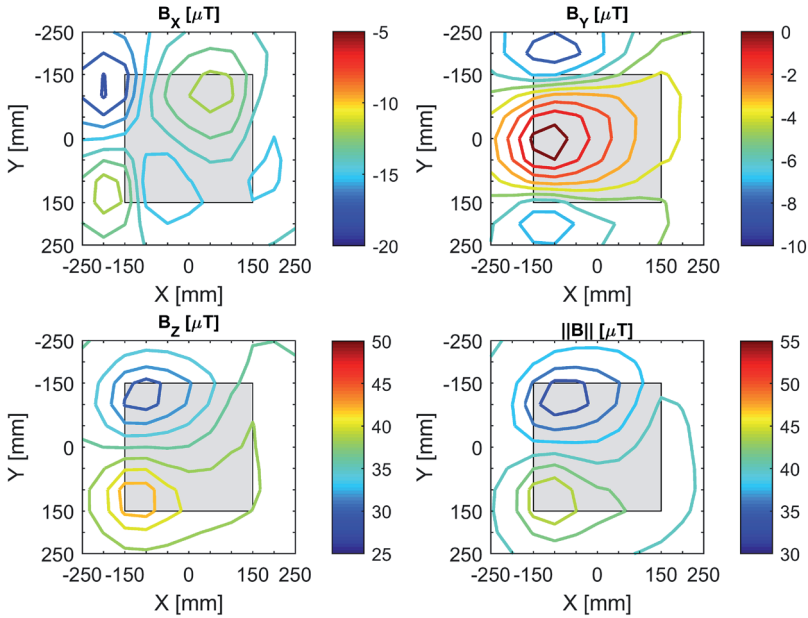
Figure 4.11: Experiment 1 - Total magnetic field $B_{tot,2}$ 75 mm above the plate surface.

When no stresses in the material, the total magnetic field consists of the background field, induced field, and permanent field. First, the background field is subtracted from the total field measurements to obtain the reduced fields:

$$\vec{B}_{red,1}(i,j) = \vec{B}_{tot,1}(i,j) - \vec{B}_{BG}(i,j), \tag{4.1}$$

$$\vec{B}_{red,2}(i,j) = \vec{B}_{tot,2}(i,j) - \vec{B}_{BG}(i,j), \tag{4.2}$$

for $i = -5, \dots, 5$ and $j = -5, \dots, 5$.

Now, the reduced fields $\vec{B}_{red,1}$ and $\vec{B}_{red,2}$ consist of an induced part and a permanent part:

$$\vec{B}_{red,1}(i,j) = \vec{B}_{red,1}^{ind}(i,j) + \vec{B}_{red,1}^{per}(i,j), \tag{4.3}$$

$$\vec{B}_{red,2}(i,j) = \vec{B}_{red,2}^{ind}(i,j) + \vec{B}_{red,2}^{per}(i,j), \tag{4.4}$$

for $i = -5, \dots, 5$ and $j = -5, \dots, 5$.

When rotating the plate 180 degrees, the permanent magnetization rotates along and the induced magnetization stays the same. Also, the induced magnetization is symmetric in *i* and symmetric in *j*. This yields:

$$\vec{B}^{ind}(i,j) = \vec{B}^{ind}_{red,1}(i,j) = \vec{B}^{ind}_{red,2}(i,j) = \vec{B}^{ind}_{red,2}(-i,-j), \qquad (4.5)$$

$$\vec{B}^{per}(i,j) = \vec{B}^{per}_{red,1}(i,j) = -\vec{B}^{per}_{red,2}(-i,-j), \qquad (4.6)$$

for $i = -5, \dots, 5$ and $j = -5, \dots, 5$.

Finally, combining equations 4.3 to 4.6 results in the following equations for the induced and permanent magnetic fields:

$$\vec{B}^{ind}(i,j) = \frac{\vec{B}_{red,1}(i,j) + \vec{B}_{red,2}(-i,-j)}{2}, \qquad (4.7)$$

$$\vec{B}^{per}(i,j) = \frac{\vec{B}_{red,1}(i,j) - \vec{B}_{red,2}(-i,-j)}{2}, \qquad (4.8)$$

for $i = -5, \dots, 5$ and $j = -5, \dots, 5$.

The resulting induced and permanent magnetic fields are shown in Figure 4.12 and Figure 4.13 respectively. Note that by rotation around the Z-axis only the permanent parts of the in-plane components of the field distribution B_X and B_Y can be eliminated.
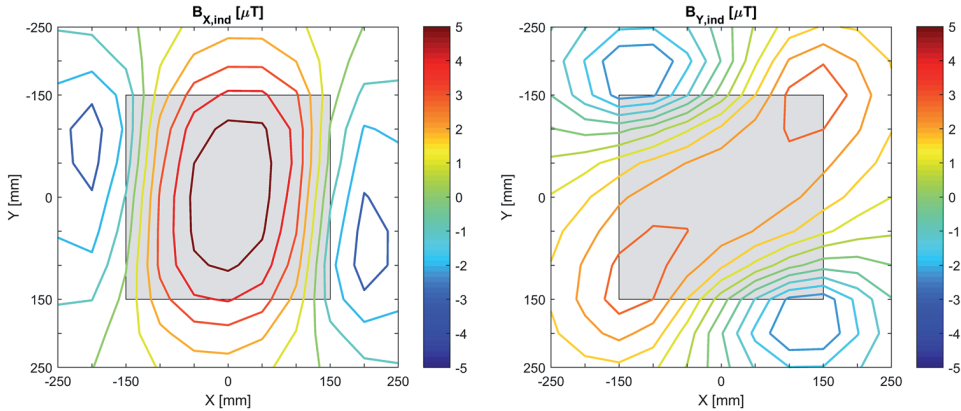

Figure 4.12: Experiment 1 - Measured induced magnetic field 75 mm above the plate surface.
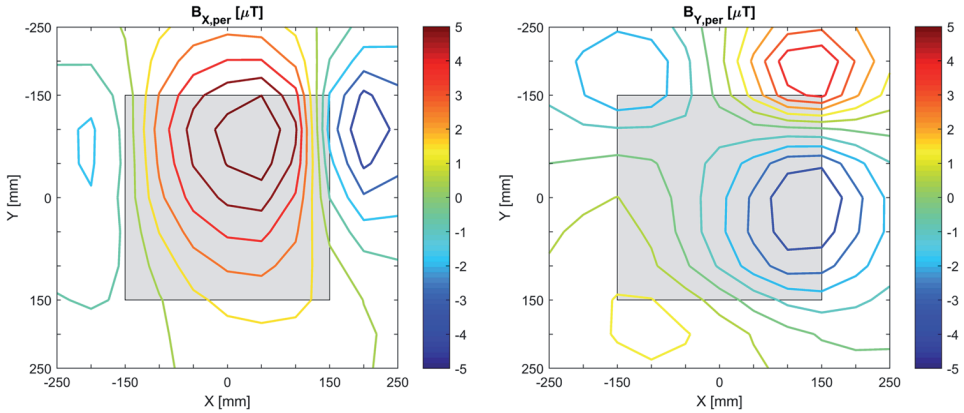
Figure 4.13: Experiment 1 - Measured permanent magnetic field 75 mm above the plate surface.

4.3.2. Comparison with FE Model 1

Now that the induced magnetic field has been extracted from the measurements of Experiment 1, it can be compared with the FE results in function of the relative permeability of the steel plate. This involves obtaining B_X and B_Y from the FE model in all 121 points of the measurement grid for each relative permeability and plotting the deviations from the experimental values by calculating the Root Mean Squared Error (RMSE) as follows:

$$RMSE = \sqrt{\frac{1}{121}\sum_{k=1}^{121}\left[B_{ind}^{FEM}(k) - B_{ind}^{Exp}(k)\right]^2}. \tag{4.9}$$

The results are shown in Figure 4.14. It can be seen from the RMSE distributions that the best agreement occurs at $\mu_r = 350$ for B_X and at $\mu_r = 450$ for B_Y, which are marked in red as the minimum RMSE values. Since the background field is approximately three times larger in X-direction than in Y-direction, the curve for B_X will likely be more reliable than for B_Y, so the relative permeability is likely to be closer to 350.
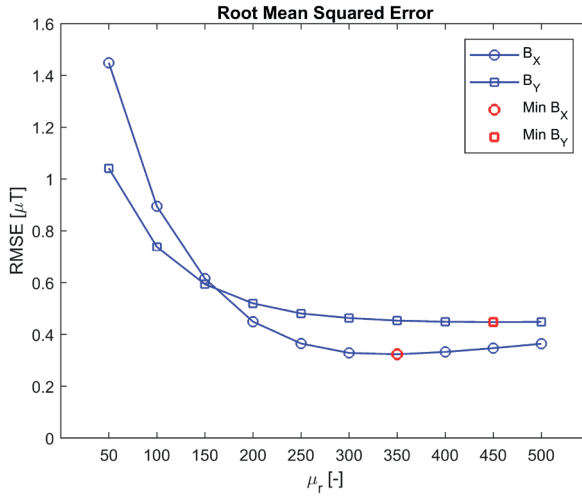
Figure 4.14: Experiment 1 - RSME between measurements and FE results.

To illustrate the similarity between the measurements and FE results, the FE results for $\mu_r = 350$ are shown in Figure 4.15, which are in good agreement with the experimental results from Figure 4.12 despite any measurement errors.
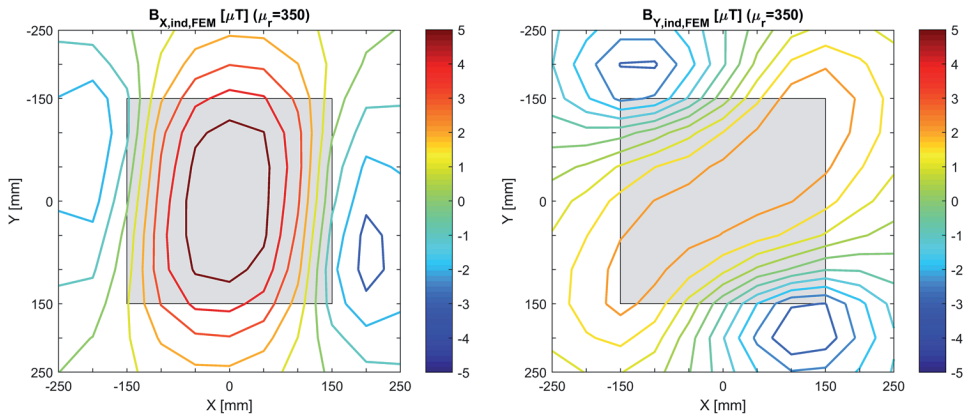

Figure 4.15: Experiment 1 - FE results induced magnetic field 75 mm above the plate surface.

4.3.3. Experiment 2

The magnetic field measurements above the plate with a slit while in a background field of 50 µT in X-direction applied by the magnetic field simulator are shown in Figure 4.16. The figure shows both the position of the plate in grey and the measurement domain. Note that only the values in X and Z-direction are shown

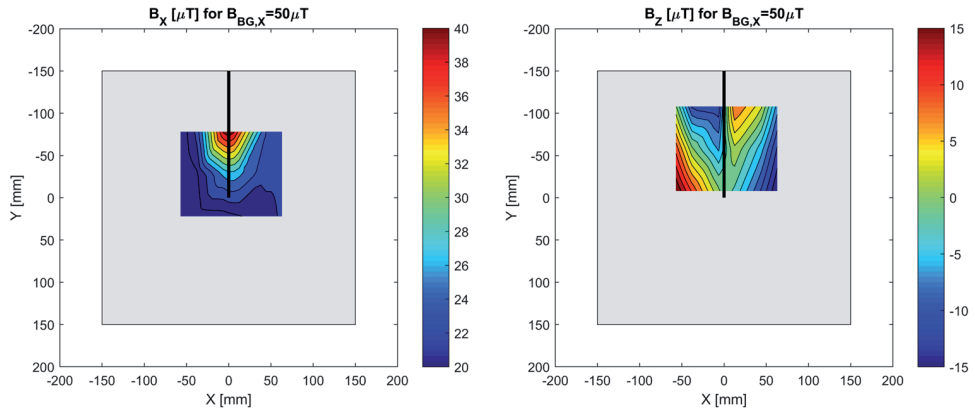because the background field is in X-direction and the magnetic flux leakage signal is in Z-direction.

Figure 4.16: Experiment 2 - Measured total magnetic field 30 mm above the plate surface.

To be able to separate the induced and permanent magnetic fields, the measurements are repeated while the magnetic field simulator creates a zero field condition around the plate. Consequently, this set of measurements results in the permanent magnetic field distribution, see Figure 4.17. Subtracting the permanent field from the total field results in the induced magnetic field, see Figure 4.18.
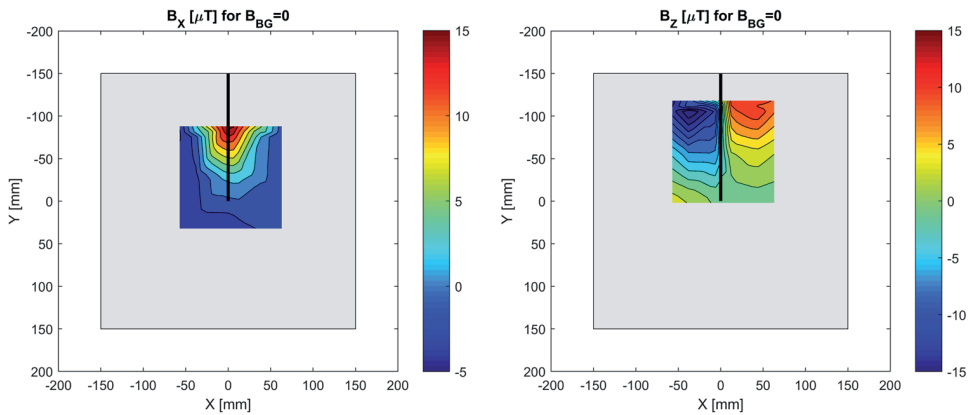

Figure 4.17: Experiment 2 - Measured permanent magnetic field 30 mm above the plate surface.
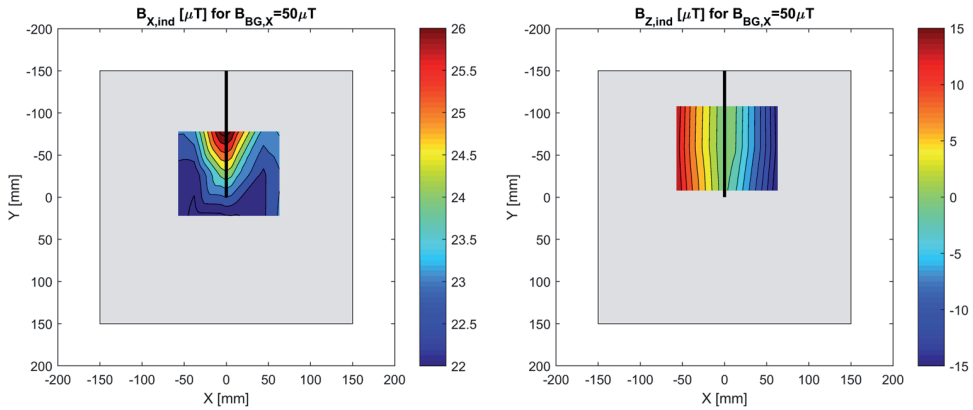
Figure 4.18: Experiment 2 - Measured induced magnetic field 30 mm above the plate surface.

4.3.4. Comparison with FE Model 2

The FE model described in section 4.2.4 is analyzed with a relative permeability of the steel plate ranging from 50 to 500 with a step size of 50. For each solution, B_X and B_Z are obtained in the 45 points of the measurement grid 30 mm above the plate surface. To show the deviation between measurements and FE results, the Root Mean Squared Error (RMSE) is calculated according to equation 4.9 with $n = 45$.

The resulting RMSE distributions are shown in Figure 4.19. It can be seen from the RMSE distributions for both B_X and B_Z that the best agreement is for a relative permeability between 200 and 250. By running an additional simulation, it is shown that the minima for both RMSE curves, which are marked in red, occur for a relative permeability of 225.

To illustrate the similarity between the measurements and FE results, the FE results for $\mu_r = 225$ are shown in Figure 4.20, which are almost identical to the experimental results in Figure 4.18.
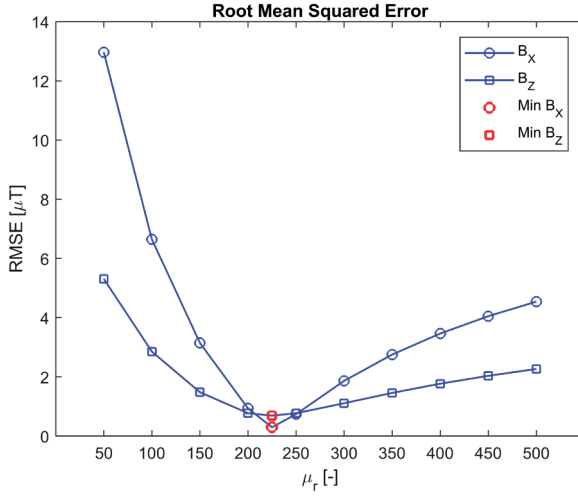
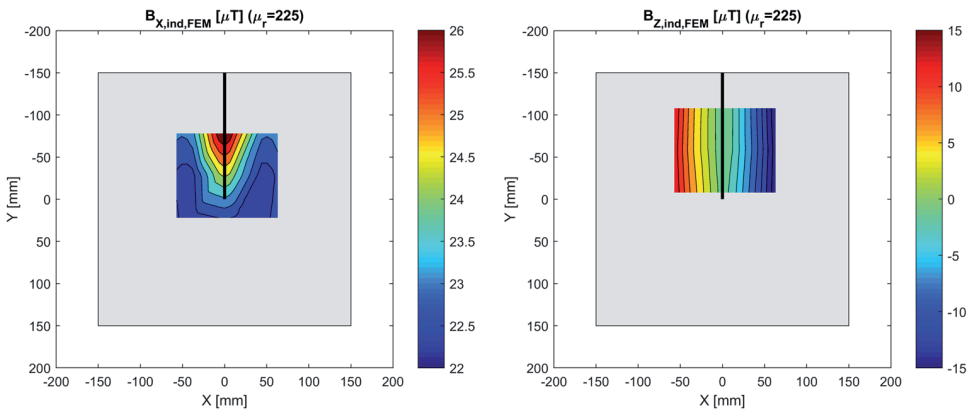Figure 4.19: Experiment 2 - RMSE between measurements and FE results.

Figure 4.20: Experiment 2 - FE results induced magnetic field 30 mm above the plate surface.

4.4. Discussion

Considering the great similarity between measurements and FE results for both experiments, the presented separation techniques of induced and permanent magnetic fields are successful. From the comparison of the measured induced magnetic field with FE results for varying μ_r, it follows that the plate from Experiment 1 has a relative permeability of approximately 350 and that the plate with a slit from Experiment 2 has a relative permeability of approximately 225. An important assumption is that the relative permeability of the steel plates is uniformly distributed

and isotropic. To get more insight in the distribution of the material properties, the error distributions between measurements and FE results for Experiment 1 and Experiment 2 are shown in Figure 4.21 and Figure 4.22 respectively as a percentage of the maximum absolute measured value.
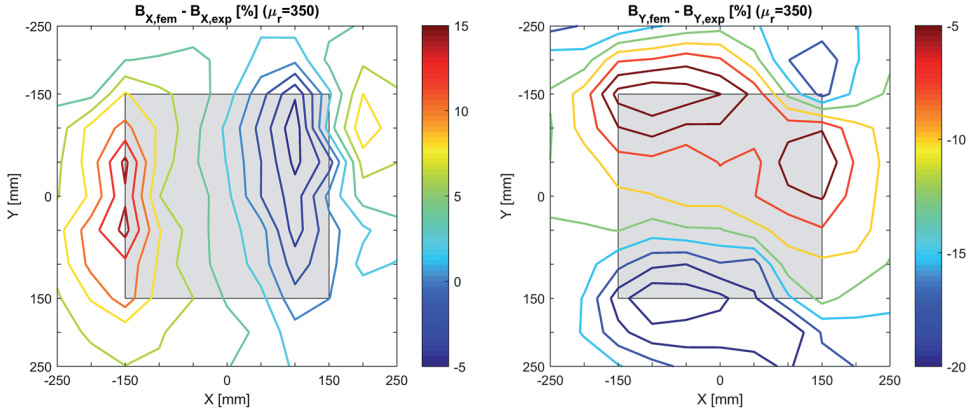

Figure 4.21: Experiment 1 - Error distribution between FE results and measurements.
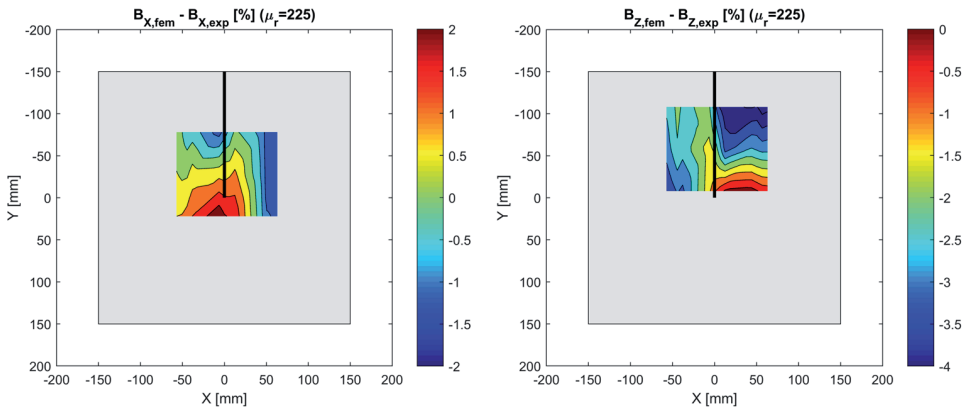
Figure 4.22: Experiment 2 - Error distribution between FE results and measurements.

Experiment 1 shows much larger errors than Experiment 2, which is most likely due the large distance between the measurement domain and the plate and the relatively poor precision of the automatic sensor positioning system, both resulting in larger measurement errors. As could be expected, the largest errors for Experiment 1 are along the plate's edges where the magnetic field has the largest spatial gradient. The magnetic field in X-direction is expected to deviate most near the left and right edges and the field in Y-direction is expected to deviate most near the top and bottom edges, which is confirmed by Figure 4.21. The small errors away from the plate's

edges indicate that the relative permeability is likely to be uniformly distributed as was assumed in the FE model.

Figure 4.22 shows that for Experiment 2 the deviations between FE results and measurements are well within 5% of the maximum absolute measured value for a relative permeability of 225 for the steel plate. The small errors indicate that the separation technique using the magnetic field simulator is successful and that a uniform and isotropic relative permeability of 225 may be assumed for this steel plate. Previous research described in Chapter 3 in which a sample was wire cut from the exact same steel plate and analyzed concluded that the relative permeability is approximately 115. The difference between these results could mean that the sample manufacturing process had a significant effect on the magnetic material properties of the sample.

The measured permanent magnetic field distribution in Experiment 1 shows that the permanent magnetization of a steel plate can be non-uniformly distributed in an unpredictable manner, see Figure 4.13. The permanent magnetic field shows an unexpected local concentration above the top right corner of the plate. Therefore, it is challenging to determine the correct permanent magnetization for numerical simulation by FEM. At the same time, the measured permanent magnetic field distribution in Experiment 2 shows that for a plate with a slit, the permanent magnetization contributes significantly to the SMFL.

4.5. Conclusions

Being able to simulate novel crack monitoring methods based on the SMFL is important for the further development of these methods towards application on ship and offshore structures, ultimately leading to a reduction of operational expenses and increasing safety. The correct interpretation of the measured SMFL around a fatigue crack in a steel structure is needed to accurately size the crack. This involves thoroughly understanding all the sources that cause the SMFL, which can be subdivided into Earth-induced magnetization and permanent magnetization. The aim of this chapter was to determine the magnetic permeability of structural steels for simulation of the induced magnetic field distribution around cracks using FEM.

Magnetic measurements were done above an FeE235 steel plate without defect (Experiment 1) and with a straight slit representing a fatigue crack (Experiment 2). The induced and permanent magnetic fields were separated using two different techniques. Comparing FE results with the measured induced magnetic

fields suggests that the relative permeability of the plate from Experiment 1 is approximately 350 and that of Experiment 2 is approximately 225. Apparently, not every FeE235 steel plate has the same magnetic permeability. The error distributions between FE results and measurements suggest that the magnetic permeability of both plates are reasonably uniform. The measured permanent magnetic field in Experiment 1 confirms the hypothesis that the permanent magnetization of structural steel can be non-uniform. Its non-uniformity together with its relation to unknown stress and temperature histories make it challenging to model the permanent magnetization accurately.

4

4.6. References

[1]   Dubov A. A Study of Metal Properties Using the Method of Magnetic Memory. Met Sci Heat Treat 1998;39:401–5.

[2]   Yao K, Deng B, Wang ZD. Numerical studies to signal characteristics with the metal magnetic memory-effect in plastically deformed samples. NDT E Int 2012;47:7–17. doi:10.1016/j.ndteint.2011.12.004.

[3]   Wang ZD, Yao K, Deng B, Ding KQ. Theoretical studies of metal magnetic memory technique on magnetic flux leakage signals. NDT E Int 2010;43:354–9. doi:10.1016/j.ndteint.2009.12.006.

[4]   Wang ZD, Gu Y, Wang YS. A review of three magnetic NDT technologies. J Magn Magn Mater 2012;324:382–8. doi:10.1016/j.jmmm.2011.08.048.

[5]   Jiles DC, Atherton DL. Theory of ferromagnetic hysteresis (invited). J Appl Phys 1984;55:2115–20. doi:10.1063/1.333582.

[6]   Davey KR. Calculation of magnetic remanence. IEEE Trans Magn 2009;45:2907–11. doi:10.1109/TMAG.2009.2014562.

[7]   Atherton DL, Jiles DC. Effects of stress on magnetization. NDT Int 1986;19:15–9. doi:10.1016/0308-9126(86)90135-5.

[8]   Jiles DC, Devine MK. The law of approach as a means of modelling the magnetomechanical effect. J Magn Magn Mater 1995;140–144:1881–2. doi:10.1016/0304-8853(94)00928-7.

[9]   Li L, Jiles DC. Modified Law of Approach for the Magnetomechanical Model: Application of the Rayleigh Law to Stress. IEEE Trans Magn 2003;39:3037–9. doi:10.1109/TMAG.2003.815882.

[10]   Bulte DP, Langman R a. Origins of the magnetomechanical effect. J Magn Magn Mater 2002;251:229–43. doi:10.1016/S0304-8853(02)00588-7.

[11]   Schwerer FC, Spangler CE, Kelly JF. Temperature dependence of the magnetic coercivity of pearlite. Acta Metall 1978;26:579–89. doi:10.1016/0001-

6160(78)90110-4.

[12]   Kuz'min MD. Shape of temperature dependence of spontaneous magnetization of ferromagnets: Quantitative analysis. Phys Rev Lett 2005;94:16–9. doi:10.1103/PhysRevLett.94.107204.

[13]   Van der Horst MP, Kaminski ML, Lepelaars E. Testing and Numerical Simulation of Magnetic Fields Affected by Presence of Fatigue Cracks. Proc. Int. Offshore Polar Eng. Conf., Anchorage, Alaska: International Society of Offshore and Polar Engineers; 2014, p. 445–50.

[14]   H. Hwang J, Lord W. Finite Element Modeling of Magnetic Field/Defect Interactions. ASTM J Test Eval 1975;3:21–5.

[15]   Tanner BK, Szpunar JA, Willcock SNM, Morgan LL, Mundell PA. Magnetic and metallurgical properties of high-tensile steels. J Mater Sci 1988;23:4534–40. doi:10.1007/BF00551956.

[16]   Thompson SM, Tanner BK. The magnetic properties of pearlitic steels as a function of carbon content. J Magn Magn Mater 1993;123:283–98. doi:10.1016/0304-8853(93)90454-A.

[17]   Chung H, Yang C, Jung W. A Magnetic Field Separation Technique for a Scaled Model Ship through an Earth's Magnetic Field Simulator. J Magn 2015;20:62–8.

[18]   Somsen OJG, Wagemakers GPM. Separating Permanent and Induced Magnetic Signature: A Simple Approach. Int J Electr Comput Energ Electron Commun Eng 2015;9:1236–9.
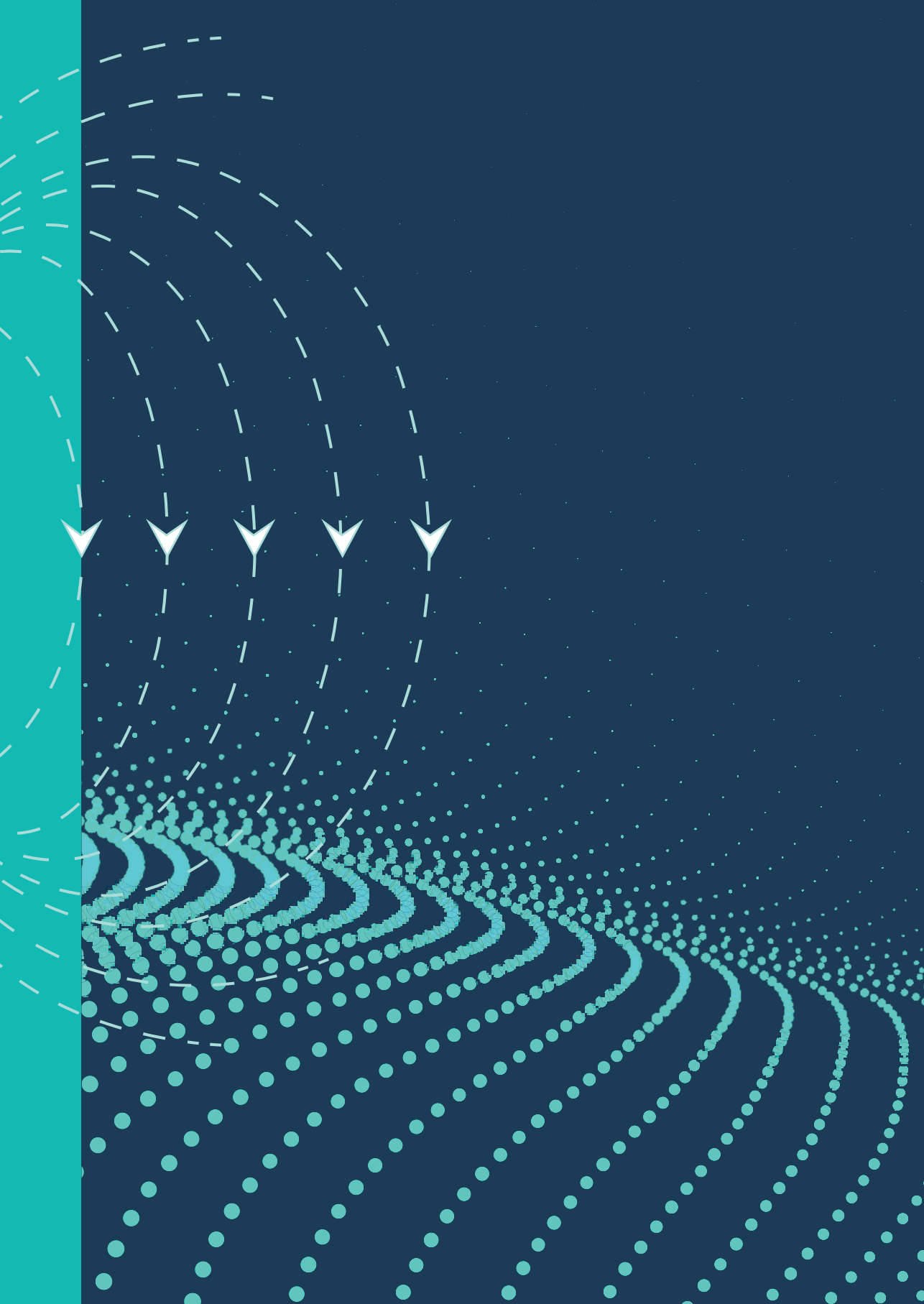
4

5

Simulation and Analysis of Earth-Induced Magnetic Flux Leakage for Monitoring Cracks in Ship and Offshore Structures

Abstract

The Earth's magnetic field may contribute significantly to the Self Magnetic Flux Leakage (SMFL) near defects. The interaction between the Earth's magnetic field and a ferromagnetic structure with a crack is dependent on many unknown factors. To aid in the interpretation of SMFL measurements for crack monitoring purposes, numerical simulation and analysis of the Earth-induced Magnetic Flux Leakage is carried out in this chapter. Results from finite element models of a center and through thickness cracked steel plate, and a double-sided and not fully penetrated fillet welded steel T-joint with a through thickness crack at one weld toe show that altitude, Earth field orientation, crack opening, crack length and geometries of welded joints have a significant effect on the Earth-induced Magnetic Flux Leakage. It is concluded that the envisaged passive magnetic crack monitoring system should have sensors at an optimal altitude by balancing sensor sensitivity and amount of sensors needed, their sampling frequency should be dictated by the loading frequency to cope with crack opening, and a correction on the measured data may be needed to cope with changing orientation in the Earth's magnetic field. Furthermore, sensors will need to be placed above the weld surface for reliable monitoring of a weld toe crack in a double-sided and not fully penetrated fillet welded T-joint.

5.1. Introduction

The Metal Magnetic Memory (MMM) method can provide a good solution for a reliable, wireless, robust, and inexpensive crack monitoring system suitable for marine structures [1]. The challenge with this technique lies with interpreting the Self Magnetic Flux Leakage (SMFL) measurements without active magnetization to determine the crack's length and/or depth. Earlier research [2] showed how the magnetization in an unloaded steel plate is caused by two separate sources: the induced and permanent magnetization. When the specimen is loaded, a third source, the stress magnetization [3–5], is present. This chapter, however, focuses primarily on the induced magnetization caused by the Earth's magnetic field as it is the only contribution that can be modeled accurately.

The aim of the research presented in this chapter is to numerically simulate and analyze the Earth-induced Magnetic Flux Leakage (MFL) near cracks in ship and offshore structures. A previous study already decoupled the induced and permanent magnetic fields from magnetic measurements above a steel plate with a straight slit [6]. The measured induced magnetic field compared very well with a linear Finite Element (FE) model using an isotropic relative magnetic permeability of 225 for the entire plate as errors were within 5%. The research in this chapter follows a similar procedure using a linear magneto-static FE model to simulate the Earth-induced magnetic field around steel plates with cracks. A set of parameters is then investigated that increase the complexity of the model as a stepping stone towards modeling an actual crack in a marine structure. Such modeling capability will be useful when designing a passive magnetic crack monitoring system for ship and offshore structures.

Section 5.2 describes the FE models that have been used for this study. The results are shown in section 5.3. First, the results of a base model of a square plate with a center crack are shown. Then, the effects of altitude, Earth field orientation, crack opening, and crack length are analyzed in separate subsubsections. The final subsubsection shows the results for the model of a double-sided and not fully penetrated fillet welded steel T-joint with a through thickness crack at one weld toe. The results are discussed in section 5.4 and conclusions are drawn in section 5.5.

5.2. Method

To conduct this study, two linear magneto-static FE models are made using the software package ANSYS Maxwell. The first model is a relatively simple one: a square

plate with a center crack. A numerical parametric study is performed on this model to investigate the effects of altitude, Earth field orientation, crack opening, and crack length on the Earth-induced MFL. The second model has a more complex geometry, which is a double-sided and not fully penetrated fillet welded steel T-joint with a through thickness crack at one weld toe. Cracks are often found in such configuration in ship and offshore structures. Both FE models are described in more detail in the two subsections below.

5.2.1. Square Plate with Center Crack

The first model represents a square steel plate of 1 m long and 10 mm thick with a through thickness crack of 50 mm long and 1 mm wide in the middle of the plate. The plate is modeled as a magnetically linear material, which is a valid assumption for weak fields, with a relative magnetic permeability of 225 and without any permanent magnetization. The plate is meshed with linear tetrahedral elements with a maximum edge length of 30 mm and local mesh refinement near the crack surface and in a plane 1 mm above the crack for post-processing purposes. The maximum edge length in the mesh refinement area is 1 mm. The FE mesh near the crack can be seen in Figure 5.1.
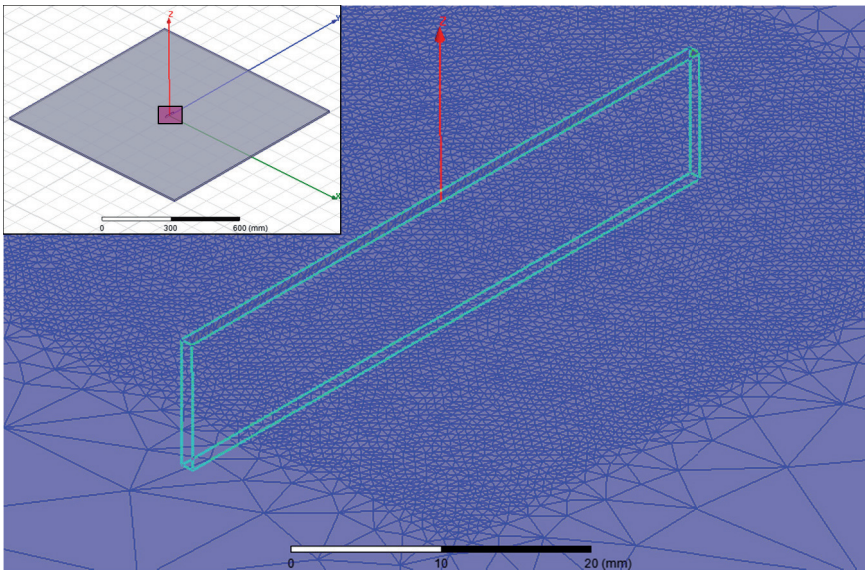

Figure 5.1: Local mesh refinement near the crack in the square plate.

The calculation domain consists of a vacuum box 10 times the size of the plate. Boundary conditions are imposed on the outer surfaces of the box resulting in a homogeneous background field of 50 µT, which is approximately the magnetic field

strength of the Earth, in positive X-direction. A 3D representation of the entire model including the background field as a vector plot can be seen in Figure 5.2.
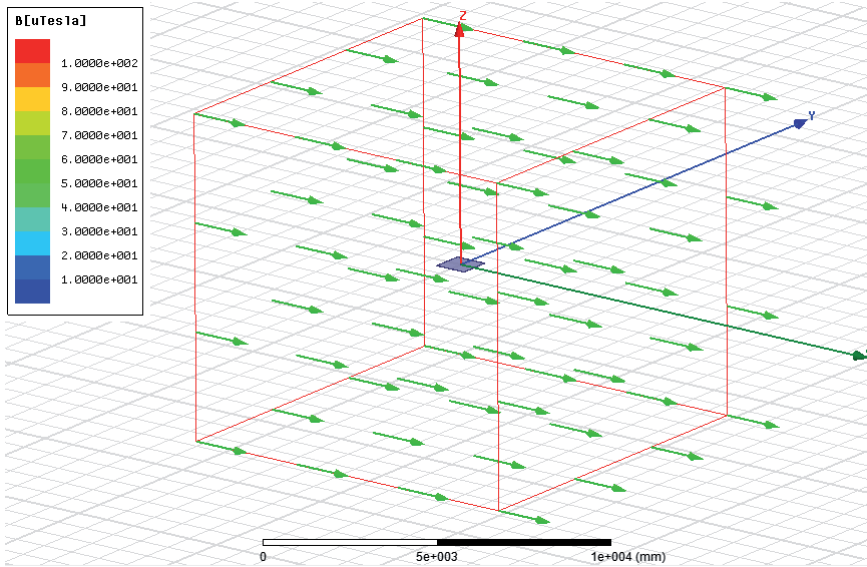

Figure 5.2: FE model center cracked plate with background field as vector plot.

5.2.2. T-joint with Weld Toe Crack

The second model is of a T-joint section with a steel base plate of 400x200x5 mm and a steel stiffener plate of 400x100x5 mm joined together with a double-sided and not fully penetrated fillet weld. Along the weld toe in the middle of the base plate, there is a through thickness crack of 100 mm long and 1 mm wide. A cross section of the T-joint section with the weld toe crack can be seen in Figure 5.3.
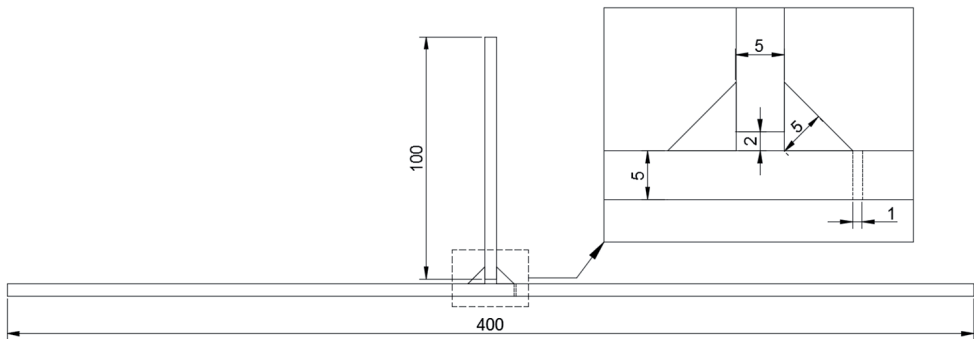

Figure 5.3: Cross section of double-sided and not fully penetrated fillet welded T-joint with through thickness crack at one weld toe.

The steel plates and the welds are modeled as a magnetically linear material with a relative permeability of 225 and they are meshed with linear tetrahedral elements with a maximum edge length of 10 mm. Near the crack, the mesh is locally refined with a maximum edge length of 1 mm. The FE mesh near the crack can be seen in Figure 5.4.
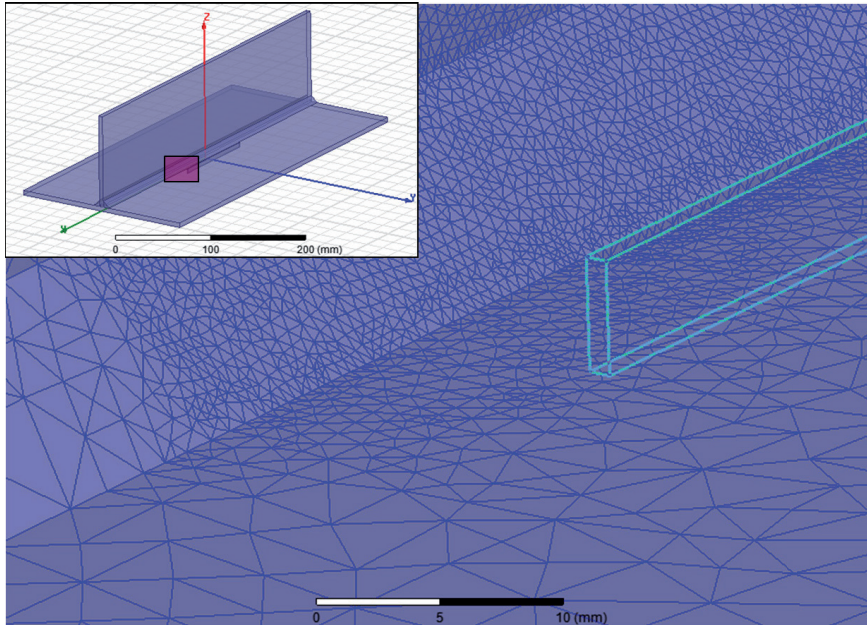
Figure 5.4: Local mesh refinement near the weld toe crack in the T-joint.

Like in the previous FE model, the calculation domain is a vacuum box with a homogenous background field imposed through boundary conditions on the outer surfaces of the domain. The background field is also 50 µT but now in positive Y-direction as the X-axis coincides with the longitudinal direction of the T-joint section. A 3D representation of the entire model including the background field as a vector plot can be seen in Figure 5.5.

Figure 5.5: FE model of T-joint with background field as vector plot.

5.3. Results

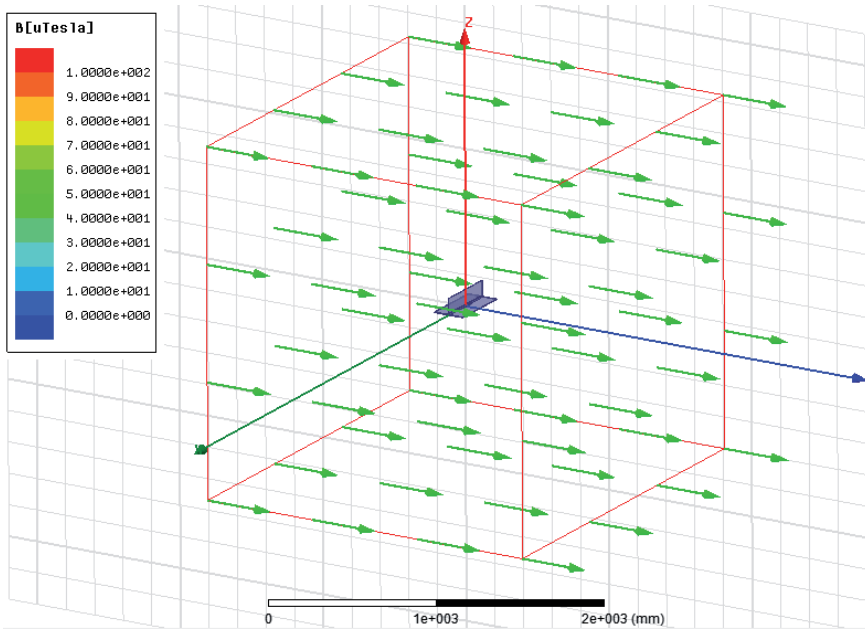This section presents the results of the FE models that were described in section 5.2. Like the Method section, there are two subsections each describing the results of one FE model. First, the results of the square plate with a center crack are shown. By varying certain parameters in the model or in the post-processing, the effects of altitude, Earth field orientation, crack opening, and crack length are presented. Each of these effects are discussed in four separate subsubsections. Then, the results of the welded T-joint with weld toe crack are shown.

5.3.1. Square Plate with Center Crack

Before moving to the parameter study, the FE results of the base model as described in subsection 5.2.1 are shown. Figure 5.6 shows the magnetic flux density as a vector plot on the midplane cross section of the steel plate in the vicinity of the crack. As can be expected, the magnetic flux lines tend to move around the crack causing a local increase of magnetic flux density around the crack tips.
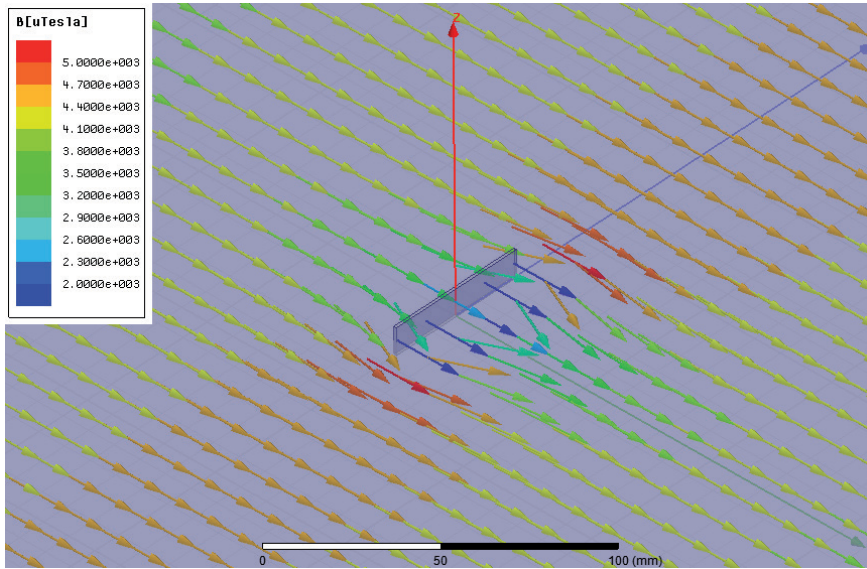
Figure 5.6: Magnetic flux density in midplane cross section.

At the top and bottom faces of the steel plate, magnetic flux lines not only tend to move around the crack in the XY-plane, but also tend to leak out of the steel plate in the out-of-plane direction. This phenomenon is commonly known as Magnetic Flux Leakage (MFL). The MFL for this FE model is illustrated in Figure 5.7, which shows the magnetic flux density in Z-direction in the XY-plane 1 mm above the surface of the plate. The location of the crack can be clearly identified in between the positive and negative peaks on both sides of the crack.

Figure 5.7: Magnetic Flux Leakage around the crack at 1 mm above the surface of the plate.

❖ **Altitude Effect**

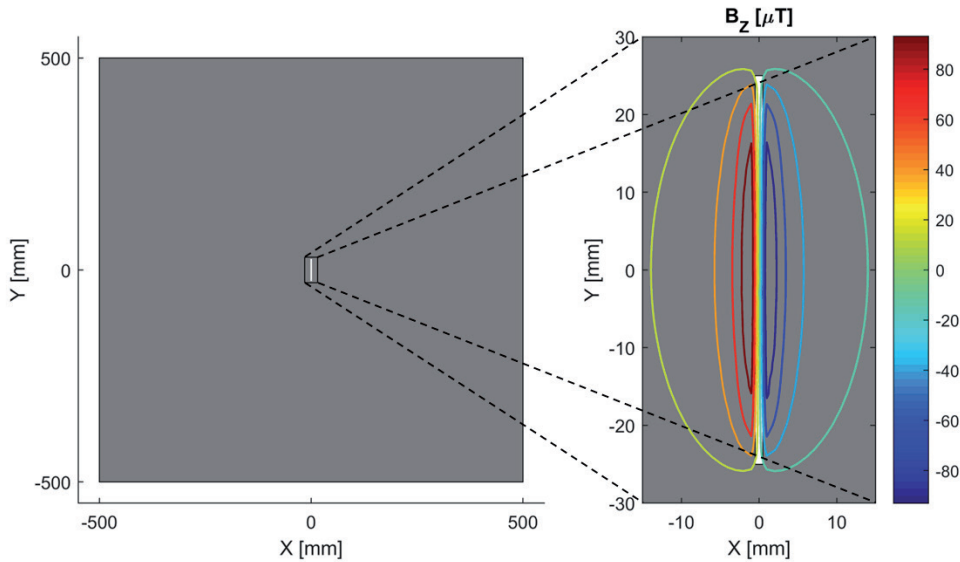The altitude is defined as the shortest distance from and perpendicular to the plate's surface to a point of interest outside the plate, for instance where a measurement probe is located. Since this distance is one of the design parameters for designing a crack monitoring system, it is important to investigate its effect on the MFL near the crack. Figure 5.7 shows the MFL for an altitude of 1 mm, which is very close to the plate's surface. Increasing the altitude causes a decay in the MFL as can be seen in Figure 5.8, which shows the out-of-plane magnetic flux density along the line at Y=0 for altitudes ranging from 1 to 10 mm.

The signal strength is defined as the peak-to-peak out-of-plane magnetic flux density, i.e. the maximum range of MFL. The signal width is defined as the distance between the positive peak and the negative peak of the MFL signal. Figure 5.9 shows the signal strength and signal width plotted against the altitude. With increasing altitude, the signal strength decreases like a power function and the signal width increases linearly.

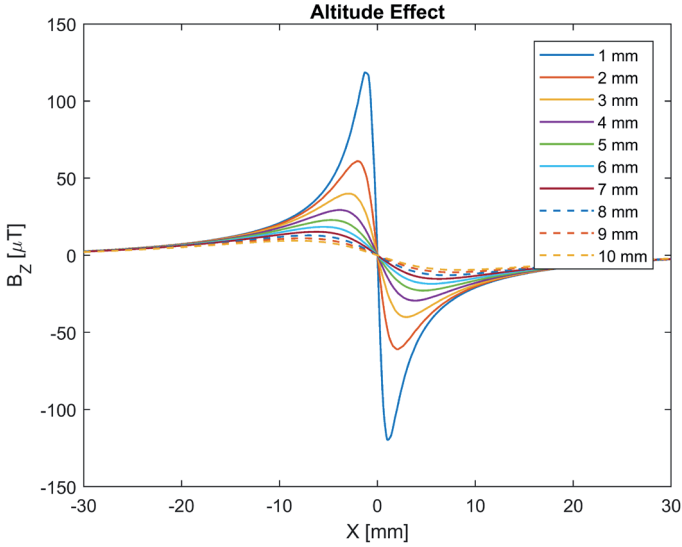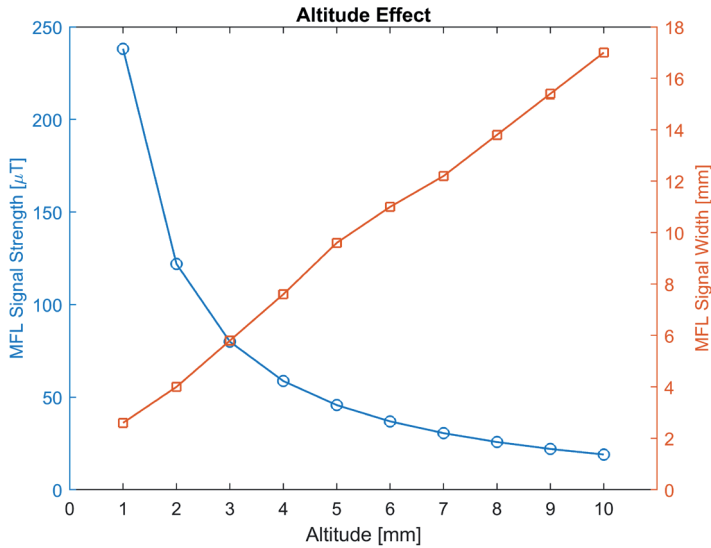Figure 5.8: Magnetic Flux Leakage at Y=0 for varying altitudes.

Figure 5.9: Effect of altitude on MFL signal strength and signal width.

❖ **Earth Field Orientation Effect**

The second parameter that is investigated is the orientation of the background field and its effect on the MFL signal near the crack. A passive magnetic crack monitoring system relies mainly on the Earth-induced magnetization and permanent

magnetization so when the orientation of the monitored object changes with respect to the Earth's magnetic field, it may have a significant effect on the measured signals. Therefore, in the FE model of the center cracked plate, the background field is varied from the positive X-direction, so perpendicular to the crack, to the positive Y-direction, so parallel to the crack, in steps of 15 degrees. The resulting MFL signals at an altitude of 1 mm for each of the different orientations are shown in Figure 5.10.
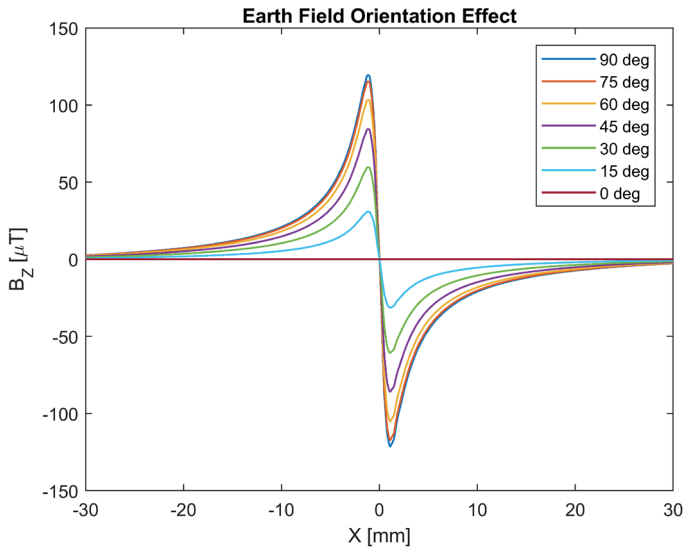
Figure 5.10: Magnetic Flux Leakage at Y=0 and altitude of 1 mm for varying Earth field orientations.

The signal width remains constant and signal strength decreases when the angle between the background field and the crack orientation gets smaller. In fact, the signal strength is exactly proportional to the sine of that angle, see Figure 5.11. It means that the MFL is proportional to the effective induced magnetization perpendicular to the crack.
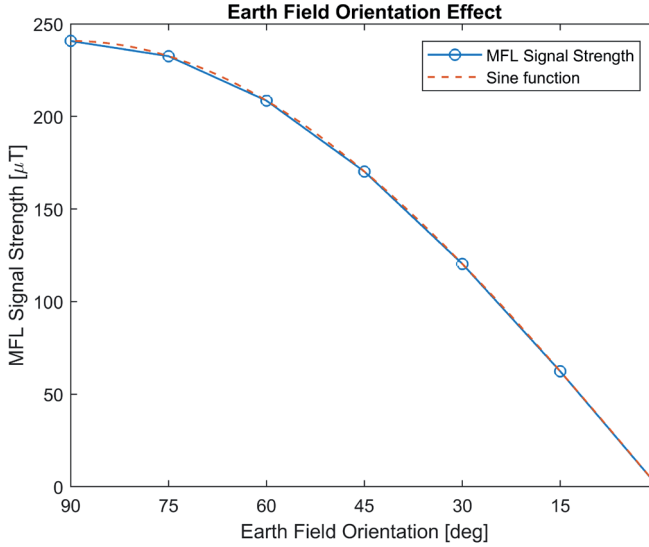
Figure 5.11: Effect of Earth field orientation on MFL signal strength at an altitude of 1 mm.

❖   **Crack Opening Effect**

The third parameter that is investigated is the crack opening displacement and its effect on the Earth-induced MFL. As ship and offshore structures are loaded cyclically by waves, cracks open and close continuously. Hence, a crack monitoring system needs to take into account the effect of the crack opening and closing on the measured signals for correct interpretation. To investigate the crack opening effect, the base model that was described in section 5.2.1 has been modified such that the width of the rectangular crack, the Crack Mouth Opening Displacement (CMOD), varies from 1 mm to 0.1 mm with steps of 0.1 mm. The resulting MFL curves along Y=0 and with an altitude of 1 mm are shown in Figure 5.12.

The crack width has a very small influence on the MFL signal width. However, the signal strength decreases rapidly when the crack width decreases. The effect of crack opening on the MFL signal strength is shown in Figure 5.13. As expected, the signal strength shows a rapid decay when the CMOD approaches zero as there is no MFL when no crack is present. The signal strength shows a monotonic increase for increasing CMOD. For a crack opening of 0.5 mm or larger (at altitude of 1 mm), the signal strength becomes less sensitive to the crack opening effect.
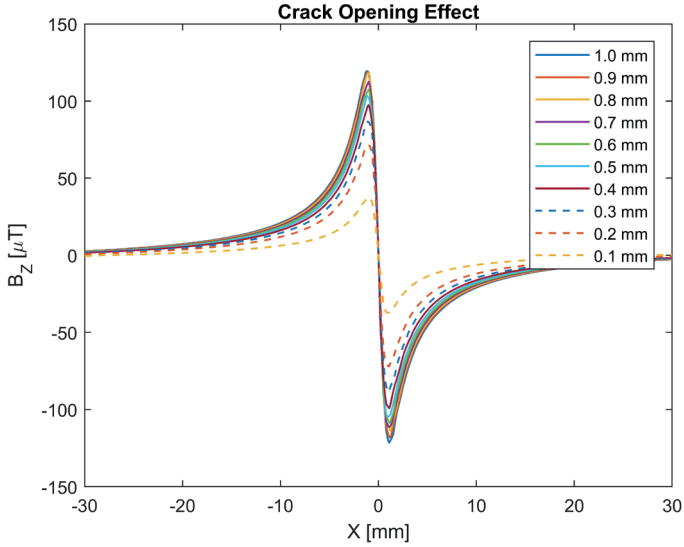
Figure 5.12: Magnetic Flux Leakage at Y=0 for varying crack widths at an altitude of 1 mm.
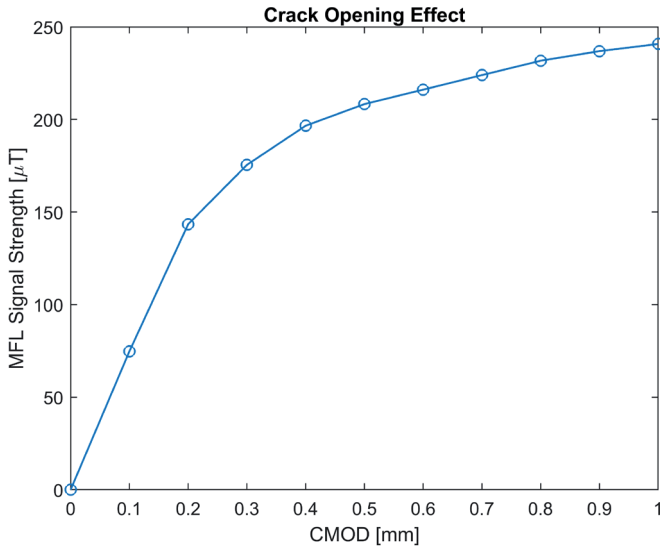
Figure 5.13: Effect of crack opening on MFL signal strength at an altitude of 1 mm.

❖ **Crack Length Effect**

Lastly but perhaps most importantly, the effect of crack length on the Earth-induced MFL is investigated. Ultimately, the most important output of a crack monitoring system for through thickness cracks is the crack length and its

propagation rate. To investigate the crack length effect, the base model that was described in section 5.2.1 has been modified such that the crack length varies from 50 mm to 150 mm with steps of 10 mm. The resulting MFL curves along Y=0 and with an altitude of 1 mm are shown in Figure 5.14.
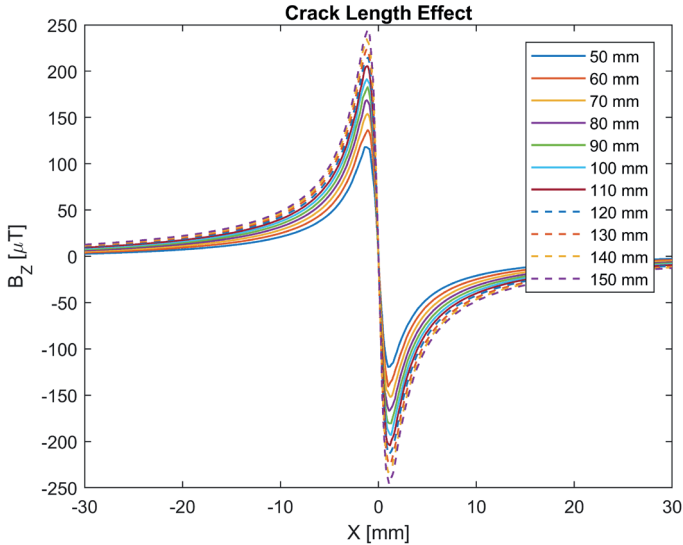
Figure 5.14: Magnetic Flux Leakage at Y=0 and altitude of 1 mm for varying crack lengths.

It can be seen that for increasing crack length, the signal strength increases monotonically but with a slowly decreasing rate. Figure 5.15 shows the crack length effect on the signal strength even more clearly. Note that the signal strengths for cracks lengths under 50 mm are added as well to illustrate that the MFL approaches zero when the crack is still very small.
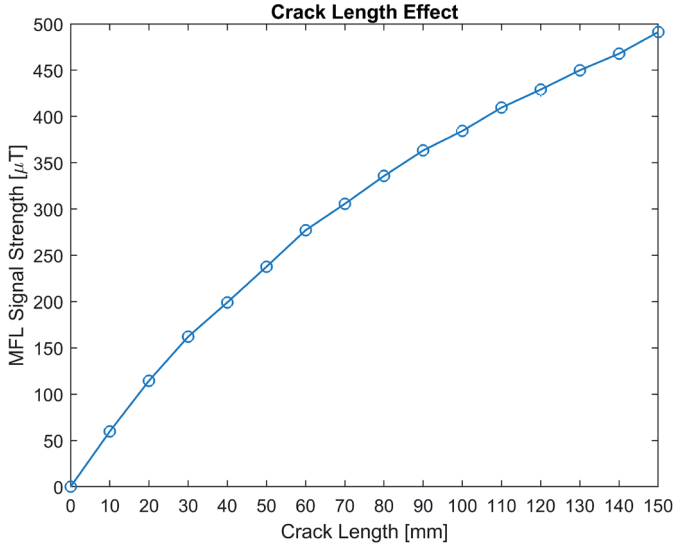
Figure 5.15: Effect of crack length on MFL signal strength at an altitude of 1 mm.

5.3.2. T-joint with Weld Toe Crack

The second FE model that is analyzed is a double-sided and not fully penetrated fillet welded steel T-joint with a through thickness crack at one weld toe. The goal is to investigate what the geometry effects are on the Earth-induced MFL for a crack configuration that is more common in ship and offshore structures than a center cracked plate. The flow of magnetic flux through the T-joint section is shown in Figure 5.16 as a vector plot in the cross section at X=0, so in the middle of the model.

Several observations can be made from Figure 5.16. Firstly, it is clear that the background field in this model is in positive Y-direction as the majority of magnetic flux is flowing from left to right. Secondly, a significant amount of magnetic flux is moving through the weld into the stiffener plate in positive Z-direction. Still, the majority of magnetic flux remains in the base plate. Note that in this model the weld material has the same magnetic properties as the steel plates. In most cases, weld material has a lower magnetic permeability so less magnetic flux would move through the weld into the stiffener plate. The last observation is that near the crack, both above and below the base plate, the magnetic flux density has a small component in the out-of-plane direction.
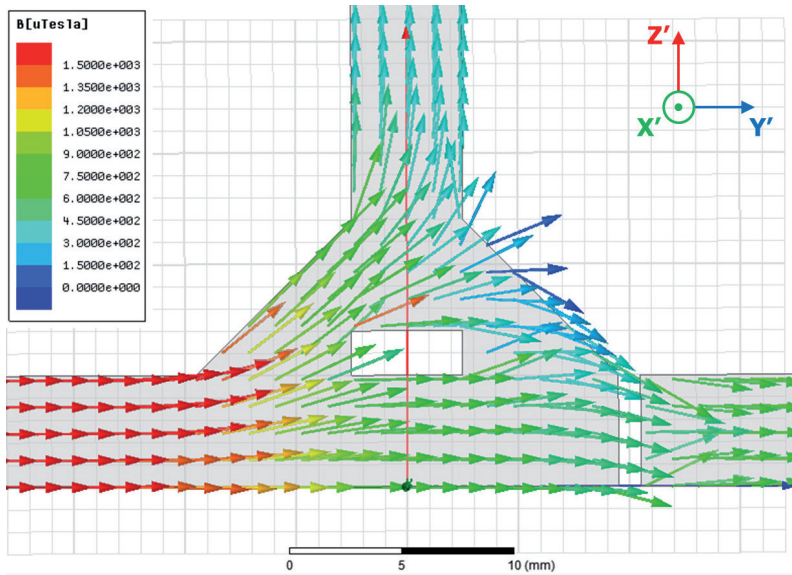
Figure 5.16: Magnetic flux density as vector plot in cross section of T-joint at X=0.

The out-of-plane component of the magnetic flux density in the T-joint near the crack causes MFL into the surrounding air. The magnetic flux density in the cross section of air at X=0 is shown as a vector plot in Figure 5.17 in which the MFL near the crack can be clearly identified.
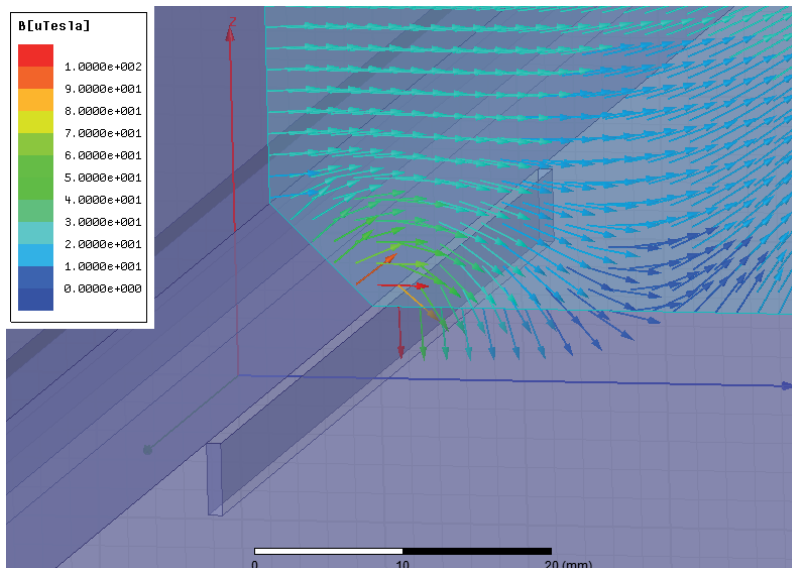
Figure 5.17: Magnetic flux density as vector plot in cross section of air at X=0.

The MFL near the crack becomes even more apparent when plotting the out-of-plane component of the magnetic flux density as a surface plot at 1 mm altitude, see Figure 5.18, and as line plots at 1 mm altitude at several locations along half of the crack, see Figure 5.19. The line plots above the weld surface and above the base plate surface are shown separately as the out-of-plane magnetic flux density above the weld is under a 45 degree angle, and above the base plate it is in positive Z-direction. Even though there is the 45 degree angle at the weld toe, the MFL can be shown continuously for all altitudes along the S-axis, which is shown in Figure 5.18 and is equal to zero at the weld toe. Note that the background field has been subtracted from the magnetic flux density shown in Figure 5.18 to obtain the MFL line plots shown in Figure 5.19.
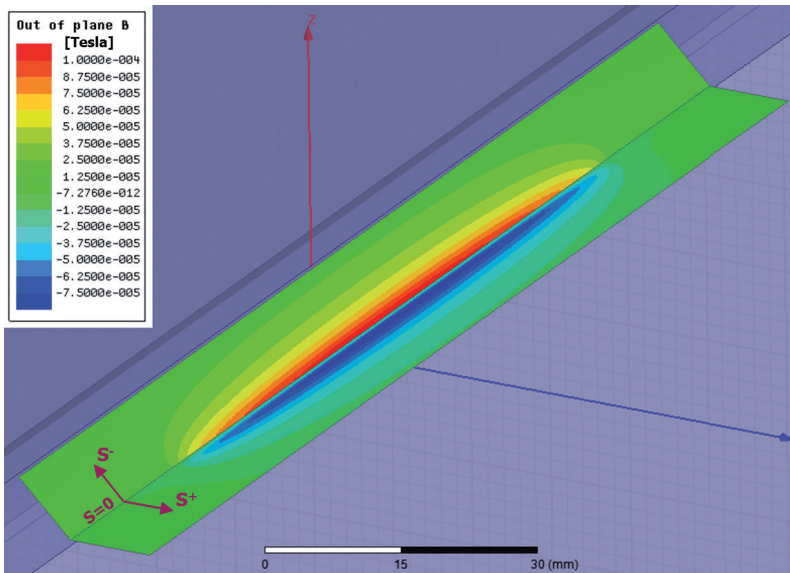
Figure 5.18: Out-of-plane magnetic flux density near weld toe crack at 1 mm altitude.

The signal strength can be obtained by subtracting the negative MFL peak above the plate from the positive MFL peak above the weld, which was done for all six curves along half of the crack. The resulting signal strengths along half of the crack are shown in Figure 5.20. The maximum signal strength of 155 µT occurs in the middle of the crack at X=0 and the minimum signal strength of 9 µT at the crack tip at X=50 mm. The slope of the signal strength over the X-coordinate approaches zero near the middle of the crack and reaches its peak value at the crack tip.
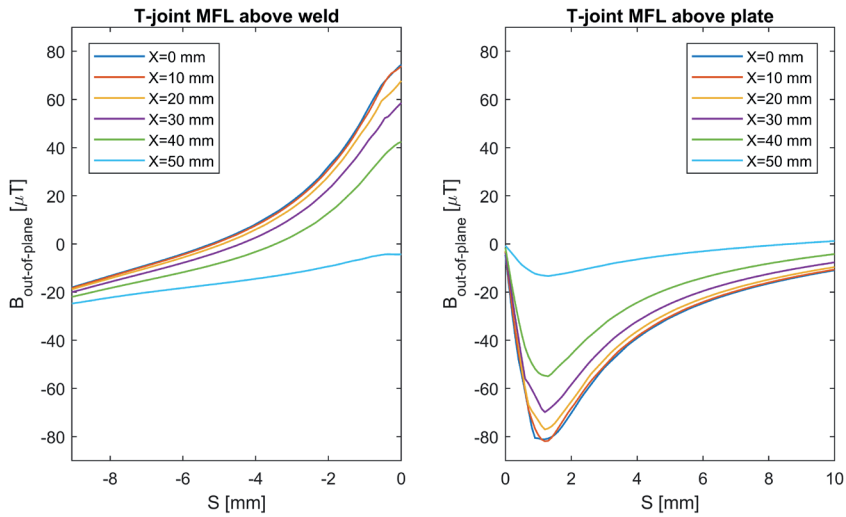
Figure 5.19: Magnetic Flux Leakage at an altitude of 1mm.
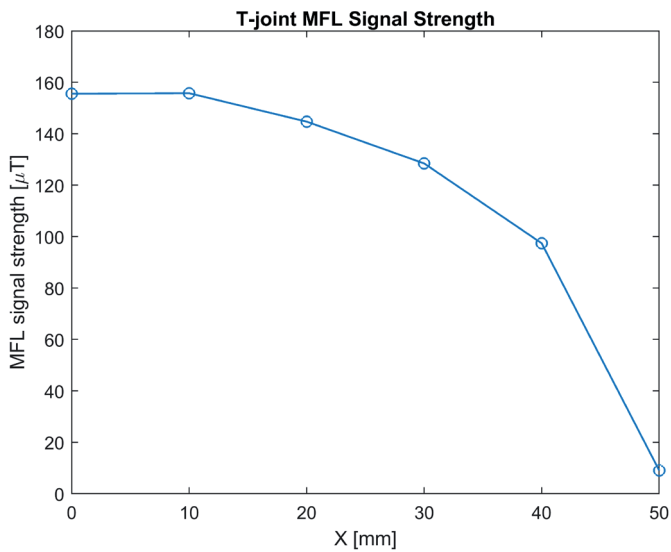
Figure 5.20: MFL signal strength along half of the crack's length.

5.4. Discussion

A numerical parametric study was performed to investigate the effects of altitude, Earth field orientation, crack opening, and crack length on the Earth-induced MFL near a through thickness center crack in a square plate. Furthermore, the Earth-induced MFL was studied numerically for a more complex geometry of a T-joint with a double-sided and not fully penetrated fillet weld with a through thickness crack along one weld toe. This section discusses some implications and limitations of the results of these studies.

The altitude is a critical design parameter when designing a crack monitoring system based on SMFL measurements. Preferably, a crack monitoring system performs well on different altitudes to account for surface roughness and corrosion protection layers. The results in Figure 5.9 implicate that with increasing altitude, the signal strength shows a rapid decay but the signal width increases linearly. The optimal altitude depends on what types of sensors are used. Highly sensitive magnetic sensors may be positioned further from the metal surface than less sensitive sensors. For the purpose of crack propagation monitoring, a grid of magnetic sensors is needed. The further the sensors are from the metal surface, the larger the grid spacing may be as the signal width increases. A decision is to be made to either use a few highly sensitive magnetic sensors at a relatively high altitude or a dense grid of less sensitive sensors very close to the metal surface.

The Earth field orientation is an environmental variable that one has no control over in reality and that affects the Earth-induced MFL significantly as shown in Figure 5.10 and Figure 5.11. The MFL signal strength is proportional to the effective background field, which is perpendicular to the crack orientation; hence, the MFL signal strength is proportional to the sine of the angle between the crack and the background field. Consequently, the Earth-induced MFL is zero when the Earth's magnetic field is in line with the crack. Fortunately, the total SMFL depends not only on the Earth-induced magnetization but also on the permanent magnetization and stress magnetization. Nevertheless, variability of the Earth field orientation can cause significant changes in real-time SMFL measurements that need to be accounted for when interpreting the measured signal.

Ship and offshore structures are cyclically loaded by waves, which can cause cracks to open and close. Some non-destructive evaluation methods are more reliable than others when crack opening displacements are very small. Research by Clark, Dover & Bond [7] reported a 100% reliability of crack length characterization, even for fully closed cracks, using Magnetic Particle Inspection (MPI), which relies on the same physical principle as MFL testing. On the other hand, a 100% reliability may not

be guaranteed without active magnetization as sensor noise levels could be higher than the calculated Earth-induced MFL signal strengths shown in Figure 5.13 for small crack opening displacements. A possible solution could be to measure the SMFL with a higher sampling rate than the load frequency so that the SMFL can be measured at maximum crack opening displacement.

The fatigue lifetime of a marine structure is directly related to the length and propagation rate of its fatigue cracks. Thus, the main objective of a crack monitoring system is to monitor the crack propagation. One way to monitor a propagating crack is to cover an area around the crack with a grid of magnetic sensors that can detect the spatial change of SMFL. The results in Figure 5.15 suggest another way of monitoring a propagating crack by measuring the gradual increase of the MFL signal strength in only one location. Previous experimental research found a linear relation between crack length and the peak-to-peak normal component of the magnetic flux density for a 18CrNiWA steel specimen under fatigue loading [8]. More research is needed to validate such relations to utilize them for crack length characterization using only one magnetic probe.

Fatigue cracks mostly initiate in stress concentration zones such as welded connections. For that reason, a double-sided and not fully penetrated fillet welded steel T-joint with a through thickness crack at one weld toe was analyzed to investigate its geometrical effects on the Earth-induced MFL. The results are very similar to that of the center cracked plate with a positive peak on one side of the crack, which is above the weld, and a negative peak on the other side. Therefore, sensors would need to be placed above the base plate as well as above the weld to measure the MFL on either side of the crack. Note that this study only focuses on the geometrical effects of welded connections, so the effects of different material characteristics and welding residual stresses [9, 10] are not taken into account in this study.

Now that several parameters have been investigated independently, combinations of certain parameter values can be made and analyzed numerically. As an example, the results of one combination are presented by taking realistic values for each parameter. This realistic case combines the geometry of the double-sided and not fully penetrated fillet weld with a through thickness crack along one weld toe with a crack length of 50 mm, a crack opening of 0.3 mm, an angle of 60 degrees between the Earth's magnetic field and the crack, and an altitude of 1 mm. The resulting out-of-plane magnetic flux density near the crack is shown in Figure 5.21 and the MFL signal strength along half of the crack's length is shown in Figure 5.22. The signal strengths are significantly reduced compared to the case from section 5.3.2, see Figure 5.20. Still, the Earth-induced MFL is strong enough to be measured with a Hall effect sensor,

which can have a sensitivity of approximately 1 μT, assuming that the grid of sensors is fine enough such that the peak values can be measured.
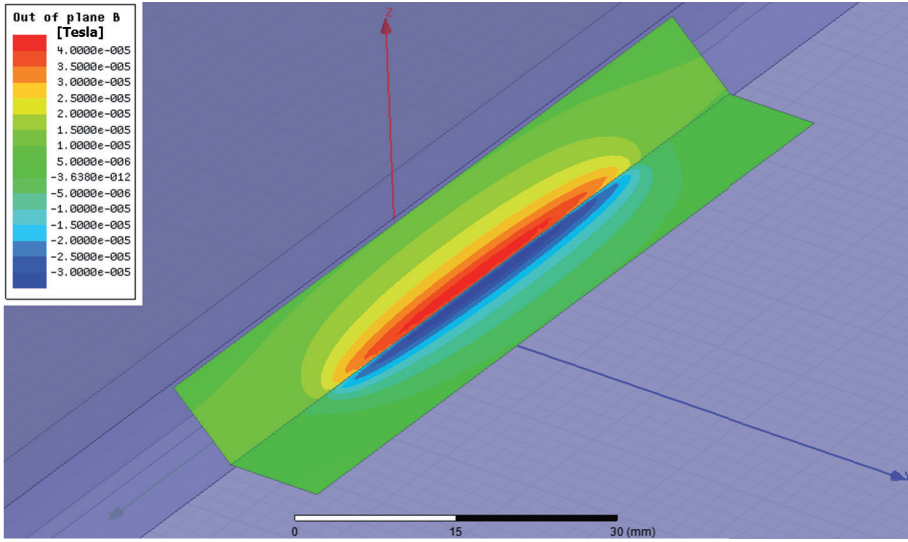
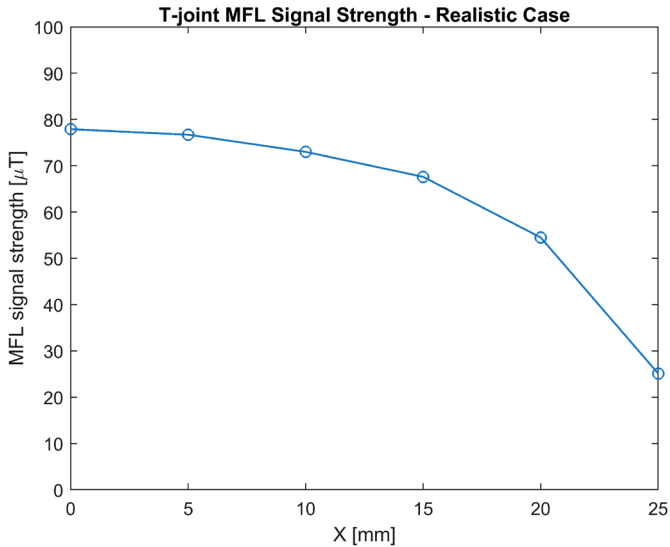Figure 5.21: Out-of-plane magnetic flux density near weld toe crack at 1 mm altitude – realistic case.

Figure 5.22: MFL signal strength along half of the crack's length – realistic case.

87

5.5. Conclusions

In this chapter, finite element simulation results of the Earth-induced Magnetic Flux Leakage (MFL) near cracks were analyzed with the aim to increase model complexity towards real fatigue cracks in ship and offshore structures. Ultimately, this research should lead to a novel passive magnetic crack monitoring system. The results from this study will help interpret measured data from such a system and perform more reliable crack characterization.

Four parameters and their effects on the Earth-induced MFL were studied that the envisaged crack monitoring system would need to cope with: altitude, Earth field orientation, crack opening, and crack length. Numerical results show that for a center cracked plate with a through thickness crack, increasing the altitude decreases the signal strength as a power function while the signal width increases linearly. For a crack monitoring system, sensors will need to be placed at an optimal altitude, balancing between the sensor sensitivity and accompanied costs, and the amount of sensors required for accurate crack length characterization. Crack opening and closing occurs with approximately the wave frequency, which then dictates the required sensor sampling rate so that the maximum signal strength can be measured at maximum crack opening displacement. The numerical results also showed that the signal strength gradually increases in the middle of the crack when the crack propagates, which creates opportunities to determine the crack length even when no sensors are present near the crack tips. Lastly, the Earth field orientation has shown to have a significant impact on the induced MFL as the MFL is proportional to the effective background field, which is in-plane and perpendicular to the crack orientation. As the orientation of ships in the Earth's magnetic field can change continuously, a correction on the measured data may be needed to ensure that for example the change in measurements is not falsely attributed to crack propagation.

Geometrical effects of a common welded joint with a crack along the weld toe on the Earth-induced MFL were studied as well. Numerical results show that some magnetic flux flows through the stiffener plate, resulting in a reduced MFL. Still, a through thickness crack can clearly be characterized when looking at the out-of-plane magnetic flux density at an altitude of 1 mm, even for a realistic case with a crack length of 50 mm, a crack opening of 0.3 mm, and an Earth field orientation of 60 degrees with respect to the crack. The main challenge with applying a crack monitoring system based on SMFL measurements on a weld toe crack is that sensors need to be placed on either side of the crack, so above the weld as well. In reality, the weld material has different magnetic properties than the base material and its geometry is not always constant over the cross section and length of the weld. More

research is needed to investigate the implications of these extra uncertainties when analyzing MFL signals near welds.

5.6. References

[1]   Van der Horst MP, Kaminski ML, Puik E. Methods for Sensing and Monitoring Fatigue Cracks and Their Applicability for Marine Structures. Proc. Int. Offshore Polar Eng. Conf., Anchorage, Alaska: 2013, p. 455–62.

[2]   Van der Horst MP, Kaminski ML. Slit Induced Self Magnetic Flux Leakage in a Square Steel Plate. Proc. Int. Offshore Polar Eng. Conf., Sapporo, Japan: 2018.

[3]   Bozorth RM, Williams HJ. Effect of Small Stresses on Magnetic Properties. Rev Mod Phys 1945;17:72–80.

[4]   Atherton DL, Jiles DC. Effects of stress on magnetization. NDT Int 1986;19:15–9. doi:10.1016/0308-9126(86)90135-5.

[5]   Jiles DC, Devine MK. The law of approach as a means of modelling the magnetomechanical effect. J Magn Magn Mater 1995;140–144:1881–2. doi:10.1016/0304-8853(94)00928-7.

[6]   Van Der Horst MP, Kaminski ML. Magnetic Properties of Structural Steels for Simulation of Crack Monitoring by Finite Element Method. Manuscr under Rev 2018.

[7]   Clark R, Dover WD, Bond LJ. The effect of crack closure on the reliability of NDT predictions of crack size. NDT Int 1987;20:269–75. doi:10.1016/0308-9126(87)90444-5.

[8]   Dong L, Xu B, Dong S, Chen Q, Dan W. Monitoring fatigue crack propagation of ferromagnetic materials with spontaneous abnormal magnetic signals. Int J Fatigue 2008;30:1599–605. doi:10.1016/j.ijfatigue.2007.11.009.

[9]   Luming L, Songling H, Xiaofeng W, Keren S, Su W. Magnetic field abnormality caused by welding residual stress. J Magn Magn Mater 2003;261:385–91. doi:10.1016/S0304-8853(02)01488-9.

[10]   Roskosz M. Metal magnetic memory testing of welded joints of ferritic and austenitic steels. NDT E Int 2011;44:305–10. doi:10.1016/j.ndteint.2011.01.008.

5

6

Effect of Stress-Induced Magnetization on Crack Monitoring by Self Magnetic Flux Leakage Method

Abstract

Wireless crack monitoring on ship and offshore structures based on Self Magnetic Flux Leakage (SMFL) measurements is a promising method to guarantee the structural integrity in a more effective way, leading to reduced operational costs and increased safety. For accurate crack sizing, the SMFL measurements must be interpreted correctly, also during cyclic loading. Not much research has been done that focuses on the effect of high cyclic stresses on the magnetization of ferromagnetic steels in weak magnetic fields. The aim of the research presented in this chapter is to investigate the effect of stress-induced magnetization on the SMFL in the stress concentration zone of a structural steel plate, and its implications for crack monitoring by the SMFL method. By means of an experiment, measured stress magnetization curves were obtained in a grid of points around an elliptical hole in a steel plate that is cyclically loaded up to the design yield stress. The results show that the stress-induced magnetization causes a maximum variation of the measured signal of 25 µT, which is fully reversible. It is concluded that, depending on the application, this stress-induced variation may need to be taken into account for the interpretation of the measured signals by a crack monitoring system using the SMFL method.

Keywords

Crack monitoring; self magnetic flux leakage; stress magnetization; ferromagnetic steel; cyclic loading; stress concentration zone.

6.1. Introduction

For accurate sizing of a crack using the Self Magnetic Flux Leakage (SMFL) method, measurements must be interpreted correctly. Earlier research gave insight in the contributions of Earth-induced magnetization and permanent magnetization to the SMFL signals near a crack in a structural steel plate that is unloaded [2, 3]. When applying fatigue loads on a cracked specimen, the SMFL will change due to crack opening [3] and stress-induced magnetization. Much research has been done on stress-induced magnetization, which is caused by the magnetomechanical effect [4–10]. However, most studies focus on the effect of small and static stresses for large applied fields. For passive magnetic crack monitoring, on the other hand, it is important to study and quantify the effect of large and cyclic stresses in weak magnetic fields. Therefore, the objective of the research presented in this chapter is to investigate the effect of stress-induced magnetization on the SMFL in the stress concentration zone of a structural steel plate, and its implications for crack monitoring by the SMFL method.

An experimental method to measure the effect of stress-induced magnetization on the SMFL is described in the next section and the experimental results are presented in section 6.3. The Earth-induced magnetization and the stress distribution for the experimental specimen are numerically simulated by the finite element method in section 6.4. This section also presents a theoretical framework to simulate the stress-induced magnetization for a qualitative comparison with the experimental results. Finally, all the results are discussed in section 6.5 and the conclusions are presented in section 6.6.

6.2. Method

6.2.1. Test Specimen

An FeE235 structural steel plate is used as test specimen for the conducted experiment. The plate has a width of 70 mm and a thickness of 5 mm and has an elliptical hole in the middle of 10 by 3 mm, see Figure 6.1. The dimensions of the defect are chosen such that it creates a significant stress concentration zone while having a large enough width so that the opening of the hole caused by applied tension is negligible. The length of the specimen is sufficient to clamp it in the MTS fatigue testing machine, see Figure 6.2, and have sufficient length left to ensure a uniform stress distribution in the middle of the plate. The MTS fatigue testing machine can apply loads in axial direction of up to 350 kN with a frequency of up to 20 Hz.
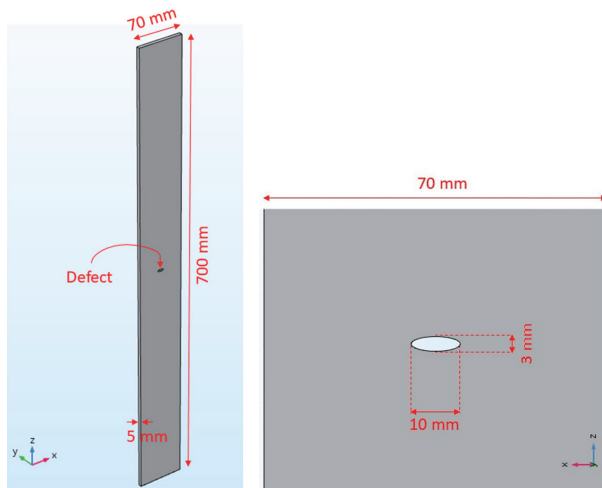
Figure 6.1: FeE235 steel specimen with dimensions.

Figure 6.2: Specimen while clamped in the MTS fatigue testing machine.

6.2.2. Experiment 1

The fatigue machine is programmed to apply a linearly increasing load from 0 kN to 82.25 kN in 40 seconds which then decreases again to 0 kN with the same rate. This load cycle is repeated two more times resulting in the force-time diagram shown

in Figure 6.3. A tensile load of 82.25 kN results in a far field stress of 235 MPa, which is the design yield limit.
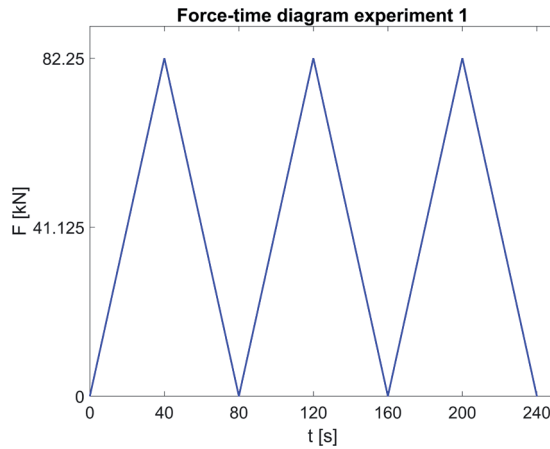
Figure 6.3: Load path Experiment 1.

While the specimen is loaded, magnetic measurements are taken near the plate surface using a single axis magnetometer with 1 µT sensitivity [11] in out-of-plane direction, which is the Y-direction in this case, see Figure 6.4. The Hall probe of the magnetometer is kept at a constant altitude of 1 mm from the plate surface and takes measurements with a sampling rate of 5 Hz. These continuous measurement cycles are repeated in a grid of 14 locations around the elliptical hole as shown in Figure 6.5.

Figure 6.4: Setup for magnetic measurements Experiment 1.
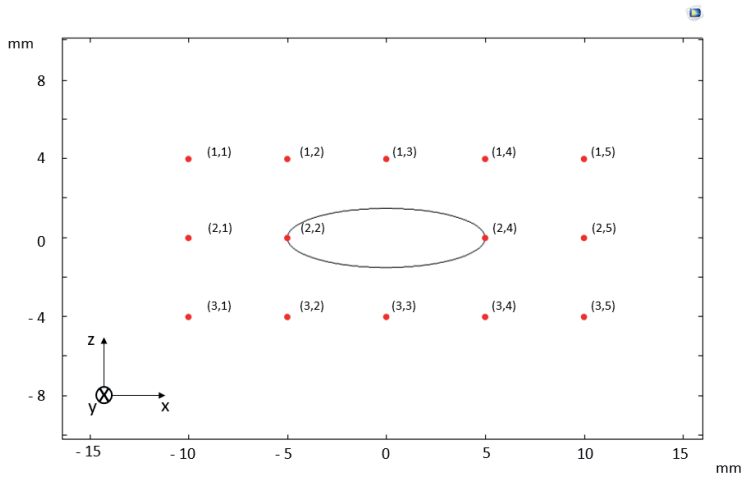
Figure 6.5: Measurement grid around elliptical hole.

6.2.3. Experiment 2

To investigate whether local plasticity plays a role in Experiment 1, a similar experiment is conducted where measurements are taken in the elastic region away from the elliptical hole. The same test specimen is used but with an extra row of five measurement points 50 mm above the elliptical hole, see Figure 6.6. The points are numbered from left to right as (0,1) to (0,5).

Figure 6.6: Test specimen with extra row of five measurement points 50 mm above elliptical hole.

The same load path is applied but with a minimum load of 3 kN to avoid any overshoot into compressive forces that could lead to unwanted bending stresses and a maximum load of 77 kN to be certain that no plasticity occurs around the extra row of measurement points. The resulting force-time diagram of Experiment 2 can be seen in Figure 6.7.

The same setup is used with the single axis magnetometer taking measurements in Y-direction with a sampling rate of 5 Hz at the five measurement points consecutively and with an altitude of 1 mm from the plate surface, as shown in Figure 6.8.
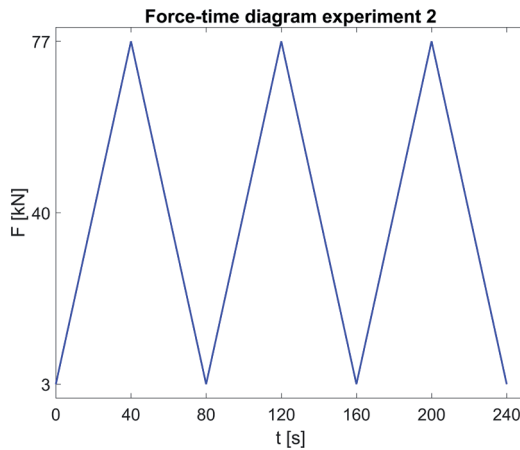
Figure 6.7: Load path Experiment 2.

Figure 6.8: Setup for magnetic measurements Experiment 2.

6.3. Experimental Results

6.3.1. Results Experiment 1

Before starting the experiment, the background field was measured. The resulting background field in X, Y, and Z-direction can be found in Table 6.1.

Direction	B [µT]
X	-10
Y	-11
Z	-20

Table 6.1: Background field before Experiment 1.

The measured time traces of the magnetic flux density in Y-direction are shown in Figure 6.9. The chart on the left shows the time traces for row 1 of the measurement grid, the middle chart for row 2, and the chart on the right for row 3.
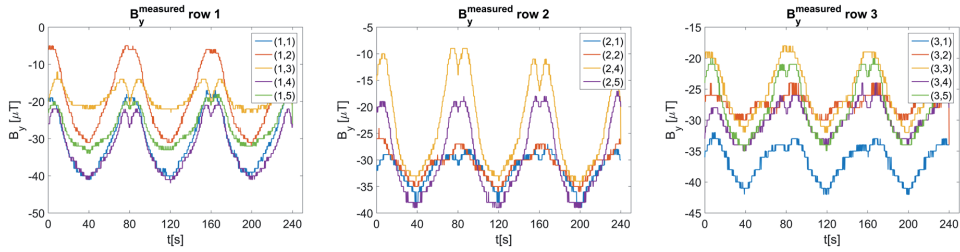
Figure 6.9: Raw measurement data Experiment 1.

The measured magnetic flux density is a summation of background field, Earth-induced field, permanent field, and stress-induced field, so it reads

$$B_Y^{measured} = B_Y^{BG} + B_Y^{ind} + B_Y^{per} + B_Y^{\sigma}. \tag{6.1}$$

The background field, Earth-induced field, and permanent field are assumed to be constant in time during loading as changes in environment, plate geometry, magnetic material properties, and coupling between stress-induced magnetization and permanent magnetization are assumed negligible. Therefore, the only change in magnetic flux density during loading is attributed to the stress-induced magnetic flux density. The stress-induced magnetic flux density can then be calculated by subtracting the measured magnetic flux density at $t = 0$ from the entire time series as follows:

$$B_Y^{\sigma}(t) = B_Y^{measured}(t) - B_Y^{measured}(t = 0). \tag{6.2}$$

The resulting time traces for the stress-induced magnetic flux density in Y-direction are shown in Figure 6.10. Note that a moving average filter with a span of 15 data points (i.e. 3 s) is applied on the raw data to reduce perturbations due to the discrete sensor output.
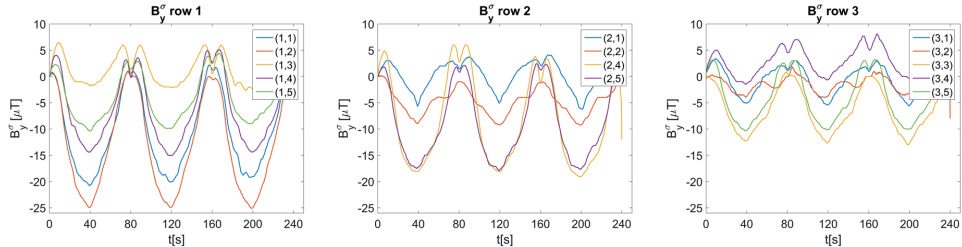
Figure 6.10: Moving average filtered stress-induced B_Y for rows 1-3.

The three load cycles can be subdivided into six periods: three periods with increasing load and three periods with decreasing load. In Figure 6.11, the results for these six periods are plotted as function of the applied load for point (1,2), which showed the highest maximum stress-induced magnetic flux density. The beginning and end of all curves coincide with each other but the path in between is different for periods with increasing load than for periods with decreasing load. Figures 6.12, 6.13, and 6.14 show the average curves for periods 1, 3, and 5 as "Increasing F" and for periods 2, 4, and 6 as "Decreasing F" for rows 1, 2, and 3 respectively. In each measurement point, a small difference can be observed in the stress-induced magnetization curve for increasing load versus decreasing load. Most importantly, the stress-induced magnetization increases with increasing load in each measurement point but the magnitude varies between measurement points.
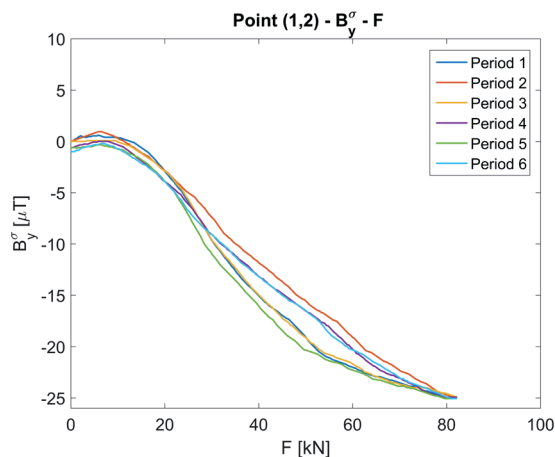
Figure 6.11: Stress-induced B_Y versus applied load for point (1,2).
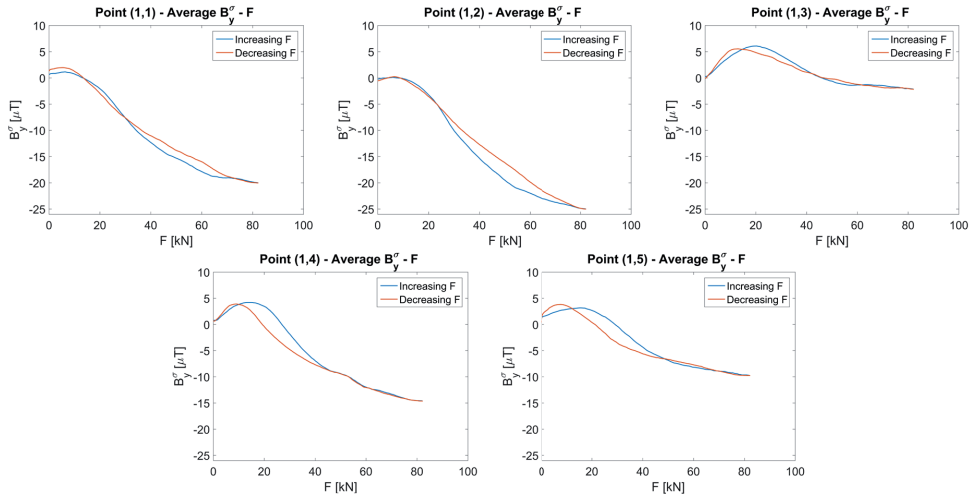
Figure 6.12: Averaged stress-induced B_Y versus applied load for row 1.
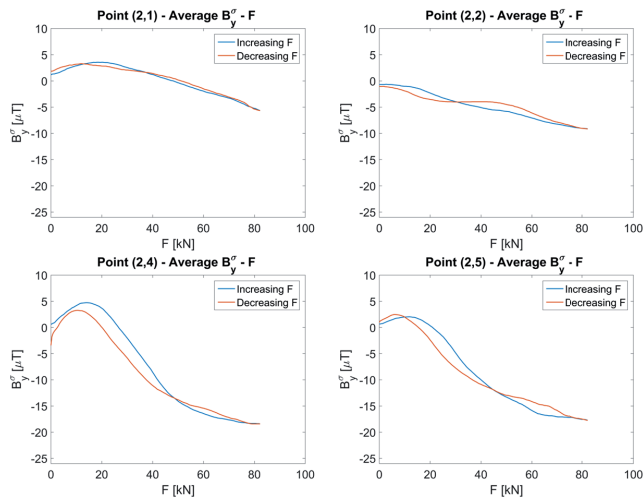
Figure 6.13: Averaged stress-induced B_Y versus applied load for row 2.
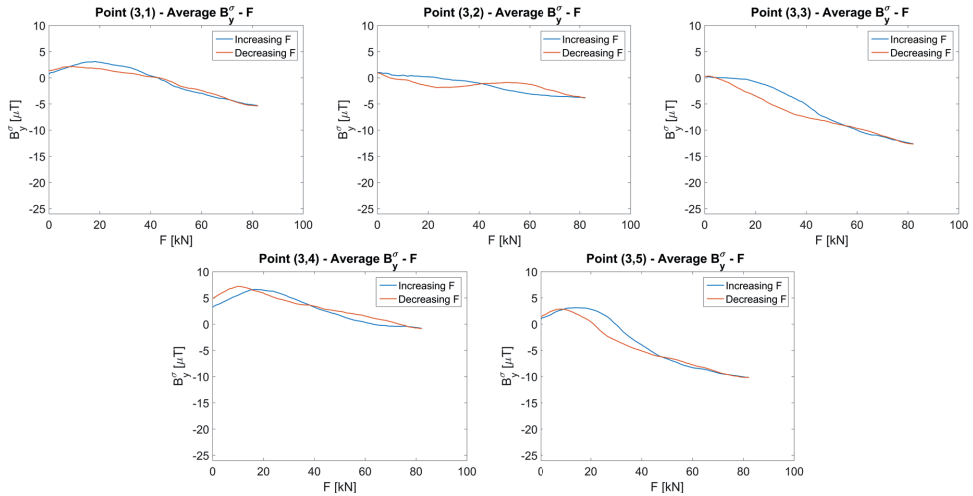
Figure 6.14: Averaged stress-induced B_Y versus applied load for row 3.

6.3.2. Results Experiment 2

Experiment 2 was conducted a week after experiment 1, so the background field was measured again. The resulting background field in X, Y, and Z-direction can be found in Table 6.2.

Direction	B [µT]
X	-5
Y	-14
Z	-18

Table 6.2: Background field before Experiment 2.

Post-processing of the measured data for Experiment 2 is done in the same manner as for Experiment 1. The measured time traces of the magnetic flux density in Y-direction are shown in Figure 6.15 and those for the stress-induced magnetic flux density in Y-direction, calculated according to equation 6.2, are shown in Figure 6.16. Again, a moving average filter with a span of 15 is applied to the raw data to obtain smooth curves in Figure 6.16. The average stress-induced magnetic flux density in Y-direction for increasing load and decreasing load is plotted against the applied load in Figure 6.17 for all five measurement points in row 0.
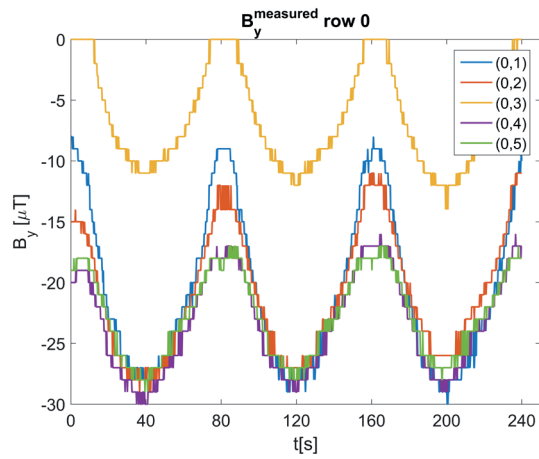
Figure 6.15: Raw measurement data Experiment 2.
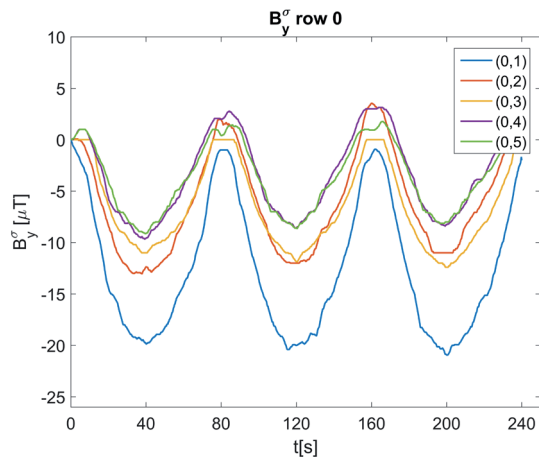
Figure 6.16: Moving average filtered stress-induced B_Y for row 0.
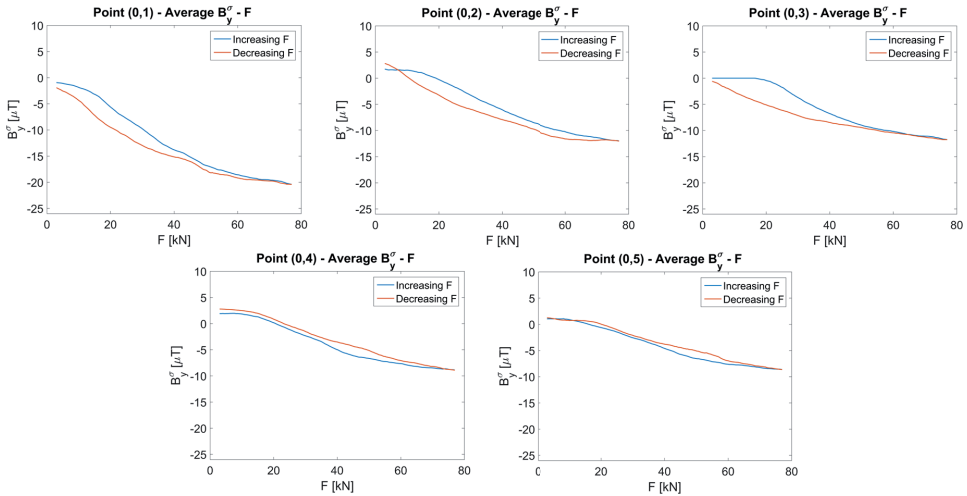
Figure 6.17: Averaged stress-induced B_Y versus applied load for row 0.

6.4. Numerical Simulation

6.4.1. Magnetic FE Model

The Earth-induced magnetization from equation 6.1 can be modeled with a linear magneto-static finite element model using the software package COMSOL Multiphysics. The same steel is used as for the specimen from Chapter 4, so the material is modeled linearly with a relative permeability of 225. The geometry from Figure 6.1 is modeled with a vacuum box of 15x15x15 m around the plate as model domain. On the domain edges, boundary conditions are applied such that a homogeneous background field is generated with the measured values from Table 6.1. The model is meshed using tetrahedral elements and results are obtained at the plate's surface around the elliptical hole. The results for the magnetic flux density in Y-direction are shown in Figure 6.18 together with the measurement grid. Note that this model only considers the induced magnetization caused by the background field in combination with the plate's ferromagnetic properties.
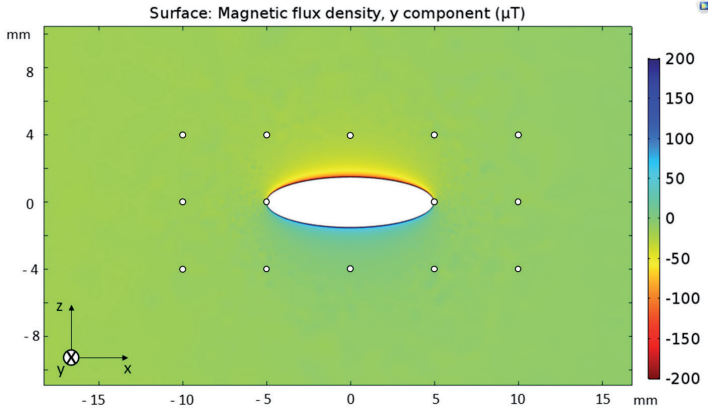
Figure 6.18: FE results for B_Y around the elliptical hole at the plate surface with grid points.

6.4.2. Mechanical FE Model

To interpret the results from section 6.3.1, the stress distribution around the elliptical hole is needed. To that end, a mechanical finite element model is made of the same steel plate from Figure 6.1 using the software package COMSOL Multiphysics. The predefined material "Structural Steel" is used, which is linear elastic with an Elasticity Modulus of 200 GPa. The plate is constrained on the lower boundary and a force per unit area of 220 MPa is applied on the upper boundary of the plate. The plate is meshed using tetrahedral elements. The resulting von Mises stress distribution at the plate's surface around the elliptical hole is shown in Figure 6.19 together with the measurement grid.
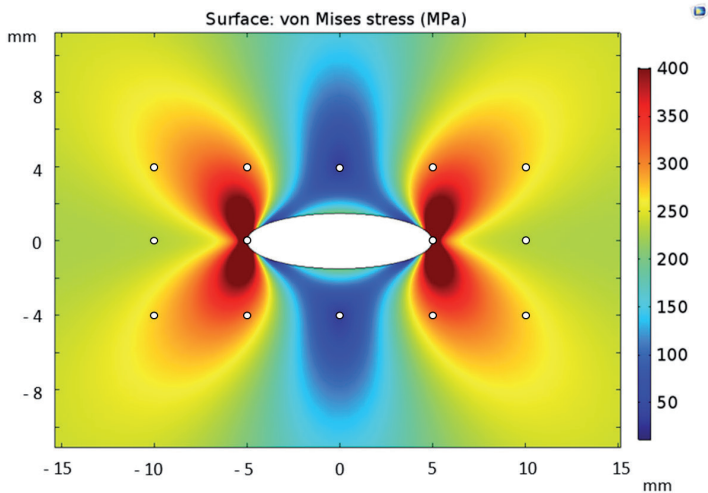
Figure 6.19: FE results for von Mises stress distribution at the plate surface with grid points.

6.4.3. Magnetomechanical Model

The magnetomechanical effect [6] can be implemented in the original theory of ferromagnetic hysteresis by Jiles & Atherton [12] through the effective field description H_e with the magnetostriction λ, which is defined as the strain due to an applied magnetic field. Note that this description of the effective field is done under the assumption that the magnetostriction is very small and the applied field is in the same direction as the direction in which the stress is applied. The effective field description reads

$$H_e = H_a + \alpha M + H_\sigma, \tag{6.3}$$

where α is a field parameter representing the inter domain coupling,

and

$$H_\sigma = \frac{3}{2\mu_0} \sigma \frac{\partial \lambda}{\partial M}. \tag{6.4}$$

The same differential equation for the effective field as proposed in [12] can be applied, which reads

$$(M - M_a) = -k\delta \frac{dM}{dH_e}, \tag{6.5}$$

where k is the pinning constant and δ is a directional parameter, which takes the value 1 for increasing fields and -1 for decreasing fields. The anhysteretic M_a is a function of the effective field, which is also described in [12] and reads

$$M_a(H_e) = M_s \cdot L(H_e/a), \tag{6.6}$$

where L is the Langevin function, $L(x) = \coth(x) - 1/x$, M_s the saturation magnetization, and a a constant form factor.

For a constant field H_a and varying stress, differential equation 6.5 can be rewritten, following the notation by Naus [7], as follows:

$$\frac{dM}{d\sigma} = -\frac{A_2(M,\sigma)(M-M_a)}{k\delta + A_1(M,\sigma)(M-M_a)}, \tag{6.7}$$

where

$$A_1(M,\sigma) = \frac{\partial H_e}{\partial M} = \alpha + \frac{3\sigma}{2\mu_0} \cdot \frac{\partial^2 \lambda}{\partial M^2}, \tag{6.8}$$

and

$$A_2(M,\sigma) = \frac{3\sigma}{2\mu_0}\left(\frac{\partial\lambda}{\partial M} + \sigma\frac{\partial^2\lambda}{\partial M\partial\sigma}\right). \tag{6.9}$$

This differential equation can describe the magnetization for a constant field and varying stress. It is stressed in [7] that this description becomes equivalent to the original formalism of magnetomechanics described in [7, 13, 14] for zero or constant stress. Naus also extended the model to include the reversible contribution of the magnetization M_r. The modified differential equation for varying stress and constant field reads

$$\frac{dM}{d\sigma} = -\frac{A_2(M,\sigma)\left(M-M_a-ck\delta\frac{dM_a}{dH_e}\right)}{k\delta+A_1(M,\sigma)\left(M-M_a-ck\delta\frac{dM_a}{dH_e}\right)}, \tag{6.10}$$

where c is a constant that represents the reversible wall motion component. Following [6], the stress dependent magnetostriction is described by a double series expansion as follows:

$$\lambda(M,\sigma) = \sum_{i=0}^{\infty}\gamma_i(\sigma)\cdot M^{2i}, \tag{6.11}$$

where

$$\gamma_i(\sigma) = \gamma_i(0) + \sum_{n=1}^{\infty}\frac{\sigma^n}{n!}\gamma_i^{[n]}(0). \tag{6.12}$$

As in [6], this series is implemented up to $i=2$ and $n=1$. Following [7], $\gamma_1^{[0]} = 3\cdot10^{-18}\,A^{-2}M^2$ and all other $\gamma_i^{[n]} = 0$. The differential equation can now be written as follows:

$$\frac{dM}{d\sigma} = -\frac{\frac{3\gamma_1^{[0]}}{\mu_0}M\left(M-M_a-ck\delta\frac{dM_a}{dH_e}\right)}{k\delta+\left(\alpha+\frac{3\gamma_1^{[0]}}{\mu_0}\sigma\right)\left(M-M_a-ck\delta\frac{dM_a}{dH_e}\right)}. \tag{6.13}$$

To solve this differential equation, five hysteresis parameters are needed. These parameters are determined in [14] for several different materials by fitting the modeled hysteresis curve with a measured hysteresis curve. In the experiment described in this paper, FeE235 steel was used, which has a maximum carbon content of 0.22 mass%. Therefore, the calculated model parameters for Fe 0.2 mass% C from [14] are used to solve equation 6.13. The chosen values for the five hysteresis parameters are presented in Table 6.3.

Parameter	Value	Unit	Represents
M_s	$1.6 \cdot 10^6$	[A/m]	Saturation magnetization
a	1085	[A/m]	Form factor for the anhysteretic curve
k	320	[A/m]	Pinning constant
α	$2 \cdot 10^{-3}$	[-]	Inter domain coupling parameter
c	0.3	[-]	Reversible wall motion component

Table 6.3: Model hysteresis parameters for Fe 0.2 mass% C [14].

The effective field description described by differential equation 6.13 is solved numerically with the Euler forward method using the parameters from Table 6.3. The initial magnetization is chosen arbitrarily as 30% of the saturation magnetization and the applied field is chosen according to the measured background field in Table 6.1 as 20 A/m. The stress is varied from zero to 235 MPa and back to zero, which is repeated two more cycles just as in the experiment. The results are presented in Figure 6.20.
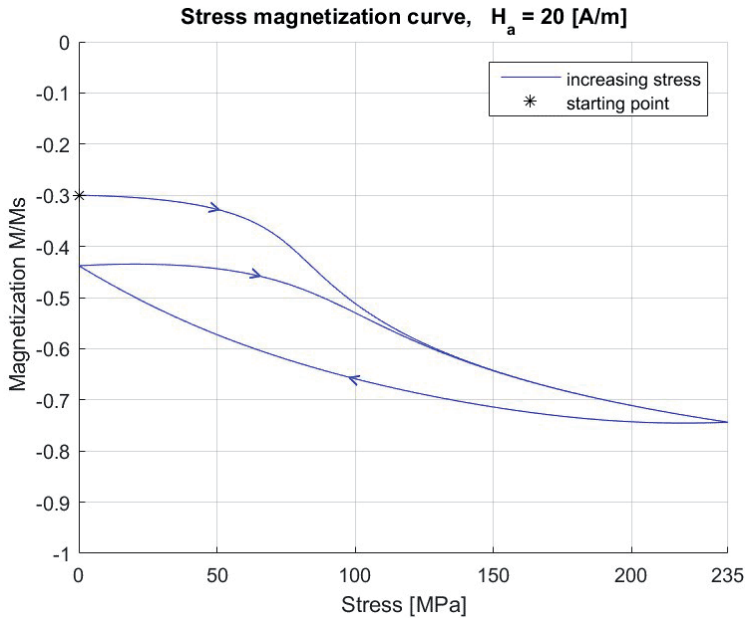

Figure 6.20: Model results for the effective field description.

6.5. Discussion

The experimental results show a clear instantaneous magnetic response to the applied cyclic tensile load on the specimen. Equation 6.1 is used to decouple the different sources of magnetization that contribute to the measured signal. This

decoupling equation is intrinsically incorrect as stress magnetization is dependent on the total magnetization in the material, see equation 6.4. Also, the stress magnetization generally has a reversible and irreversible component. The irreversible stress magnetization should be captured in the permanent magnetization, which means they are coupled as well. Nevertheless, equation 6.2 can still be applied to extract the stress-induced B_Y from the measurements as long as only short term effects are considered. The validity of this approach is supported by the results in Figures 6.12 to 6.14 as there are no irreversible effects visible in the stress-induced magnetization curves during the three load cycles for any of the measurement points. This finding is in accordance with the work of other researchers who stated that the magnetomechanical loop tends to a stable curve after multiple cyclic loads [15], so the reversible magnetization becomes more dominant during subsequent stress cycles. Note that the specimen already experienced a few load cycles before the first magnetic measurements were taken.

The stress magnetization measurements for different locations may not be directly compared as the stress magnetization is dependent on the total magnetization, which is most likely non-uniform especially around the machined elliptical defect. Still, it can be seen that the stress magnetization at high stress concentration areas such as location (1,2) is generally much higher than where the stress is low such as location (1,3). For all the measurement points, the stress magnetization curves for increasing load are slightly different from those for decreasing load, but the way they differ from each other is not consistent for each of the measurement locations, see Figures 6.12 to 6.14. For most of the locations, the measured time traces show an unexpected peak when the applied load approaches zero, see Figures 6.9 and 6.10. These peaks are most likely caused by a small overshoot of the applied load into the compressive region causing some bending stresses in the plate. This explanation is confirmed by the absence of these additional peaks for Experiment 2 where the minimum load was 3 kN in tension, see Figures 6.15 and 6.16. Local plasticity near the elliptical hole does not seem to have a large impact on the stress magnetization for this test plate in the given environment as the results from Experiment 2 in the elastic region are very similar to the results of Experiment 1. The fact that each of the measurement points in Experiment 2 show different values for the stress-induced magnetic flux density supports the hypothesis that the magnetization in the plate is highly non-uniform because the stresses there are uniform.

The magnetic FE simulation in section 6.4.1 gives insight in the Earth-induced Magnetic Flux Leakage around the elliptical hole. A direct comparison with the measurements cannot be made because the permanent magnetization in the steel plate is unknown. The main learning from the results shown in Figure 6.18 is that the

spatial variation of the Earth-induced magnetic flux density is very small near the measurement points, which gives more confidence in the quality of the experimental data obtained in this study. The mechanical FE simulation in section 6.4.2 gives insight in the distribution of stresses around the elliptical defect. Figure 6.19 shows that the largest stresses are very concentrated near the tips of the elliptical hole and the smallest stresses occur in the shadow areas above and underneath the elliptical hole.

Finally, the numerical simulation of the magnetomechanical effect may be used for a qualitative comparison with the experimental results. Since the magnetomechanical model describes the magnetization in the steel plate and the measurements were done at an altitude of 1 mm from the plate surface, a quantitative comparison cannot be made. Also, the permanent magnetization in the plate is unknown and the chosen values for the hysteresis parameters from Table 6.3 and the magnetostriction may not be accurate for this particular steel plate. Nevertheless, the model results in a similar shape of the stress magnetization curve as the experimental results. After just one stress cycle, the calculated stress magnetization curve in Figure 6.20 enters a stable loop, which corresponds with the experimental results.

6.6. Conclusions

The effect of the stress-induced magnetization on the Self Magnetic Flux Leakage (SMFL) near a stress concentration zone has been investigated experimentally and, as far as possible, numerically. The maximum change in measured SMFL due to applied tensile stress was approximately 25 µT near an elliptical hole in a 5 mm thick steel plate in the Earth's magnetic field. For a fatigue crack, the effect of the stress-induced magnetization may be larger as the stress concentration factor is even higher. The measured stress-induced signal during cyclic loading showed a closed loop, so the irreversible magnetization was negligible. The expectation was that the stress-induced signals would be to some extent symmetric around the elliptical hole as loading and geometry, and therefore stresses, are symmetric as well. Instead, the distribution of the stress-induced magnetization appeared very irregular, which can be attributed to the inhomogeneous magnetization. From equation 6.4, it follows that the stress magnetization is dependent on the magnetization, magnetostriction, and stress. Local plasticity did not seem to have a significant effect on the stress-induced magnetization as experimental results in the elastic region showed similar magnetization curves in the same order of magnitude. A numerical simulation of the magnetomechanical effect based on a theoretical framework resulted in a similar stress magnetization curve as the ones that were measured.

For crack monitoring based on the SMFL method, the stress-induced magnetization may have a significant effect on how the measured signals should be interpreted, depending on the application. A maximum change in the SMFL of 25 µT due to stress can probably be neglected when monitoring a through thickness crack with a length of at least 50 mm in a thick steel plate that is part of a large structure, but the stress-induced magnetization may be more significant near a real fatigue crack as opposed to the experimental case presented here. For monitoring short elliptical surface cracks, the stress-induced magnetization probably has a significant effect on the measured SMFL signals near the defect. Therefore, the stress-induced magnetization should be taken into account for the interpretation of the measured signals and sizing of the crack. To this end, more research is necessary to gain better understanding of the interaction between high local stresses at a crack tip and the magnetization of ferromagnetic steel in weak background fields.

6.7. References

[1]   Van der Horst MP, Kaminski ML. Slit Induced Self Magnetic Flux Leakage in a Square Steel Plate. Proc. Int. Offshore Polar Eng. Conf., Sapporo, Japan: 2018.

[2]   Van Der Horst MP, Kaminski ML. Magnetic Properties of Structural Steels for Simulation of Crack Monitoring by Finite Element Method. Manuscr under Rev 2018.

[3]   Van der Horst MP, Kaminski ML. Simulation and Analysis of Earth-Induced Magnetic Flux Leakage for Monitoring Cracks in Ship and Offshore Structures. Manuscr under Rev 2018.

[4]   Craik DJ, Wood MJ. Magnetization changes induced by stress in a constant applied field. J Phys D Appl Phys 1970;3:1009–16. doi:10.1088/0022-3727/3/7/303.

[5]   Atherton DL, Jiles DC. Effects of stress on magnetization. NDT Int 1986;19:15–9. doi:10.1016/0308-9126(86)90135-5.

[6]   Jiles DC. Theory of the magnetomechanical effect. J Phys D Appl Phys 1995;28:1537–46.

[7]   Naus HWL. Theoretical developments in magnetomechanics. IEEE Trans Magn 2011;47:2155–62.

[8]   Jiles DC, Devine MK. The law of approach as a means of modelling the magnetomechanical effect. J Magn Magn Mater 1995;140–144:1881–2. doi:10.1016/0304-8853(94)00928-7.

[9]   Li L, Jiles DC. Modified Law of Approach for the Magnetomechanical Model: Application of the Rayleigh Law to Stress. IEEE Trans Magn 2003;39:3037–9. doi:10.1109/TMAG.2003.815882.

[10]   Jiles DC, Li L. A new approach to modeling the magnetomechanical effect. J Appl Phys 2004;95:7058–60. doi:10.1063/1.1687200.

[11]   Wuntronic. Wuntronic Tesla Meter KOSHAVA-USB n.d. http://www.wuntronic.de/en/USB-Tesla-Meter-Gauss-Meter-with-USB.html (accessed March 27, 2018).

[12]   Jiles DC, Atherton DL. Theory of ferromagnetic hysteresis (invited). J Appl Phys 1984;55:2115–20. doi:10.1063/1.333582.

[13]   Sablik MJ, Jiles DC. Coupled Magnetoelastic Theory of Magnetic and Magnetostrictive Hysteresis. IEEE Trans Magn 1993;29:2113–23. doi:10.1109/20.221036.

[14]   Jiles DC, Thoelke JB, Devine MK. Numerical Determination of Hysteresis Parameters for the Modeling of Magnetic Properties Using the Theory of Ferromagnetic Hysteresis. IEEE Trans Magn 1992;28:27–35. doi:10.1109/20.119813.

[15]   Shi P, Jin K, Zheng X. A general nonlinear magnetomechanical model for ferromagnetic materials under a constant weak magnetic field. J Appl Phys 2016;119:145103. doi:10.1063/1.4945766.
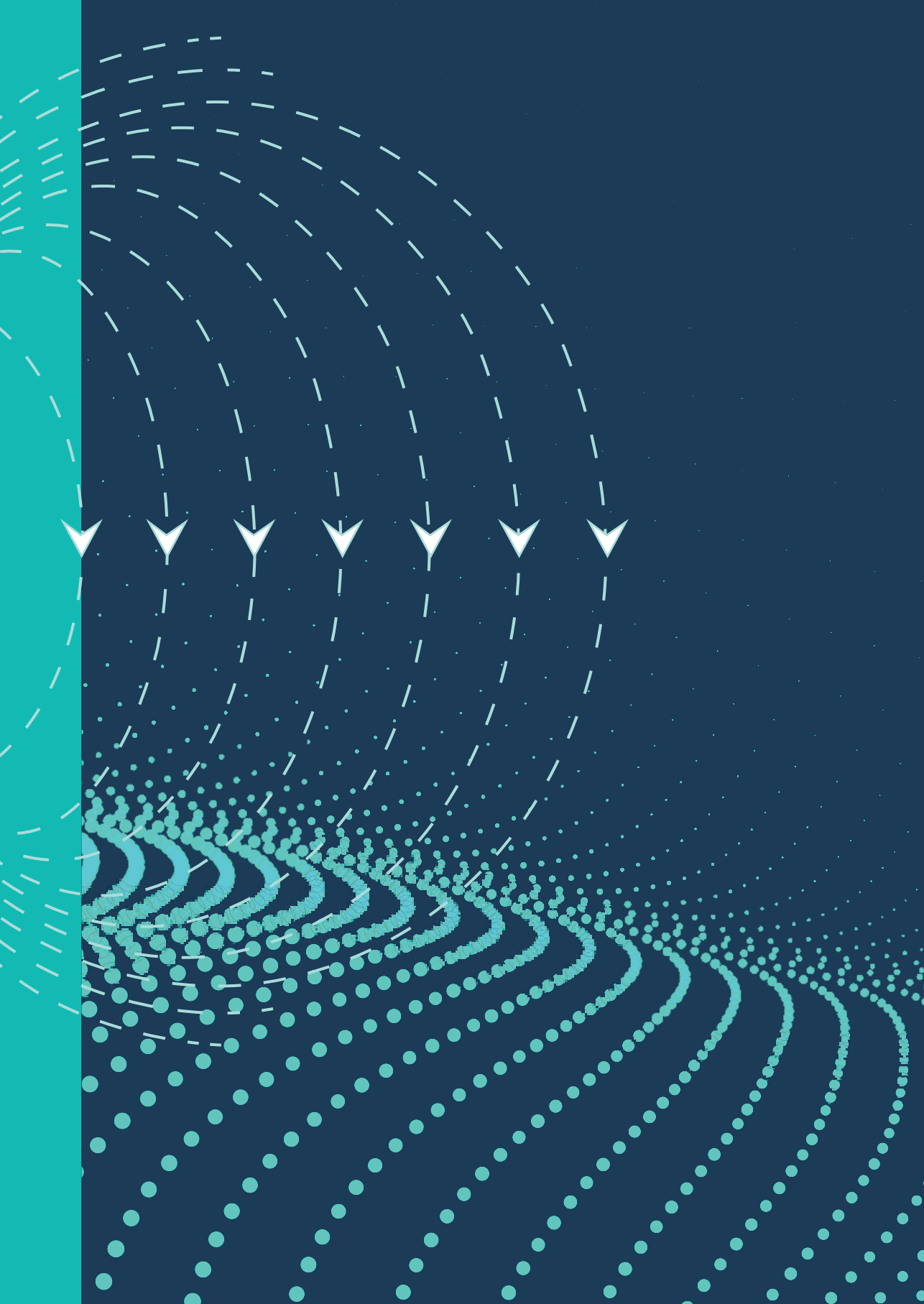
6

7

Full-Scale Experimental Study on Monitoring Fatigue Cracks in Steel Structures by Self Magnetic Flux Leakage Method

Abstract

A wireless monitoring system for detected cracks can significantly reduce operational costs and downtime for operators and owners of offshore and civil structures, and increase safety for surveyors by minimizing inspections. The Self Magnetic Flux Leakage (SMFL) method is the most promising for an affordable, robust, wireless monitoring system that is also easy to install. The SMFL depends on many factors that have been researched only for small-scale specimens with artificial cracks. The aim of this study is to experimentally investigate the applicability of the SMFL method for monitoring real through thickness fatigue cracks in full-scale steel structures, such as bridges, ships, and offshore structures. Measurements were performed on cracks in a suction hopper dredger and in a reconstructed steel bridge deck. The results give a clear indication of the location and size of each of the cracks by measuring the magnetic flux leakage with a Hall effect sensor in a grid with 5 mm spacing and with an altitude of 1 mm from the steel surface. The observed signal strengths are much larger than those of small-scale specimens, which means the magnetization in these large steel structures is significantly larger. Based on the results, it is hypothesized that the permanent magnetization is dominant over the Earth-induced magnetization, which would make the crack monitoring system less susceptible to changing background fields.

7.1. Introduction

The interaction of a fatigue crack in a ferromagnetic material with a weak magnetic background field is very complex as the Self Magnetic Flux Leakage (SMFL) is induced by several different sources: Earth-induced magnetization, stress-induced magnetization, and permanent magnetization. For that reason, together with the changing geometry of the crack under realistic loading conditions, the SMFL is dependent on many factors such as magnetic material properties, Earth field orientation, stress, crack opening, crack length, and on the history of all these factors due to steel's hysteresis property. These phenomena have all been investigated separately, numerically, and/or experimentally in the previous chapters of this work. However, experiments using SMFL measurements have so far only been performed on small-scale specimens and often on artificial cracks that were machined. Therefore, the aim of the research presented in this chapter is to experimentally investigate the applicability of the SMFL method for monitoring real through thickness fatigue cracks in full-scale steel structures, such as bridges, ships, and offshore structures.

The experimental study described in this chapter comprises of SMFL measurements on a number of fatigue cracks in a steel bridge deck and a suction hopper dredger. These structures and their fatigue cracks are described and illustrated in section 7.2, as well as the measurement setup and procedure. The results are presented in section 7.3 and discussed in section 7.4. Finally, some conclusions are drawn.

7.2. Method

The experimental setup and method of the study are described in this section. The first subsection describes a suction hopper dredger and two fatigue cracks in a torsion box at the deck of the ship. The second subsection describes a partial full-scale reconstruction of the deck of a real bridge and three cracks that initiated in the welded connections between a longitudinal box girder and a cross beam by cyclic loading of the deck in a laboratory. The magnetic measurement method and procedure for each of these cracks are described in the final subsection.

7.2.1. Suction Hopper Dredger

The suction hopper dredger that the measurements were performed on has torsion boxes as coamings on either side of the ship with transverse stiffener plates inside that were slot welded onto the outer plate of the box. Fatigue cracks have

appeared in these slot welds in at least two locations. The slots in the cover plates are 80 mm high and 25 mm wide and the thickness of these cover plates is 15 mm. The thickness of the stiffener plates is 20 mm. A schematic top view of the ship with coordinate system and the approximate locations of the two cracks are shown in Figure 7.1. The entire structure is made of FeE235 structural steel.
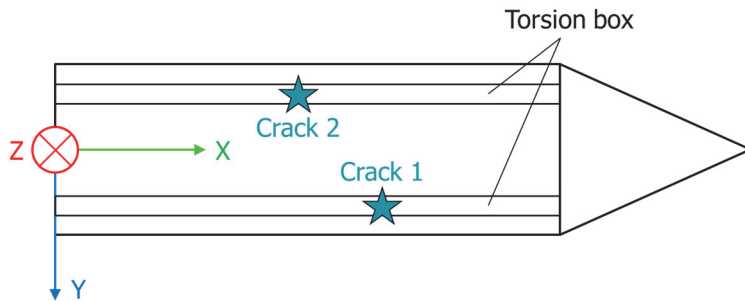
Figure 7.1: Schematic top view of suction hopper dredger with locations of cracks in torsion boxes.

A photo of the location of crack 1 on starboard side and a close up photo can be seen in Figure 7.2. This crack had already been repaired earlier and had reappeared. Significant corrosion can be observed due to local removal of the paint layer, which makes the crack very difficult to see with the naked eye. A photo of the location of crack 2 on portside and a close up photo can be seen in Figure 7.3. This crack was detected due to the small amount of corrosion but it cannot be visually observed as it sits underneath the paint layer. On the photo, a sticker with a measurement grid is already attached to the surface, which will be further explained in subsection 7.2.3.

Figure 7.2: Location (a) and close up photo (b) of crack 1 on starboard side.
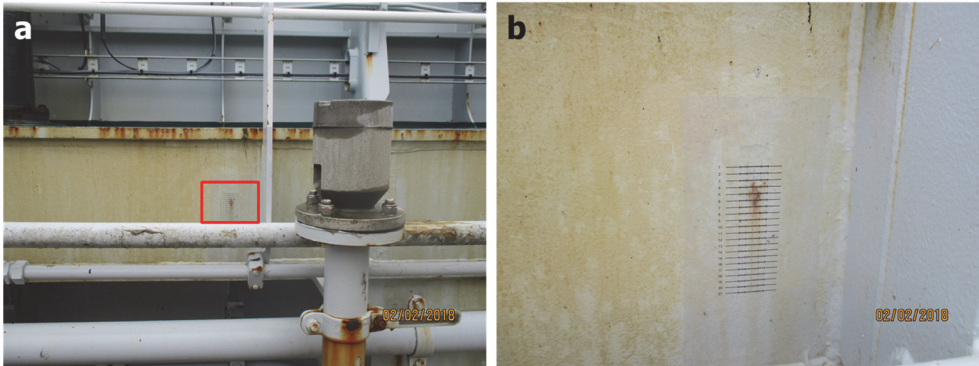
Figure 7.3: Location (a) and close up photo (b) of crack 2 on portside.

7.2.2. Bridge Deck

The FeE355 steel bridge deck that was measured on is a reconstruction of a real bridge in The Netherlands. The fatigue resistance of this partial full-scale reconstruction is investigated experimentally by the Steel and Composite Structures department of Delft University of Technology. This was a great opportunity to perform magnetic measurements on the cracks that have appeared in the structure due to fatigue loading. As can be seen in Figure 7.4, the structure consists of a deck plate with longitudinal box girders (troughs) and transverse cross beams. The plate thickness of the cross beams is 16 mm and the box girders are 6 mm thick. Fatigue cracks occurred at the welded connections between the box girders and the cross beams. All cracks initiated in the weld and propagated into the cross beam. Note that cracks 1 and 2 are in a different cross beam than crack 3. A close up photo of crack 1 is shown in Figure 7.5 and photos of cracks 1 and 2 with the measurement grid applied to the surface of the cross beam are shown in Figure 7.6 and Figure 7.7 respectively. The measurement grids are applied such that the crack tip of crack 1 is at row 14 and that of crack 2 is at row 6. Crack 3 has been measured at different stages of propagation.
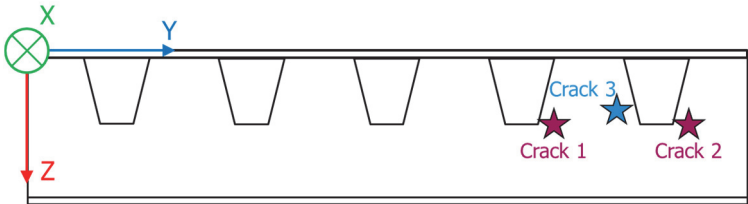
Figure 7.4: Schematic cross-section of bridge deck with locations of the fatigue cracks.

Figure 7.5: Close up photo of crack 1.
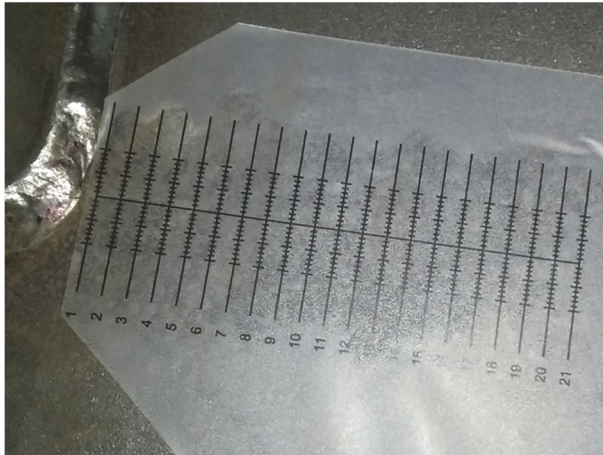
Figure 7.6: Crack 1 with measurement grid.
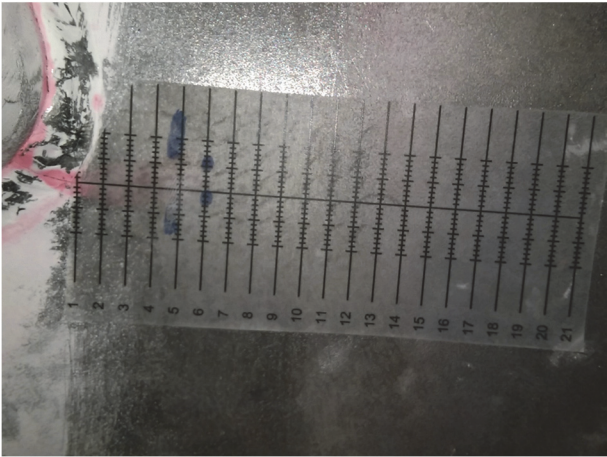
Figure 7.7: Crack 2 with measurement grid.

The third crack is in a different cross beam than cracks 1 and 2 and initiated as a weld root crack, propagated through the weld around the corner of the box girder, and then propagated into the cross beam. A close up picture of the location of crack 3 can be seen in Figure 7.8 and the markings on the cross beam show the propagation of the crack. At the time this picture was taken, the crack had propagated approximately 25 mm into the cross beam, which corresponds with the crack tip being at row 4 of the measurement grid. A transverse load was applied cyclically on the deck in between the box girders with a frequency of 3 Hz as can be seen in Figure 7.9.
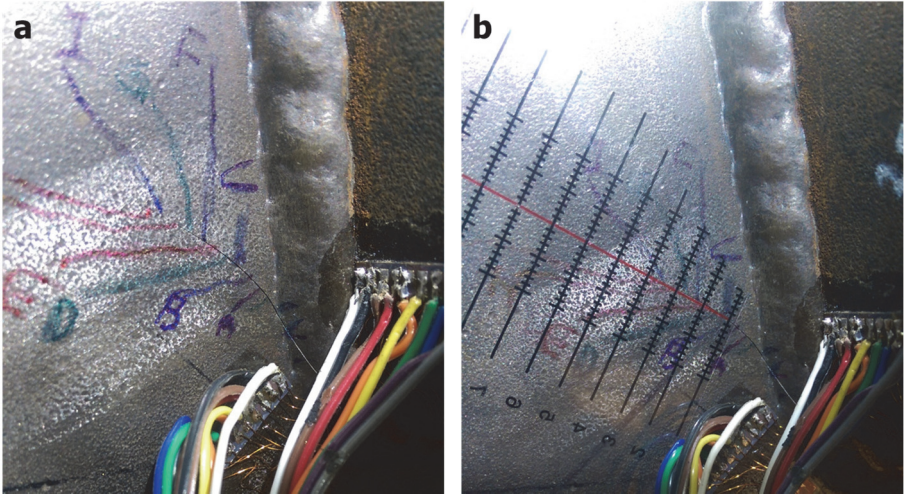
Figure 7.8: Close up photo of crack 3 (a) and with measurement grid (b).
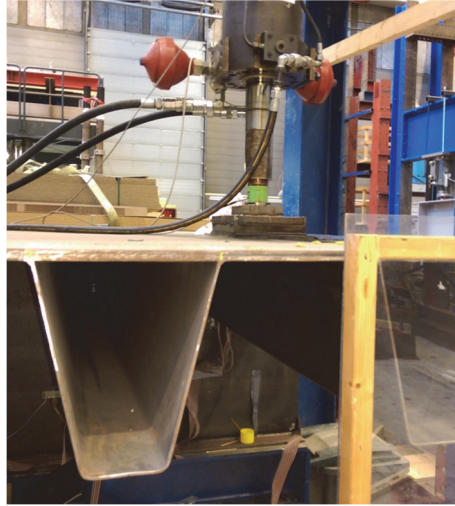
Figure 7.9: Loading mechanism for propagation of crack 3.

7.2.3. Measurement Procedure

For the SMFL measurements, a single axis magnetometer with a sensitivity of 1 µT is used [1]. A sticker with a measurement grid is placed on the surface such that the crack is approximately underneath the centerline of the grid, see Figure 7.6 and Figure 7.7. Each row on the measurement grid is numbered and has five measurement points (columns) with 5 mm spacing between them. The rows are spaced also 5 mm from each other. The sticker with the measurement grid can be seen in Figure 7.10. With the axial probe of the magnetometer, the out-of-plane component of the magnetic flux density is measured consecutively on each grid point at an altitude of 1 mm above the steel surface for the rows that are of interest for each particular crack. The positioning of the single axis magnetometer is depicted in Figure 7.11.
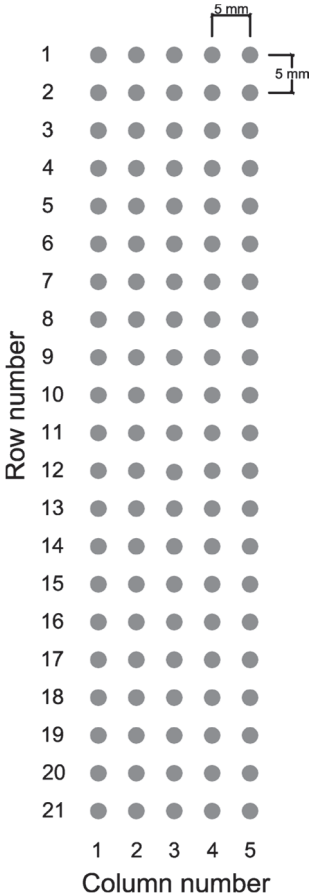
Figure 7.10: Measurement grid with 21x5 measurement points with spacing of 5 mm.

Figure 7.11: Measurement procedure with single axis magnetometer.

On the suction hopper dredger, all rows were measured for crack 1 and only the first seven rows were measured for crack 2 because of space restrictions due to a pipe as can be seen in Figure 7.3. On the bridge deck, all rows were measured for crack 1 except the first row because of space restrictions due to the weld. For crack 2 on the bridge deck, rows 3 to 13 were measured also because of space restrictions due to the weld and because this is a relatively short crack (tip is at row 6). For crack 3, measurements were taken on rows 3 to 18 at several stages during its propagation in the cross beam. In the first stage, the crack was approximately 25 mm long and for every other stage, the crack had propagated approximately 5 mm until the final length of 50 mm was reached.

Both on the suction hopper dredger and at the bridge deck, the background magnetic field was measured as well. To illustrate, the magnetic background field in X-direction on the suction hopper dredger was being measured in Figure 7.12.

Figure 7.12: Measurement of background field in X-direction on suction hopper dredger.

7.3. Results

The experimental results of the measurements that have been described in the previous section are presented here. The first subsection shows the measurement results for the cracks on the suction hopper dredger and the second subsection shows the results for the cracks in the bridge deck.

7.3.1. Suction Hopper Dredger

The results of the background field measurements on the ship are presented in Table 7.1. The three components of the measured background field correspond to the coordinate system shown in Figure 7.1.

Direction	B [µT]
X	-29
Y	71
Z	35

Table 7.1: Background field on suction hopper dredger.

The measured magnetic flux density in out-of-plane direction near crack 1 and with an altitude of 1 mm from the steel surface is shown in Figure 7.13 as a contour plot using linear interpolation. As can be seen, all 21 rows of the measurement grid have been measured. The colors represent the magnetic flux density in Y-direction (according to the coordinate system shown in Figure 7.1), which ranges between approximately -1 mT and +1 mT. A disturbance in the out-of-plane magnetic flux density is clearly visible around rows 4 to 14 with a negative peak along column 2 and a positive peak along column 3. Note that the actual crack length is difficult to observe due to excessive corrosion.

Figure 7.13: Measurement results for crack 1 on suction hopper dredger with altitude of 1 mm.

Figure 7.14 shows the measured magnetic flux density in out-of-plane direction near crack 2 with an altitude of 1 mm from the steel surface. This contour plot is also obtained by linear interpolation of the measured values on the measurement grid. Again, a disturbance can be seen in the form of a positive peak and negative peak, this time more concentrated around rows 3 to 5 and along columns 3 and 4. The range of the measured magnetic flux density in Y-direction is approximately between -200 µT and +50 µT. The picture of crack 2 in Figure 7.3 also suggests that crack 2 is rather small but it cannot be said with certainty as the paint has not been removed.
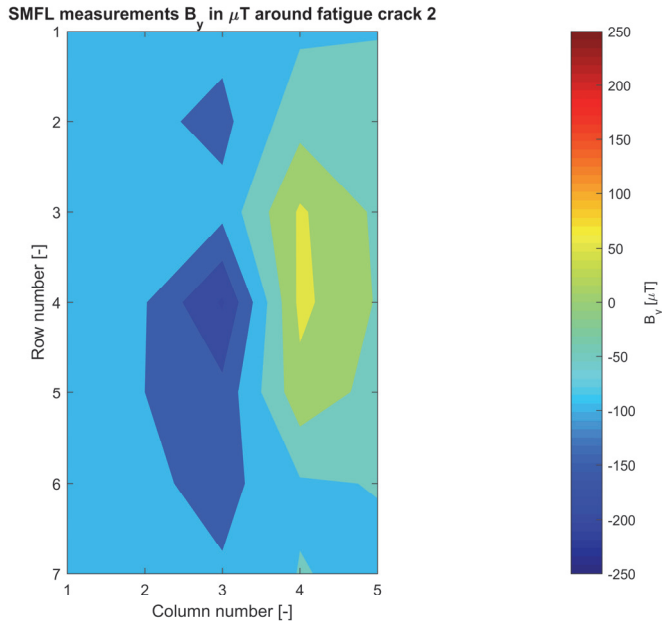
Figure 7.14: Measurement results for crack 2 on suction hopper dredger with altitude of 1 mm.

7.3.2. Bridge Deck

The results of the background field measurements near the bridge deck are presented in Table 7.2. The three components of the measured background field correspond to the coordinate system shown in Figure 7.4.

Direction	B [µT]
X	7
Y	-8
Z	31

Table 7.2: Background field near bridge deck.

In the exact same way as for the ship, the results of the measurements on the bridge deck are shown. Figure 7.15 shows the measured magnetic flux density in out-of-plane direction near crack 1 with an altitude of 1 mm from the steel surface as a contour plot. The colors represent the magnetic flux density in X-direction (according to the coordinate system shown in Figure 7.4), which ranges between approximately -100 µT and +500 µT. Note that the actual crack runs approximately in a straight line along column 3 and the crack tip is at row 14.
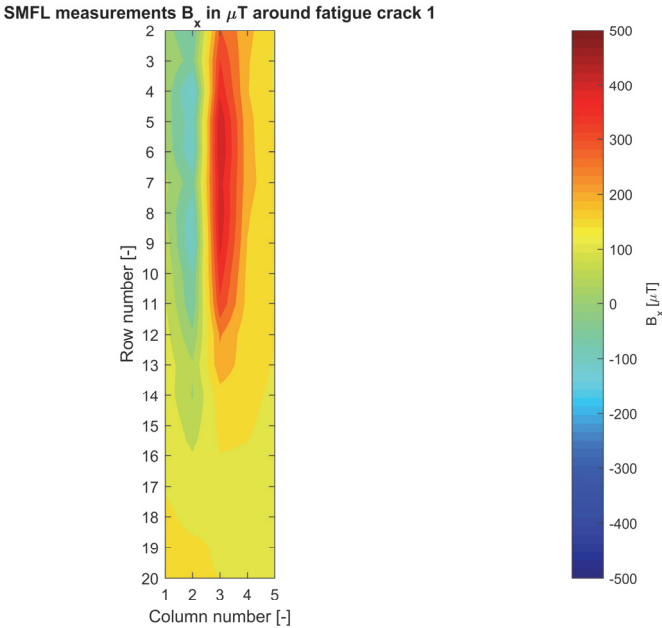
Figure 7.15: Measurement results for crack 1 in bridge deck with altitude of 1 mm.

Figure 7.16 shows the measured magnetic flux density in out-of-plane direction near crack 2 at an altitude of 1 mm. The crack is in between column numbers 2 and 3 and the crack tip is approximately at row number 6, which makes crack 2 much shorter than crack 1. Still, the measured signals are of the same order of magnitude as they range from approximately -400 µT to +400 µT.
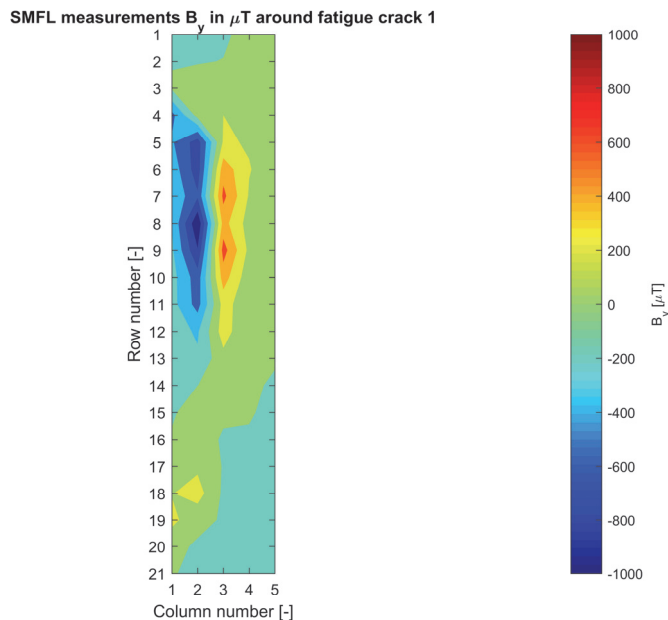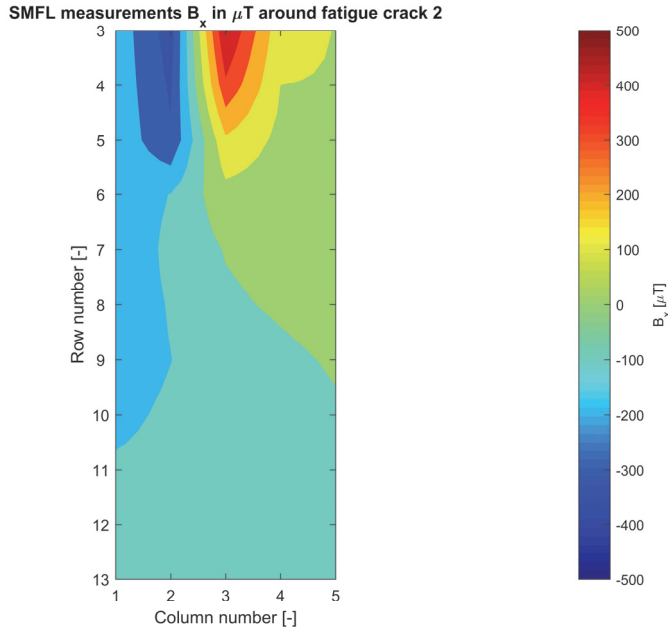
Figure 7.16: Measurement results for crack 2 in bridge deck with altitude of 1 mm.

Figure 7.17 shows the measured magnetic flux density in out-of-plane direction near crack 3 at an altitude of 1 mm and at different stages of crack propagation. Stage 1 corresponds to a crack length of 25 mm in the cross beam and the crack tip is approximately at row 4 of the measurement grid. At every next stage, the crack had propagated approximately 5 mm further in the cross beam up to 50 mm in the final stage where the crack tip was approximately located at row 9. The measured signals range from -200 µT to +400 µT.

Aside from the disturbance near the crack at the first few rows, there are significant disturbances in the measured signal in other areas as well. This is likely due to the fact that the crack length and depth profiles were measured at stages 1 and 2 using alternating current potential drop equipment, which involved placement of electrical probes using permanent magnets on the steel surface around the crack. The permanent magnets were not always placed at the exact same location so the disturbance they induced cannot be calibrated for. Still, signal processing techniques could be used to better identify the crack's location and to filter out disturbances unrelated to the crack. One simple technique is to differentiate the signal in the direction perpendicular to the crack in order to show the sharp peak behavior of the SMFL. Figure 7.18 shows the measurement results differentiated in the direction of the rows, so approximately perpendicular to the crack orientation. Note that these

results are obtained by first performing cubic interpolation of the measured signals from Figure 7.17. The location of the crack can be seen more clearly from the differentiated results where the maximum values are concentrated. The curvature of the crack, which is illustrated in the photo of Figure 7.19, can even be observed from these differentiated results. It can also be seen that the disturbances unrelated to the crack are getting filtered out during later stages of the crack propagation.
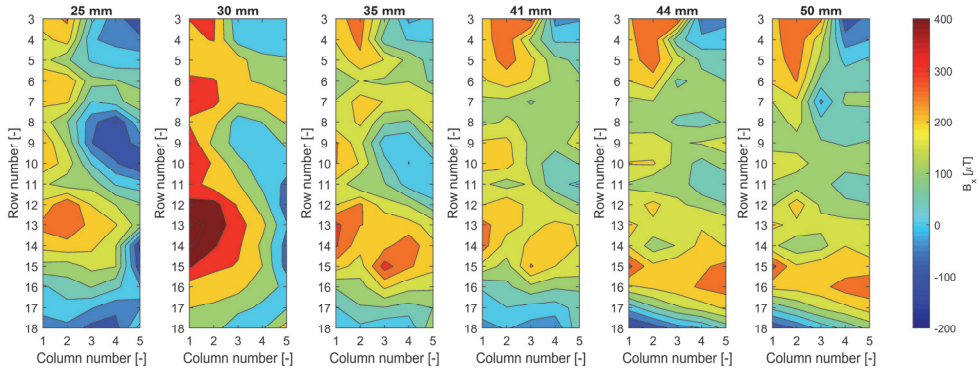
Figure 7.17: Measurement results for crack 3 in bridge deck with altitude of 1 mm – stages 1-6.
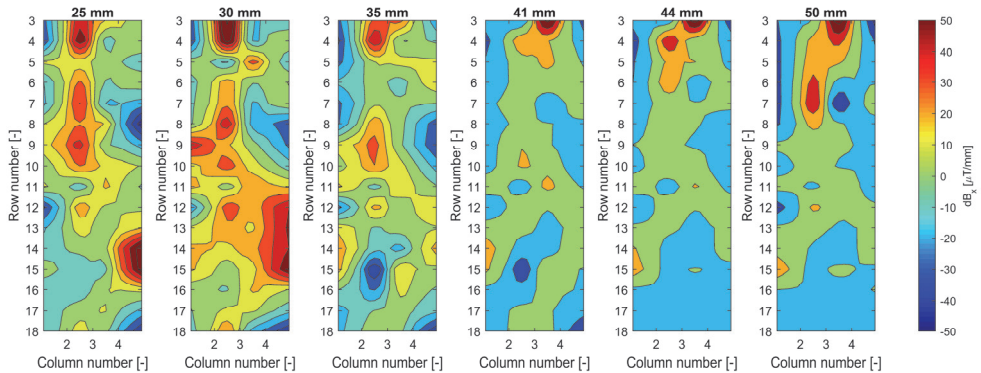
Figure 7.18: Differentiated results for crack 3 in bridge deck with altitude of 1 mm – stages 1-6.

Figure 7.19: Close up photo of crack 3 in stage 6.

7.4. Discussion

The results for the two cracks on the suction hopper dredger and crack 1 and 2 in the bridge deck are unambiguously in line with the theory on SMFL testing. A distinct positive and negative peak in the out-of-plane magnetic flux density are visible in the measurements, indicating the crack being in between the peaks where the sign change occurs. The observed signal strengths are much higher than earlier experimental results on small-scale specimens of a single plate, even though these plate specimens had machined cracks that are wider than actual fatigue cracks. It means that the level of magnetization in these full-scale steel structures is much higher than in a single steel plate. Also, aside from the disturbance near the crack, the measured signals for the cracks on the dredger and cracks 1 and 2 on the bridge deck have a smooth spatial distribution without any local peaks that need to be filtered out, which makes data processing rather straight forward. However, some data processing will still be needed to accurately characterize the crack length, which is extra challenging for real fatigue cracks in rather thick plates as they have not fully penetrated through the entire cross section around the crack tip, resulting in much smaller signal strengths near the crack tip.

Post-processing the measured data for crack 3 in the bridge deck is more challenging because multiple disturbances in the measurements are visible that are not caused by the crack, see Figure 7.17. As mentioned before, these disturbances are likely caused by the use of permanent magnets for measuring the crack length and depth profile using alternating current potential drop equipment. Although these

disturbances do not remain entirely constant, a general pattern of peak behavior can be observed. Hence, data filtering techniques may be able to significantly reduce these disturbances unrelated to the crack propagation, especially when monitoring a detected crack whose size and location is known prior to installing the crack monitoring sensor. It is shown that differentiation of the measured signals in the direction perpendicular to the crack already filters out the unrelated disturbances to some extent and that the location of the crack becomes more clear. Focusing solely on the top part of Figures 7.17 and 7.18, it is clear that the SMFL caused by the crack increases with increasing crack length, so the crack propagation can be followed. The curvature in the crack orientation is even visible, especially in the results for later stages. Still, it is challenging to accurately locate the position of the crack tip as the signal strength significantly decreases closer to the crack tip.

The measured magnetic flux densities are caused by a combination of Earth-induced magnetization and permanent magnetization, which cannot be separated for a full-scale structure as was done for a single plate in Chapter 4. However, the polarity of the SMFL gives an indication of the direction of magnetization inside the structure locally. Together with the background field measurements, an indication may possibly be obtained for the magnitude and orientation of the permanent magnetization. In the case of the dredger, the polarity of the SMFL indicates that the magnetization in the cover plates with the cracks is in astern direction, just as the background field. Therefore, the permanent magnetization will either be in astern direction as well, or its magnitude is significantly smaller than the Earth-induced magnetization. In the case of the bridge deck, the polarity of the SMFL indicates that the magnetization in the cross beams with the cracks is in upward direction as flux leaks out underneath the crack and enters back into the material above the crack. The background field, on the other hand, is in downward direction. Consequently, the permanent magnetization in the cross beams must be in upward direction in the vicinity of the crack and its magnitude must be significantly larger than that of the Earth-induced magnetization.

7.5. Conclusions

Self Magnetic Flux Leakage (SMFL) measurements have been conducted for real fatigue cracks in full-scale steel structures. The results from measurements on cracks in the coaming of a suction hopper dredger and on a bridge deck show that the SMFL method is suitable for monitoring cracks in large steel structures. Even for cracks in excessively corroded plates and for small cracks underneath a paint layer that are impossible to visually observe, the measurements using a single axis Hall effect sensor in a grid with 5 mm spacing give an unambiguous indication of their size

and location. The measured signal strengths are much larger when compared to the SMFL of small-scale specimens with machined cracks, which means that an inexpensive and small size Hall effect sensor is capable of measuring the SMFL for real through thickness fatigue cracks. The measurement grid with a spacing of 5 mm is sufficiently dense to be able to pick up the peak values of the SMFL at an altitude of 1 mm. Based on the findings in Chapter 5, one could even consider placing the sensors at a larger altitude to increase the signal width at the cost of reducing the signal strength. This way, the grid of sensors can be coarser, making the monitoring system cheaper, but the accuracy of crack characterization will then decrease as well.

It is demonstrated that a propagating crack under fatigue loading can be followed during different stages of propagation as the measured SMFL increases with increasing crack length. More research should still be done on signal processing of these measurements to filter out any disturbances unrelated to the propagating crack and to obtain accurate and reliable information on the crack length and the propagation rate. For instance, it is shown that differentiating the measured signals in the direction perpendicular to the crack already reduces these disturbances significantly. Also, a better indication should be pursued of how much the permanent magnetization contributes to the measured SMFL signals as compared to the Earth-induced magnetization. The hypothesis is that the permanent magnetization contributes significantly to the SMFL, making crack monitoring data more robust for changing orientation of the structure in the Earth's magnetic field. At the same time, the permanent magnetization can slowly vary as well due to magnetic hysteresis, relaxation, and stress-induced magnetization. The latter should be experimentally researched as well by conducting similar measurements as presented here but under cyclic loading.

7.6. References

[1]   Wuntronic. Wuntronic Tesla Meter KOSHAVA-USB n.d. http://www.wuntronic.de/en/USB-Tesla-Meter-Gauss-Meter-with-USB.html (accessed March 27, 2018).

7
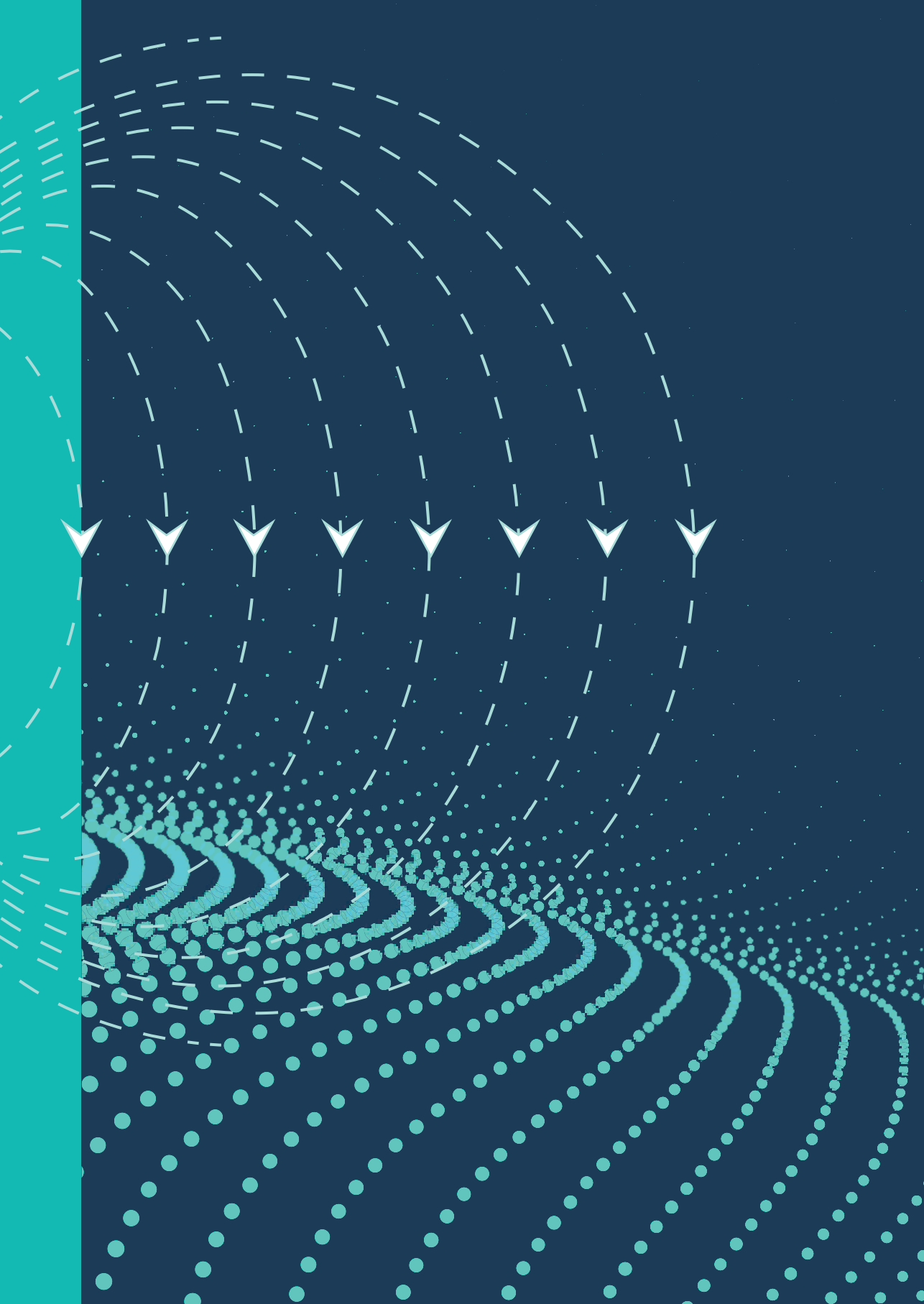
8

Review

8.1. Conclusions

A literature study on some widely used as well as state-of-the-art non-destructive evaluation methods was performed to select the most suitable method for monitoring detected and allowable cracks in ship and offshore structures. Magnetic measurement principles seem most promising because they can be intrinsically safe and no cleaning or polishing of the metal surface is required. In particular, the novel Metal Magnetic Memory method shows great potential to be used for a real-time crack monitoring system because no active magnetization is required. Instead, it measures the Self Magnetic Flux Leakage (SMFL) near a defect, which is induced by a passive magnetization due to the steel's hysteresis property and the Earth's magnetic field. Advantages of a passive crack monitoring system include increased battery life, wireless capability, robust design, and easy installation.

Although the SMFL technique is an attractive method for a real-time wireless monitoring system for detected cracks, many knowledge gaps exist that prevent a successful application to ship and offshore structures. Uncertainties related to e.g. magnetic material properties, welding, crack opening, plastic deformation, and magnetization due to applied stress need to be understood better in order to accurately characterize a crack by interpreting the SMFL measurements. The research described in this dissertation resulted in a better understanding of some of those uncertainties and their implications on fatigue crack monitoring by the SMFL method.

The magnetic measurements on a square steel plate with a slit from Chapter 3 confirmed the theoretical basis of the Metal Magnetic Memory method. The SMFL along the slit was large enough to be measured with a Hall effect sensor, which is currently inexpensive and small in size. By comparing the measurements with finite element results for the same plate in the same background field, it was found that the SMFL due to the permanent magnetization increases linearly with increasing distance from the crack tip and is an order of magnitude larger than the SMFL due to the Earth-induced magnetic field. It means that the sensitivity with respect to changes in the background field is small and that the method should even be successful when no background field is present. Accurate numerical simulation of the permanent magnetization, however, is challenging because it varies slowly in time due to hysteresis and is most likely non-uniform throughout a steel plated structure.

Unlike the permanent magnetization, the Earth-induced magnetization can accurately be calculated for any geometry by a finite element software package such as ANSYS Maxwell or COMSOL Multiphysics. To this end, the magnetic permeability of structural steel is required. For weak magnetic fields, such as the Earth's magnetic field, hysteresis may be neglected and the material may be assumed magnetically

linear, so with a constant permeability. In Chapter 4, the induced magnetic field for the square steel plate with a slit was measured by separating it from the permanent magnetic field by using a magnetic field simulator. When comparing the measured values with results from finite element analysis using a constant and uniform relative permeability of 225 for the steel plate, errors were found to be less than 5%. This result confirms that the Earth-induced magnetization of a structural steel plate can be accurately calculated by finite element simulation with constant and uniform magnetic material properties, even though analysis of an ellipsoid sample from the same steel plate resulted in a different relative permeability of 115. It means that either the magnetic material properties can differ locally but globally they can be assumed homogeneous, or the steel's properties were changed due to the manufacturing process of the ellipsoid sample.

A numerical parametric study on a through thickness center cracked steel plate and on a steel T-joint with a double-sided and unpenetrated fillet weld with a through thickness crack along one weld toe was described in Chapter 5. Four parameters (altitude, Earth field orientation, crack opening, and crack length) and their effects on the Earth-induced SMFL were investigated by finite element analysis using the magnetic material properties found in Chapter 4. Firstly, it was found that for increasing altitude, the SMFL signal strength decreases as a power function and the signal width increases linearly. Secondly, the signal strength was found to be proportional to the effective background field, which is in-plane and perpendicular to the crack orientation. Thirdly, the SMFL of the center cracked plate decreased significantly for crack openings less than 0.5 mm. Finally, a gradual increase in SMFL signal strength was observed in the middle of the crack when the crack length increases. Furthermore, it was demonstrated that for the T-joint geometry in combination with realistic parameter values (crack length of 50 mm, crack width of 0.3 mm, Earth field orientation of 60 degrees with respect to the crack, altitude of 1 mm), the Earth-induced SMFL is still strong enough to be measured with a Hall effect sensor. An additional requirement for such a geometry is that sensors need to be placed on the weld as well.

In Chapter 6, the effect of the stress-induced magnetization on the SMFL near a stress concentration was investigated experimentally and numerically. For a structural steel plate of 5 mm thick and 70 mm wide in the Earth's magnetic field, the maximum change in measured SMFL due to applied tension up to the design yield stress was approximately 25 μT near an elliptical hole of 10 by 3 mm. The measured stress-induced magnetic flux density during cyclic loading showed cyclic behavior with the loading frequency and formed a closed loop, so the irreversible magnetization was negligible. Interesting was that the spatial distribution of the measured stress-induced magnetic flux density was not symmetric around the

elliptical hole and even appeared irregular. This is most likely attributed to the non-uniform magnetization in the steel plate upon which the stress-induced magnetization is dependent. Neglecting any irregularities, a qualitative comparison between measurements and results from a numerical simulation based on a theoretical framework of the magnetomechanical effect showed that the two were in good agreement.

Finally, a full-scale experimental investigation on the applicability of the SMFL method for real through thickness fatigue cracks was presented in Chapter 7. Results from magnetic measurements on cracks in a suction hopper dredger and a reconstructed steel bridge deck show a clear indication of the location and size of the cracks, even when the surface was highly corroded or when the crack was not visible as it was underneath a paint layer. One of the cracks in the bridge deck was measured at different stages of propagation under fatigue loading and it was demonstrated that the propagating crack could be followed. The observed signal strengths were much larger than those of earlier experiments on small-scale specimens, so the magnetization in these large steel structures must be significantly larger than for a single steel plate. The measurements were taken in a grid with a spacing of 5 mm and at an altitude of 1 mm. As the measured signal strengths are much above the sensitivity of an inexpensive and small-sized Hall effect sensor, a larger altitude could be chosen to increase the signal width so that the sensor spacing can be larger, making the monitoring system even more affordable.

8.2. Implications

This research has shown that the Self Magnetic Flux Leakage (SMFL) method is a very promising technique for monitoring detected and allowable fatigue cracks as it is fully passive, which creates opportunities for a crack monitoring system that is robust, wireless, affordable, and easy to install. The experimental and numerical results described in this thesis have increased our knowledge on several uncertainties that have prevented the application of the SMFL method to ship and offshore structures to date. This knowledge can be used as input for the development of a crack monitoring system for ship and offshore structures based on the SMFL method.

The envisaged crack monitoring system would consist of arrays of Hall effect sensors that are placed on detected cracks, so that their propagation can be monitored without additional inspections. The Hall effect sensors need to be placed at an optimal altitude above the metal surface, balancing between the sensor sensitivity and accompanied costs, and the spatial density of sensors required for accurate crack

length characterization. In principle, a crack can be monitored as long as it is underneath the sensor array. However, crack length dependency of the SMFL creates opportunities to estimate the crack length even when it has propagated outside the sensor array. The sensor sampling rate is dictated by the frequency in which the crack opens and closes, which is approximately the wave frequency for ship and offshore structures. By performing several measurements during one wave period, the SMFL for maximum crack opening displacement can be extracted. If a crack does not open and close as a result of the wave loading, it means that the crack will not grow and monitoring would be redundant.

Measured SMFL signals are relatively weak when compared to Magnetic Flux Leakage signals with active magnetization typically close to magnetic saturation. For this reason, additional effects may need to be taken into account and corrected for by the envisaged crack monitoring system. One of those effects is that the orientation of ships or weathervaning floating structures can change continuously. From numerical results in Chapter 5, it was concluded that the Earth-induced SMFL is directly proportional to the effective background field that is in-plane and perpendicular to the crack. Hence, a correction on the measured SMFL may be needed related to the structure's orientation in the Earth's magnetic field. On the other hand, from experimental results in Chapter 3 and Chapter 4 it was concluded that the permanent magnetization can be one order of magnitude larger than the induced magnetization. Another effect that may need to be corrected for is the stress-induced magnetization, which was investigated in Chapter 6. As stresses are very large around the crack tip and nearly zero along the wake of the crack, the stress-induced magnetization may change the way measured SMFL signals should be interpreted. However, the experimentally found maximum change in the SMFL of 25 µT due to tensile stress is probably negligible when monitoring a through thickness crack with a length of at least 50 mm in a thick steel plate that is part of a large structure as signal strengths close to 1 mT were reported in such cases in Chapter 7.

The envisaged crack monitoring system should become a decision support tool for asset owners and operators of ship and offshore structures for a more rational maintenance and repair strategy based on real-time information whether a detected crack is growing or not, and if so, what the propagation rate is. Such a crack monitoring system could also be linked with existing structural health monitoring systems, such as Monitas and Risk Based Inspection (RBI). The Monitas system monitors the actual fatigue lifetime, which is calculated by a fatigue design tool that uses measured data instead of design assumptions. Information on the length and propagation rate of detected cracks can be a valuable input for validation of the calculated fatigue lifetime by the Monitas system. Within RBI, inspection intervals are adjusted according to inspection results by continuously updating the probability of

8

fatigue failure of detected and unrepaired cracks. A real-time crack monitoring system would provide significantly more input data on detected cracks when compared to periodical inspection by surveyors, which can make RBI a much more effective method than it already is. Ultimately, linking these systems with a crack monitoring system as investigated in this thesis would result in optimized operational cost, less downtime, and safer operation.

8.3. Recommendations for Future Work

Although the research described in this thesis forms a good basis, there is more work to be done before a crack monitoring system based on the SMFL method can be developed and applied to ship and offshore structures. As a first step, some prototypes would need to be developed to gather more full-scale experimental data on the performance of such a crack monitoring system in realistic conditions. When more data is available, the attention should focus on signal processing techniques to accurately and reliably characterize a crack's geometry from SMFL measurements.

Some more fundamental research topics need further attention as well. First of all, magnetic material properties of structural steels will need to be further investigated, also for high strength steels, so that the Earth-induced magnetization and also the permanent magnetization of steel structures can be more accurately simulated by finite element method. Secondly, the material properties of weld material and heat affected zones need to be researched as most fatigue cracks are found near welds, and this will have a significant effect on the measured SMFL signals. Not only is the weld material different than the base material but there are also residual stresses in welds that will have an effect on the SMFL. Thirdly, the interaction between high local stresses at a crack tip and the magnetization of ferromagnetic steel in a weak background field needs to be researched further because the stress-induced magnetization may be more significant for real fatigue cracks instead of an elliptical hole as stress concentration zone.

Once some of the aforementioned fundamental questions are answered, the application of the SMFL method should be expanded from only through thickness cracks in the base material to more complex crack configuration, such as weld toe cracks, weld root cracks, semi-elliptical surface cracks, subsurface flaws, and combinations of those. It may even be possible to measure corrosion with the SMFL method. When all these additional applications are possible, endless new possibilities will arise that many different industries can potentially benefit from.

8

Acknowledgements

My research has been a process that involved many people without whom I would not have been able to present this final product, my doctoral dissertation. Some people have contributed directly to my research and others indirectly by supporting me in any form or way. I would like to thank every single one of them and a select few people I would like to acknowledge explicitly in the next few paragraphs.

First of all, I would like to thank my promotor Mirek Kaminski for giving me the opportunity and motivation to pursue my doctorate, for his endless enthusiasm throughout the entire journey, and for being my greatest supporter until the very end. Under Mirek's leadership, the section Ship and Offshore Structures has grown over the past few years to a diverse team of great colleagues. I would like to thank everyone in the Ship and Offshore Structures family, but also the people in the Ship Hydromechanics section, for their efforts in creating such a wonderful atmosphere at work that is both academically stimulating and fun at the same time.

Secondly, I would like to thank the companies that have participated in the CrackGuard Joint Industry Project and the people representing them during our many progress meetings for not only funding my research but also giving it a purpose. I would especially like to thank Erik Puik, managing director of DotDotFactory BV, for all his hard work in this project and always managing to translate the knowledge that I gathered into an improved sensor prototype. I enjoyed working with Erik, who was basically a co-promotor for me as he was always my second greatest supporter after Mirek. As I said, the CrackGuard Joint Industry Project has given my research purpose and the fact that I got to manage this project and have regular progress meetings with companies trying to solve an actual problem has been an enrichment of my PhD research and personal development.

Thirdly, there are some people who directly contributed to this dissertation who I would like to acknowledge. I want to thank my colleague PhD candidate Aad Vijn from the faculty of Electrical Engineering, Mathematics and Computer Science and TNO, The Hague for allowing me to use their measurement facilities and assisting me with conducting the experiments in Chapter 4. Aad also provided me with a solver that was used to calculate the numerical results of the magnetomechanical model in Chapter 6. I also want to thank former MSc students Offshore and Dredging

Engineering at Delft University of Technology Sylvia van Kreveld and Marijn Abrahamse for their contribution to my research in their Master Theses. They both worked full-time on a subject related to my research for nine months and without their help I could not have performed and analyzed as many experiments as I did in this time frame.

Then, I would like to give a special thanks to my parents for giving me all the opportunities in the world and the freedom to chase any dream I had. My parents, my grandparents, and my brother Tim provided me with the best childhood I can imagine, which prepared me for an even better time in my life as a student in which I opened up as a person and found out who I really was and what my talents are. I should also thank my parents for having me in the United States of America, because my dual citizenship led me back to the country I was born in, which brought me great career opportunities and led me into the arms of my soul mate.

That brings me to the last person I want to acknowledge and who I am most grateful for: my beloved wife, Mallery. I feel like everything in my life has happened for a reason so that I would be in the right place at the right time to meet this beautiful woman, inside and out. I will be forever grateful for the commitment she has shown me by leaving her home country and all her family and friends behind immediately after graduating, just to be with me and to support me while I pursued my PhD. That makes this PhD just as much hers as it is mine. Thank you from the bottom of my heart for all your love and support. I love you, Mallery!

Menno van der Horst
Delft, July 2018

List of Publications

Conference Proceedings

M.P. van der Horst, M.L. Kaminski and E. Puik, Methods for Sensing and Monitoring Fatigue Cracks and Their Applicability for Marine Structures, Proceedings of the International Offshore and Polar Engineering Conference, Anchorage, Alaska, 2013, p. 455-462.

M.P. van der Horst, M.L. Kaminski and E. Lepelaars, Testing and Numerical Simulation of Magnetic Fields Affected by Presence of Fatigue Cracks, Proceedings of the International Offshore and Polar Engineering Conference, Busan, South-Korea, 2014, p. 445-450.

M.P. van der Horst and M.L. Kaminski, Slit Induced Self Magnetic Flux Leakage in a Square Steel Plate, Proceedings of the International Offshore and Polar Engineering Conference, Sapporo, Japan, 2018, p. 7-13.

Journal Papers

M.P. van der Horst and M.L. Kaminski, Magnetic Properties of Structural Steels for Simulation of Crack Monitoring by Finite Element Method, Manuscript under Review.

M.P. van der Horst and M.L. Kaminski, Simulation and Analysis of Earth-Induced Magnetic Flux Leakage for Monitoring Cracks in Ship and Offshore Structures, Manuscript under Review.

M.P. van der Horst, S.L. van Kreveld and M.L. Kaminski, Effect of Stress-Induced Magnetization on Crack Monitoring by Self Magnetic Flux Leakage Method, Manuscript under Review.

M.P. van der Horst, M. Abrahamse and M.L. Kaminski, Full-Scale Experimental Study on Monitoring Fatigue Cracks in Steel Structures by Self Magnetic Flux Leakage Method, Manuscript under Review.

About the Author

Menno van der Horst was born on May 19th, 1990 in Santa Clara, California in the United States of America. He was only one and a half years old when his parents moved back to the Netherlands, where he grew up. He obtained his VWO high school diploma in 2008 from Het Baarnsch Lyceum in Baarn with electives in Nature, Health, and Technology. After that, he started his Bachelor of Science in Civil Engineering at Delft University of Technology, which he graduated from in 2011 with honors. The title of his BSc Thesis was "Fracture Propagation in Lattice Models". Immediately after that, he started his Master of Science in Structural Engineering specializing in Structural Mechanics, also at Delft University of Technology. Some of his courses he took at the National University of Singapore, where did an exchange program for one semester. He also did an internship in the United States at the American Bureau of Shipping in Houston, Texas, where he developed a tool for fracture and leakage analysis in LNG tankers. During these exciting three months, he also met his wife who moved to The Netherlands a year later. In May 2014, he graduated Cum Laude and with honors. The title of his MSc Thesis was "Passive Monitoring of Fatigue Cracks in Steel Ship and Offshore Structures", which led straight into his PhD as his work on this topic was not finished yet. His PhD was fully funded by industry as his work was part of the CrackGuard Joint Industry Project (JIP), which he managed as well during the complete four years of his PhD. In the summer of 2017, he spent three months in Houston, Texas again. This time, he worked as a Facilities Engineering Intern at Chevron Energy Technology Company (ETC) where he conducted a technology assessment of a novel in-line mooring tensioner system for floating production units. After finishing his PhD, he will return to Chevron ETC as a full-time Facilities Engineer in the Subsea, Civil & Marine Engineering department.